UNIVERSIDADE FEDERAL DO RIO DE JANEIRO

INSTITUTO DE FÍSICA

Thermodynamic, magnetic and transport properties of strongly correlated systems

Andressa Raquel Medeiros Teixeira da Silva

Tese de Doutorado apresentada ao Programa de Pós-Graduação em Física do Instituto de Física da Universidade Federal do Rio de Janeiro - UFRJ, como parte dos requisitos necessários à obtenção do título de Doutora em Ciências (Física).

Orientadora: Thereza Cristina de Lacerda Paiva

Rio de Janeiro

Maio de 2025

Thermodynamic, magnetic and transport properties of strongly correlated systems

Andressa Raquel Medeiros Teixeira da Silva

Thereza Cristina de Lacerda Paiva

Tese de Doutorado apresentada ao Programa de Pós-Graduação em Física do Instituto de Física da Universidade Federal do Rio de Janeiro - UFRJ, como parte dos requisitos necessários à obtenção do título de Doutora em Ciências (Física).

Aprovada por:

Profa. Dra. Thereza Cristina de Lacerda Paiva - IF/UFRJ
(Presidente e orientadora)

Prof. Dr. Marcello Barbosa da Silva Neto - IF/UFRJ

Profa. Dra. Maria Carolina de Oliveira Aguiar - UFMG

Prof. Dr. Eric de Castro e Andrade - USP

Profa. Dra. Helena de Souza Bragança Rocha - UnB

Rio de Janeiro

Maio de 2025

M488 Silva, Andressa Raquel Medeiros Teixeira da
Thermodynamic, magnetic and transport properties of strongly correlated systems / Andressa Raquel Medeiros Teixeira da Silva - - Rio de Janeiro, 2025.
118f.
Orientadora: Thereza Cristina de Lacerda Paiva
Tese (doutorado) - Universidade Federal do Rio de Janeiro, Instituto de Física, Programa de Pós-graduação em Física, 2025.
1. Strongly correlated systems. 2. Magnetism. 3. Monte Carlo method. 4. Hubbard model. I. de Lacerda Paiva, Thereza Cristina, orient. II. Thermodynamic, magnetic and transport properties of strongly correlated systems.

Resumo

Thermodynamic, magnetic and transport properties of strongly correlated systems

Andressa Raquel Medeiros Teixeira da Silva

Orientadora: Thereza Cristina de Lacerda Paiva

Resumo da Tese de Doutorado apresentada ao Programa de Pós-Graduação em Física do Instituto de Física da Universidade Federal do Rio de Janeiro - UFRJ, como parte dos requisitos necessários à obtenção do título de Doutora em Ciências (Física).

Recentemente, tem havido interesse em estudar as diversas propriedades de sistemas fortemente correlacionados. A presença de frustração, por exemplo, pode afetar o magnetismo do sistema devido à alta degenerescência do estado fundamental. Sistemas com geometrias específicas podem ser desenvolvidas por meio de engenharia de vacâncias, obtendo sistemas com resposta magnética mais intensa para um determinado regime de interações. Também é possível estudar o efeito de perturbações dependentes do tempo para obtenção de diferentes propriedades. É interessante notar que as propriedades quânticas de sistemas interagentes podem ser percebidas a temperaturas finitas, permitindo analisar efeitos de emaranhamento nessa situação.

Neste trabalho estudamos a hamiltoniana de Hubbard por meio de simulações numéricas, em especial por Monte Carlo quântico determinantal, com objetivo de entender os efeitos da interação eletrônica sobre correlações magnéticas e propriedades de transporte.

Primeiramente, analisamos a rede kagome, conhecida por possuir frustração. Observamos a transição entre um metal paramagnético e um isolante de Mott em $U/t = 6.5 \pm 0.5$,

e descobrimos ser possível resfriar adiabaticamente nosso sistema para entropias menores que $s \approx \ln 2$.

Também estudamos o emaranhamento de um sítio com o restante da rede em temperaturas finitas como uma forma de sinalizar transições de Mott. Para isso, estudamos a hamiltoniana de Hubbard em três geometrias bidimensionais diferentes cujas transições de Mott são conhecidas e analisamos a relação entre o emaranhamento de um sítio e a interação de Hubbard e a densidade eletrônica. Encontramos que o emaranhamento e suas derivadas quanto a U e quanto a n nos permitem estimar de forma razoável a transição de Mott.

Um outro tema abordado foi o estudo de um semimetal de linhas nodais, criado por meio de engenharia de vacânicas a partir de uma rede *honeycomb*. Identificamos que o sistema se torna um isolante magnético para qualquer $U/t > 0$, e possui magnetismo não homogêneo dentro da célula unitária, diferente da rede pristina.

Finalmente, investigamos como utilizar fotoirradiação para obter supercondutividade em uma rede bicamada. Observamos que é possível introduzir um potencial vetor nas hamiltonianas de Hubbard e tJ que pode ser ajustado de modo a sair do estado fundamental e atingir um estado com maior resposta supercondutora.

Palavras-chave: Sistemas fortemente correlacionados, Magnetismo, Método de Monte Carlo, Modelo de Hubbard.

Abstract

Thermodynamic, magnetic and transport properties of strongly correlated systems

Andressa Raquel Medeiros Teixeira da Silva

Orientadora: Thereza Cristina de Lacerda Paiva

Abstract da Tese de Doutorado apresentada ao Programa de Pós-Graduação em Física do Instituto de Física da Universidade Federal do Rio de Janeiro - UFRJ, como parte dos requisitos necessários à obtenção do título de Doutora em Ciências (Física).

Recently, there has been increasing interested in studying several properties of strongly correlated systems. The presence of frustration, for instance, can affect the magnetism of the system due to the high degeneracy of the ground state. Systems with specific geometries can be designed through vacancy engineering, obtaining systems with a more intense magnetic response for a given regime of interactions. It is also possible to study the effect of time-dependent perturbations to obtain different properties. It is relevant to note that the quantum properties of interacting systems can be perceived at finite temperatures, allowing the analysis of entanglement effects in this situation.

In this thesis we study the Hubbard Hamiltonian through numerical simulations, specifically through determinant quantum Monte Carlo, with the aim of understanding the effects of electronic interaction on magnetic correlations and transport properties.

We firstly analyze the kagome lattice, which is known to have frustration. We find a transition between a paramagnetic metal and a Mott insulator at $U/t = 6.5 \pm 0.5$, and find that it is possible to adiabatically cool our system to entropies smaller than $s \approx \ln 2$.

We then investigate the entanglement between a site with the rest of the lattice at finite temperatures as a means to signal Mott transitions. To do this, we study the Hubbard Hamiltonian in three different two-dimensional geometries whose Mott transitions are known and analyze the relation between the single-site entanglement with the Hubbard interaction and with the electronic density. We find that the entanglement and its derivatives with respect to U and with respect to n allow us to reasonably estimate the Mott transition.

Another topic addressed was the study of a nodal line semimetal, created through vacancy engineering from a *honeycomb* network. We identified that this system becomes a magnetic insulator for any $U/t > 0$, and has inhomogeneous magnetism within the unit cell, different from the pristine network.

Finally, we investigated how to use photoirradiation to enhance superconductivity in a bilayer. We observed that it is possible to introduce a vector potential in the bilayer Hubbard and t-J models that can be fine-tuned to leave the ground state and access a state with a higher superconducting response.

Keywords: Strongly correlated systems, Magnetism, Monte Carlo method, Hubbard model.

Agradecimentos

Agradeço a minha família pelo suporte que me deram ao longo da vida. Em especial, agradeço à minha avó Disterro, por todo o carinho e por ser um exemplo de persistência.

Gostaria de agradecer à professora Thereza Paiva pela confiança e por todo o suporte que me ofereceu. Agradeço ao professor Rubem Mondaini por me receber e supervisionar durante minha estadia na Universidade de Houston. Também gostaria de expressar gratidão ao professor Natanael Costa pelas contribuições para a minha formação. Também agradeço aos meus colegas na UFRJ, especialmente Sebastião e Rodrigo, pelas discussões sobre física e pela amizade que me ofereceram.

Finalmente, agradeço às instituições CAPES, CNPq e FAPERJ pelo apoio financeiro.

Contents

List of Figures

Chapter 1

Introduction

Magnetic frustration is a central issue in Condensed Matter Physics, with a great experimental effort being devoted, over the past decades, to understand its effects. Its origin can be attributed to geometry and the kind of interactions considered, that prevent a single minimum energy state to be obtained. For instance, antiferromagnetically coupled Ising spins in a triangular geometry exhibit frustration, since it is not possible to find a single arrangement of spins that minimizes all interactions. This causes degeneracy in the ground state of these systems, which can lead to a myriad of correlated phases at low temperatures. Among the many geometries leading to frustration, the kagome lattice has gained much attention recently due to the possibility of the occurrence of a quantum spin liquid (QSL) state. The experimental realization of this geometry is found, e.g., in herbertsmithite compounds [10, 11] like the one in Fig. 1.1, exhibiting strong evidences for the occurrence of QSL, although its nature is still under debate [12, 13, 1].

The electronic properties of the kagome lattice have also been investigated by the manipulation of atoms and molecules on given substrates [14, 15], although the tuning of the interaction strength remains a challenge. The advent of optical lattices has raised great expectations for unveiling fundamental properties of strongly correlated systems, in particular those with frustration. Within this context, optical lattices for the kagome geometry were recently realized for bosonic atoms [16, 17, 18], and one expects that fermionic ones could be realized in the near future. In spite of the experimental effort, manipulating

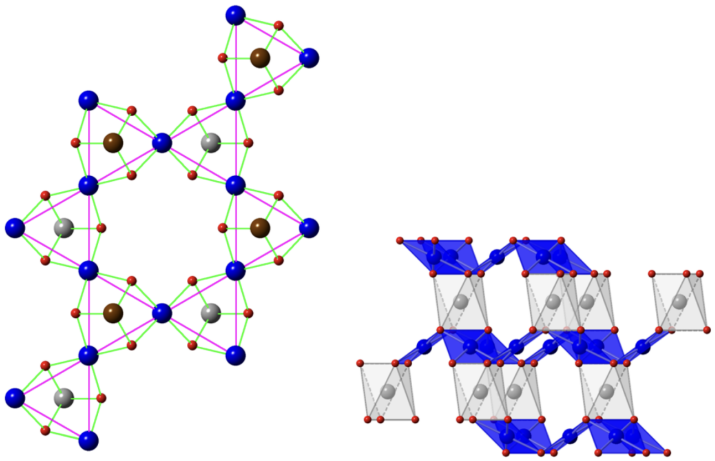

Figure 1.1: Crystal structure of herbertsmithite $ZnCu_3(OH)_6Cl_2$. In the left the view when looking down along the c axis. On the right is a side view of the crystal structure. From [1].

these many-body states is an arduous task, therefore providing information that could guide experiments is clearly in order.

It is also interesting to note that by setting one of the diagonal hoppings of the kagome lattice as $t' = 0$, one ends up with the so-called Lieb lattice (or decorated square lattice or CuO_2 lattice). Like the kagome lattice, the Lieb lattice also displays a flat tight-binding band, located at the particle-hole symmetry point. With on-site repulsion, the Lieb lattice at half filling is not frustrated, but is a ferrimagnetic insulator for all $U > 0$. A question that then arises is how the ferrimagnetic insulator at $t' = 0$ evolves to either a Mott insulator or a paramagnetic metal as $t' \to t$.

On the subject of detecting and characterizing quantum phases of matter, it has been established that entanglement can be especially useful in correlated many-body and cold-atoms systems, entanglement [19, 20, 21, 22, 23, 24, 25, 26]. For the particular case of the one-dimensional (1D) Hubbard model, bipartite entanglement has been used to explore quantum phase transitions at $T = 0$, such as metal-insulator transitions [27, 28, 29, 30, 31, 32] and superfluid-insulator transitions [33], including in disordered systems [34, 35] and conventional superfluid to exotic superfluid transitions in spin-imbalanced systems [36, 37]. The restriction to zero temperature arises from the von Neumann entropy, which is

a proper measure of bipartite entanglement only for pure states.

In contrast, in two-dimensional fermionic systems, entanglement has been less explored since numerical techniques often employed on 1D systems start facing limitations. Going beyond the computation of free-fermionic systems in either Hermitian [38] or non-Hermitian settings [39], the work by Grover [40] pioneered a method to study the Rényi entanglement entropy (REE) in auxiliary-field quantum Monte Carlo methods [41, 42]. Challenges associated with the statistical convergence of the estimator in the importance sampling in the simulations gave rise to improved approaches [43, 44], and for the search of additional schemes where one could compute it reliably [45, 46], where, for example, it can now be established the subleading corrections to the area law in the REE within determinant quantum Monte Carlo (DQMC) for interacting fermions in the honeycomb lattice [47].

The study of band degeneracies in crystals continues to yield interesting physics. Semimetals are materials whose band degeneracies occur at points – nodal point semimetals – or along lines – nodal line semimetals (NLSMs) – in the Brillouin zone of otherwise gapped bands [48, 49]. The lower dimensionality of the Fermi surface of semimetals underpins a wide range of phenomena: from fundamental aspects involving topological charges [50], Fermi arcs [51], and chiral anomaly [52], to technological applications, notably for topological quantum computing [49] and for designs of quantum devices based on proximity effects [53].

Band degeneracies fall into two categories. A *symmetry-enforced* band degeneracy owes its existence solely to some set of crystal symmetries which must include at least one nonsymmorphic symmetry [54]. *Accidental* band degeneracies of one- or two-dimensional crystals require a combination of symmetries and tuning a microscopic parameter of the material. In three dimensions, the availability of sufficiently many tunable parameters leads to accidental band degeneracies even without symmetries [48], the nodes of Weyl semimetals being the most prominent instance.

Symmetry-enforced band degeneracies have been intensively investigated in the field of topological semimetals [55, 56, 57]. Symmetry-enforced NLSMs, in particular, have been predicted in various three-dimensional (3D) groups [58, 59]. We note that the presence of nonsymmorphic symmetries in the compounds falling in those groups is related to the presence of more than one type of atom in their unit cell.

Coming to 2D materials, hexagonal lattices [60], honeycomb-Kagome lattices [61], and PbFCl-type structures [62] have been reported to realize accidental NLSMs. These proposals suffer from accidental nodal lines being particularly fragile to perturbations in 2D, especially to spin-orbit coupling (SOC), which essentially prevents their utility in proximity-effect based devices. As an alternative to solid-state realizations, NLSMs have recently been reported in experiments of ultracold fermions in optical lattices [63], which offer an unprecedented possibility of engineering nodal lines and fine-tune correlations.

Despite the significant effort to understand the topological properties of semimetals, the role of electron-electron (e-e) interactions in these materials is less clear. Electronic correlations on NLSMs have been recently probed in ZrSiSe, showing a reduction of the Fermi velocity and a strong suppression of the Drude spectral weight due to short-range interaction effects [64]. Similar results have been obtained from angle-resolved photoelectron spectroscopy, which revealed a light-induced quasiparticle renormalization due to strong e-e interactions [65]. Other NLSM candidates also exhibit correlated properties, such as magnetism in HoSbTe [66] and A_2B_3 (A = Ti-Ni) [67], or superconductivity [68]. Theoretically, e-e interactions in NLSMs have been examined in connection to the emergence of phases with broken symmetry [69, 70, 71, 72, 73] and as corrections to physical quantities [74, 75].

Inspired by the myriad of possible effects present in strongly interacting systems, in this thesis we investigate thermodynamic, magnetic and transport properties of these systems. To investigate these phenomena, we study interacting Hamiltonians primarily through quantum Monte Carlo simulations. In Chapter 2 we introduce the Hubbard Hamiltonian,

explaining how it can be obtained from a generic Hamiltonian that contemplates electronic interactions, and the determinant quantum Monte Carlo, where we describe the procedure used to map an interacting Hamiltonian into a noninteracting one and how to obtain the quantities of interest from the Green's functions. In Chapter 3 we study the Hubbard model on a kagome lattice and obtain a value for a Mott-insulator transition and also discuss the possibility of adiabatically cooling the system. In Chapter 4 we attempt to utilize von Neumann entropy in order to locate the presence of a phase transition in the system previously described. In Chapter 5 we study the magnetic properties of the Hubbard model on a depleted honeycomb lattice and how these depletions affect the density of states in the noninteracting limit. In Chapter 6 we present the preliminary investigations about the effects of a time-dependent excitation on the bilayer Hubbard and t-J models. The last Chapter contains our concluding remarks.

Before closing this chapter it is important to mention that Refs. [76, 77, 78] are related to this thesis, and the contents of Chapter 6 will be submitted for publication soon. I have also contributed to Ref. [2] that is not part of this thesis.

Chapter 2

Determinant quantum Monte Carlo

In this Chapter we discuss details Hubbard model [79] used throughout this thesis to investigate interacting fermions subject to a repulsive onsite interaction. We will also discuss the implementation of the Determinant Quantum Monte Carlo (DQMC) method [41, 80, 81, 82, 83, 84, 85]. This method is efficient to investigate the properties of interacting Hamiltonians, such as the one just mentioned, at finite temperatures, which will be done in the following Chapters.

2.1 On-site interactions

The Hubbard model was developed in 1963 [79] to investigate ferromagnetism in metallic systems. In these systems electrons tend to be localized so that electron-electron interactions cannot be dismissed. Systems with this characteristics are said to be strongly correlated. The Hubbard model has been vastly used to study phenomena such as metal-insulating transitions, magnetism and non-conventional superconductivity.

To obtain the Hubbard Hamiltonian, we firstly consider a generic Hamiltonian that contemplates *e*-*e* interactions,

$$\begin{aligned}\mathcal{H} = &\sum_{\sigma} \int d^3r \psi^{\dagger}_{\sigma}(\mathbf{r}) \left[-\frac{\nabla^2}{2m} + U_{ion}(\mathbf{r}) \right] \psi_{\sigma}(r) \\ &+ \sum_{\sigma,\sigma'} \int d^3r \int d^3r' \psi^{\dagger}_{\sigma}(\mathbf{r}) \psi^{\dagger}_{\sigma'}(\mathbf{r}') V_{ee}(\mathbf{r}-\mathbf{r}') \psi_{\sigma'}(\mathbf{r}') \psi_{\sigma}(\mathbf{r}), \end{aligned} \tag{2.1}$$

with $V_{ee}(\mathbf{r}-\mathbf{r}') \propto \frac{1}{|\mathbf{r}-\mathbf{r}'|}$ being the Coulomb interaction between electrons ($\hbar = 1$) in a lattice. Throughout this thesis we will employ the second quantization formalism, where the creation operators are defined as

$$c^{\dagger}_{i\alpha\sigma} = \int d^3r \phi_{i\alpha}(\mathbf{r})\psi^{\dagger}_{\sigma}(\mathbf{r}), \tag{2.2}$$

with $\phi_{i\alpha}$ being the Wannier function of a given state and α represents the electronic orbitals. Its inverse relation is then

$$\psi^{\dagger}_{\sigma}(\mathbf{r}) = \sum_{i,\alpha} \phi^{*}_{i\alpha}(\mathbf{r}) c^{\dagger}_{i\alpha\sigma}. \tag{2.3}$$

Since $c^{\dagger}_{i\alpha\sigma}$ and $c_{i\alpha\sigma}$ are fermionic operators, they obey anticommutation relations,

$$\{c_{j\alpha\sigma}, c^{\dagger}_{l\beta\sigma}\} = \delta_{jl}\delta_{\alpha\beta}\delta_{\sigma\sigma'},\ \{c_{j\alpha\sigma}, c_{l\beta\sigma}\} = \{c^{\dagger}_{j\alpha\sigma}, c^{\dagger}_{l\beta\sigma}\} = 0. \tag{2.4}$$

Therefore, Eq. (2.1) can be rewritten in the Wannier basis as

$$\mathcal{H} = \sum_{ij\alpha\sigma} t^{\alpha}_{ij} c^{\dagger}_{i\alpha\sigma} c_{j\alpha\sigma} + \sum_{ijmn} \sum_{\alpha\beta\mu\nu} \sum_{\sigma\sigma'} \upsilon_{ijmn} c^{\dagger}_{i\alpha\sigma} c^{\dagger}_{j\beta\sigma'} c_{n\nu\sigma'} c_{m\mu\sigma}, \tag{2.5}$$

with the hopping between electrons being

$$t^{\alpha}_{ij} = \int \phi^{*}_{i\alpha}(\mathbf{r}) \left[-\frac{1}{2m}\nabla^2 + U_{ion}(\mathbf{r}) \right] \phi_{j\alpha}(\mathbf{r}), \tag{2.6}$$

and the Coulomb interaction being

$$\upsilon^{\alpha\beta\mu\nu}_{ijmn} = \int d^3r \int d^3r' \phi^{*}_{i\alpha}(\mathbf{r}) \phi^{*}_{j\beta}(\mathbf{r}') V_{ee}(\mathbf{r}-\mathbf{r}') \phi_{m\mu}(\mathbf{r}) \phi_{n\nu}(\mathbf{r}'). \tag{2.7}$$

If we assume a single orbital per site, the indexes α, β, μ and ν and their respective sums can be disregarded, resulting in

$$\mathcal{H} = \sum_{ij\sigma} t_{ij} c^{\dagger}_{i\sigma} c_{i\sigma} + \sum_{ijmn} \sum_{\sigma\sigma'} \upsilon_{ijmn} c^{\dagger}_{i\sigma} c^{\dagger}_{j\sigma'} c_{n\sigma'} c_{m\sigma}. \tag{2.8}$$

Finally, we are able to simplify Eq. (2.8), considering only onsite interactions and nearest-neighbor hoppings, resulting in

$$\mathcal{H} = -t \sum_{\langle ij \rangle} \sum_{\sigma} \left(c^{\dagger}_{i\sigma} c_{j\sigma} + c^{\dagger}_{j\sigma} c_{i\sigma} \right) + U \sum_{i} n_{i\uparrow} n_{i\downarrow}, \tag{2.9}$$

with $t = -t_{ij}$ representing the hopping amplitude between electrons and $U = v_{iiii}$ representing onsite repulsion. To study this system in the grand-canonical ensemble, it is necessary to include a term that tunes the electronic density. If we include the term $\mathcal{H}_\mu = -\mu \sum_{i\sigma} n_{i\sigma}$ to Eq. (2.9), we finally reach the Hubbard Hamiltonian

$$\mathcal{H} = -t \sum_{\langle \mathbf{i},\mathbf{j}\rangle,\sigma} \left(c^\dagger_{\mathbf{i}\sigma} c_{\mathbf{j}\sigma} + \text{H.c.}\right) - \mu \sum_{\mathbf{i},\sigma} n_{\mathbf{i},\sigma} + U \sum_{\mathbf{i}} n_{\mathbf{i},\uparrow} n_{\mathbf{i},\downarrow} \,. \tag{2.10}$$

The sums run over the lattice sites, with $\langle \mathbf{i}, \mathbf{j}\rangle$ denoting nearest-neighbor sites under periodic boundary conditions. Long-range interaction terms $v_{ijij} \neq 0$ may be included, but in this thesis we will focus on Eq. (2.10). Throughout this thesis the energy scale is defined in terms of the hopping and we set $t = 1$ unless otherwise mentioned.

2.2 Determinant quantum Monte Carlo

We now turn to the implementation of the DQMC method. Considering the Hubbard Hamiltonian found at the end of section 2.1. Its kinetic part is given by

$$\mathcal{H}_K = -t \sum_{\langle \mathbf{i},\mathbf{j}\rangle,\sigma} \left(c^\dagger_{\mathbf{i}\sigma} c_{\mathbf{j}\sigma} + \text{H.c.}\right) - \mu \sum_{\mathbf{i},\sigma} n_{\mathbf{i},\sigma} \,, \tag{2.11}$$

and its potential part is

$$\mathcal{H}_U = U \sum_{\mathbf{i}} n_{\mathbf{i},\uparrow} n_{\mathbf{i},\downarrow} \,. \tag{2.12}$$

While Eq. (2.11) can be easily diagonalized via a Fourier transform, the same is not true for Eq. (2.12), that is quartic due the density-density interaction. To diagonalize $\mathcal{H}_U$ we first must separate the kinetic and interaction parts of the Hubbard Hamiltonian, which we do by performing a Trotter-Suzuki decomposition on the partition function

$$e^{-\beta\mathcal{H}} = \left[e^{-\Delta\tau\ (\mathcal{H}_K + \mathcal{H}_P)}\right]^{L_\tau} \approx \left(e^{-\Delta\tau\ \mathcal{H}_K} e^{-\Delta\tau\ \mathcal{H}_U}\right)^{L_\tau} + \mathcal{O}(\Delta\tau^2). \tag{2.13}$$

This allows us to separate the exponentials of the single- and two-body terms, increasing the dimension of the system by one. The additional dimension corresponds to the

imaginary-time coordinate $L_\tau = \beta/\Delta\tau$, discretized by the inverse temperature $\beta \equiv 1/(k_B T)$ where k_B is the Boltzmann constant. The decomposition introduces an error proportional to $(\Delta\tau)^2$, being exact in the limit $\Delta\tau \to 0$. To ensure the statistical errors from the Trotter-Suzuki decomposition are negligible when compared to the Monte Carlo ones, we set $t\Delta\tau \leq 0.1$ throughout this thesis.

After decoupling the exponentials, we are left with the many-particle operator $e^{-\Delta\tau\ \mathcal{H}_U}$, which can be rewritten from a quartic form into a quadratic one by performing a Hubbard-Stratonovich transformation [80]. For the repulsive case, we have that the argument of the interaction exponential can be written as

$$e^{-\Delta\tau\ U n_{\mathbf{i}\uparrow} n_{\mathbf{i}\downarrow}} = \frac{1}{2} \sum_{s=\pm 1} e^{-\frac{1}{4}\Delta\tau U} e^{\alpha s (n_\uparrow - n_\downarrow)} \ , \tag{2.14}$$

with $\cosh\alpha = \exp\{(\Delta\tau U/2)\}$. The repulsive Coulomb interaction is replaced by discrete auxiliary fields $s(\mathbf{i}, \tau)$ coupled to the magnetization. We are then able to write the partition function as

$$\mathcal{Z} \propto \sum_s \prod_\sigma \det O^\sigma(s) \ , \tag{2.15}$$

with

$$O^\sigma(s) = \mathbb{1} + B^\sigma(L_\tau) B^\sigma(L_\tau - 1) \cdots B^\sigma(1) \ , \tag{2.16}$$

and

$$B^\sigma(l) \equiv e^{-\Delta\tau \mathcal{H}_K} e^{-\Delta\tau \mathcal{H}_U} . \tag{2.17}$$

The weight $P(s)$ of each configuration of auxiliary field is defined as

$$P(s) = \det\left[O^\uparrow O^\downarrow\right]. \tag{2.18}$$

The Green's functions can be computed by [86]

$$G^\sigma_{\mathbf{i},\mathbf{j}} \equiv \frac{1}{2^{2NL_\tau}} \sum_s [O^\sigma]^{-1}_{\mathbf{i},\mathbf{j}} \prod_\sigma O^\sigma(s) \ , \tag{2.19}$$

which can then be used to calculate the physical quantities of interest.

Among the physical quantities that will be calculated in the following Chapters, we have the occupation, that can be obtained from the Green's functions as

$$n = \sum_{\mathbf{i}} \sum_{\sigma} \langle c^{\dagger}_{\mathbf{i},\sigma} c_{\mathbf{i},\sigma} \rangle = \sum_{\mathbf{i}} \sum_{\sigma} (1 - G^{\sigma}_{\mathbf{i},\mathbf{i}}). \tag{2.20}$$

2.3 Minus sign problem

Defining the statistical weight as the product of determinants $P(s)$ can lead to problems since $P(s)$ is not positive definite. To avoid using a negative probability when computing a certain observable O, we can discard the negative sign by taking the absolute value $|P(s)|$ and multiplying it by its sign s. We then reweigh the average value of the observable by the average value of the determinant sign $\langle s \rangle$

$$\langle O \rangle = \frac{\sum_s |P(s)| \times s \times O}{\sum_s |P(s)| \times s} = \frac{\langle s \times O \rangle}{\langle s \rangle} \ . \tag{2.21}$$

When $\langle s \rangle \approx 1$, the quantities of interest can be obtained with no issues. However, in systems without particle-hole symmetry, $\langle s \rangle$ decreases rapidly in regimes with high values of U, low temperatures or for large sizes, introducing large fluctuations in the average calculations.

This phenomenon is known as the minus-sign problem. To reliably obtain the desired averages in regimes where $\langle s \rangle \to 0$, it is necessary to perform a high amount of Monte Carlo steps ($\geqslant 10^5$) to overcome the fluctuations. Although the sign problem limits the application of DQMC simulations, recent works [87, 88, 89] provide numerical evidence that the average of the determinant sign can be used to detect quantum critical points and their critical temperatures and/or exponents.

An example of system where this problem arises is the repulsive Hubbard model on the kagome lattice, which is the main topic of Chapter 3 and is also briefly seen in Chapter 4. This lattice can be divided in three sublattices, where the sites of each sublattice only interact with those belonging to the other two sublattices. As a consequence, the

kagome lattice has no particle-hole symmetry at any filling, thus displaying the minus-sign problem. In Fig. 2.1 we see how the average sign $\langle sign \rangle$ decreases as the temperature is

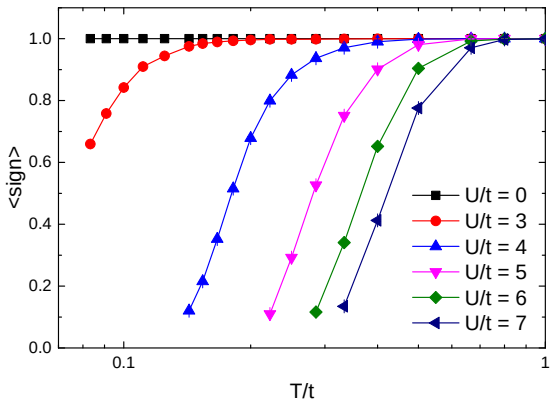

Figure 2.1: The average fermionic sign as a function of the temperature, for different values of U/t.

lowered. For higher U/t this decrease is more pronounced, limiting investigations as will be further discussed in Chapter 3.

Chapter 3

Repulsive Hubbard model on the kagome lattice

3.1 Introduction

From a theoretical point of view, the ground state properties of the Heisenberg model in the kagome lattice was extensively examined, with the nature of its QSL phase (gapped or gapless) being a matter under debate [90, 91]. However, this picture is less clear for the half-filled Hubbard model: many studies, using different techniques, agree on the occurrence of a Mott transition from a finite value of interaction, although controversies on the critical value remain. For instance, by using Variational Cluster Approximation (VCA), Yamada *et al* [92] examined the occurrence of a metal-to-insulator (MIT) transition as the interaction strength increases, finding a critical point at $U_c/t \approx 5$, while Higa *et al* [93] suggested that such a transition should occur at $U_c/t = 6.8$. Similarly, Ohashi *et al* [94] found this Mott transition around $U_c/t = 8.22$, using cellular dynamical mean field theory (CDMFT), while Variational Monte Carlo studies, conducted by Kuratani *et al* [95], exhibits $U_c/t \approx 11$. The lack of a consensus about U_c on these studies may be due to the particularities of their implementations, i.e. due to the way their biased input is added, and how it improves their ground states.

Unbiased methodologies are usually limited by technical issues, as the fermionic minus-sign problem for quantum Monte Carlo (QMC) approaches, or by dimensionality for

DMRG. Early attempts to perform finite temperature determinant QMC (DQMC) simulations were conducted by Bulut *et al*[96], without a clear evidence for a Mott transition. Recently, by combining dynamical vertex approximation, dynamical mean-field theory, and DQMC, Kaufmann *et al*[97] further examined how the magnetic correlation evolves in the kagome lattice, and proposed a critical point within a range of $U_c/t = [7, 9]$. On the other hand, DMRG results [98] provide evidence for two critical points, one for a translational symmetry broken insulator, and the other one to a QSL, at $U_{c1}/t \approx 5.4$ and $U_{c2}/t \approx 7.9$, respectively. Away from half-filling, physical responses are even less clear, with the enhancement of unconventional pairing correlations [99].

Despite these recent advances, much of the thermodynamic properties of the Hubbard model in the half-filled kagome lattice is unknown. Knowing the many different energy scales of the system would be particularly important to cold atoms experiments.

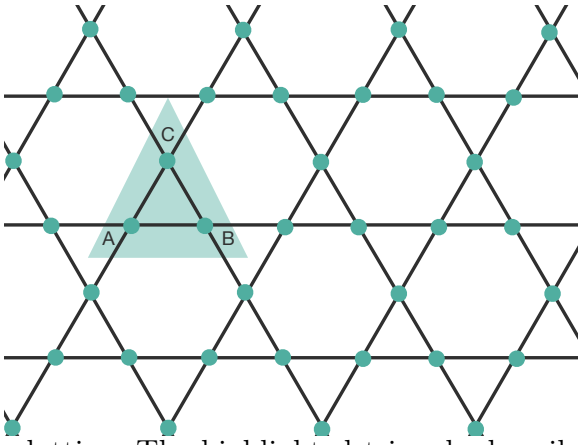

Figure 3.1: The kagome lattice. The highlighted triangle describes the unit cell with its A, B and C basis sites.

In this Chapter we study the repulsive Hubbard model on the kagome lattice, shown in Fig. 3.1. We perform a *tour de force* using the DQMC method to examine the thermodynamic, magnetic and transport properties of such a frustrated system. These analyses allow us to show the critical point within some accuracy, as well as unveiling hints about the ground state properties [100].

3.2 The repulsive Hubbard model

We investigate the thermodynamic properties of the repulsive Hubbard model Eq. (2.10) on the half-filled kagome lattice by performing determinant quantum Monte Carlo (DQMC) simulations, as discussed in Chapter 2. Here, we choose $t\Delta\tau \leq 0.05$, so that the error from the Trotter-Suzuki decomposition is negligible compared to that from the Monte Carlo sampling.

The kagome lattice is non-bipartite and has no particle-hole symmetry (PHS) for any filling, which may lead to a severe sign problem depending on the system size, temperature scale, and interaction strength, as discussed in Chapter 2. To further illustrate it, we replicate Fig. 3.2, previously shown in Chapter 2, that shows the average sign as a function of temperature T/t at half-filling on the kagome lattice, for the different U/t values, and for fixed linear size $L = 6$, i.e. $N = 6 \times 6 \times 3$ sites. Notice that the sign decreases as the temperature is lowered, and it is strongly suppressed as U/t increases (this behavior is more accentuated for larger system sizes). Therefore, the following results are obtained for $L = 6$, keeping $\langle \text{sign} \rangle \gtrsim 0.05$, which, for some cases, demand simulations up to 5×10^6 Monte Carlo sweeps for measurements. Similarly, unless otherwise indicated, the following results for the noninteracting case ($U/t = 0$) are obtained in the thermodynamic limit.

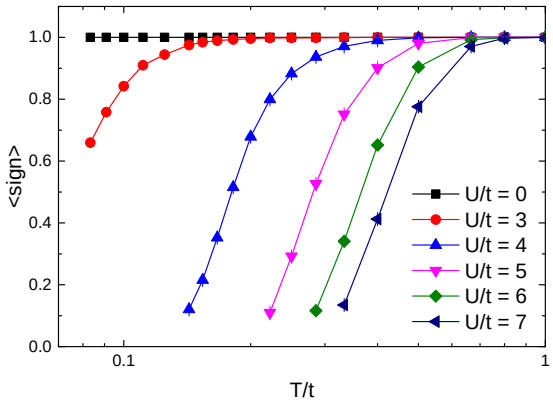

Figure 3.2: The average fermionic sign as a function of the temperature, for different values of U/t.

Another important feature of the kagome lattice is that, due to the absence of the

PHS, half-filling is not at $\mu = 0$. Therefore, one needs to vary the chemical potential in order to find which μ leads to $\langle n \rangle = 1$. Figure 3.3 shows how the chemical potential leading to a half-filled band at different U/t changes with temperature.

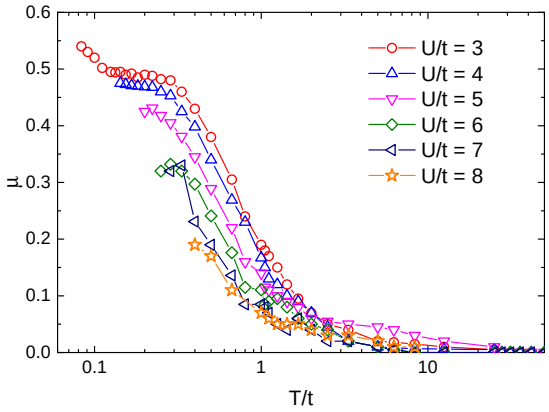

Figure 3.3: The chemical potential that leads to the half-filling of the system as a function of the temperature, and for different values of interaction strengths.

3.3 Results

3.3.1 Thermodynamic properties

We start our analysis by discussing the thermodynamic properties of the system. First, we investigate the internal energy density,

$$e(\beta, U) = \frac{1}{N}\langle \mathcal{H} \rangle, \tag{3.1}$$

which is shown in Fig. 3.4 (a). Given this, one is able to obtain the entropy per site (in units of the Boltzmann constant, k_B) by [101]

$$s(\beta, U) = \ln 4 + \beta e(\beta, U) - \int_0^\beta e(\beta', U) d\beta', \tag{3.2}$$

which is shown in Fig. 3.4 (b). We obtain $s(T \to \infty) \equiv \ln 4$ for all U/t, while it decreases and goes toward zero when T is reduced. However, the way $s(T) \to 0$ depends on the value of U/t. For instance, for $U/t = 3$, the entropy approaches zero in close similarity to the non-interacting case, while for $U/t = 7$ it decays slowly at low temperatures, directly affecting the specific heat, as discussed latter.

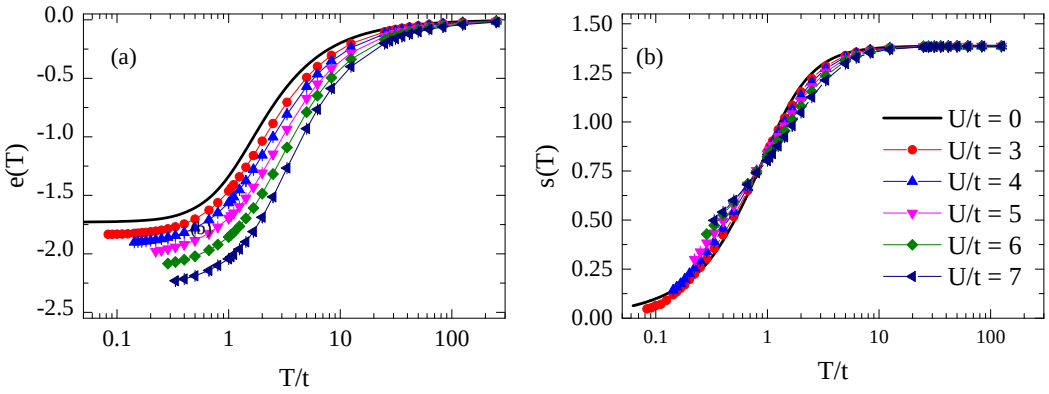

Figure 3.4: The (a) total energy, and (b) entropy as functions of the temperature, for different values of U/t. When not shown, error bars are smaller than symbol size.

Interestingly, the entropy curves for different values of the interaction strength cross around $s \approx \ln 2$. This crossing has also been observed for the square [102, 103, 104, 105] and honeycomb lattices, [104, 105, 106] and is closely connected with the possibility of adiabatical cooling in the system. That is, for entropies greater than $s \approx \ln 2$, Fig. 3.4 (b) shows that increasing U/t (at fixed entropy) pushes the temperature up. On the other hand, below $s \approx \ln 2$, increasing U/t at fixed entropy actually cools the system. At this point, we recall that this change of behavior should occur around an energy scale where the entropy of a Fermi liquid state becomes lower then the limit of the Heisenberg model (i.e., of localized spin-1/2). At high temperatures, the latter exhibits weakly interacting spins, which, in turn, leads to a crossing of entropies around $s \approx \ln 2$.

The adiabatic cooling/heating of the systems is shown in Fig. 3.5, which is constructed by selecting fixed values of entropy in Fig. 3.4 (b), and gathering the temperature for each U/t value. A comparison between the isentropic curves on the square [107], honeycomb[104] and kagome lattices is also presented and shows that, for low values of s, adiabatic cooling on the kagome lattice is at least as effective as in the honeycomb lattice. Further evidence of it is present below when investigating the behavior of the double occupancy at lower temperatures. In particular, for $s = 0.4$ it is possible to decrease the temperature in half by decreasing U/t within the limit investigated.

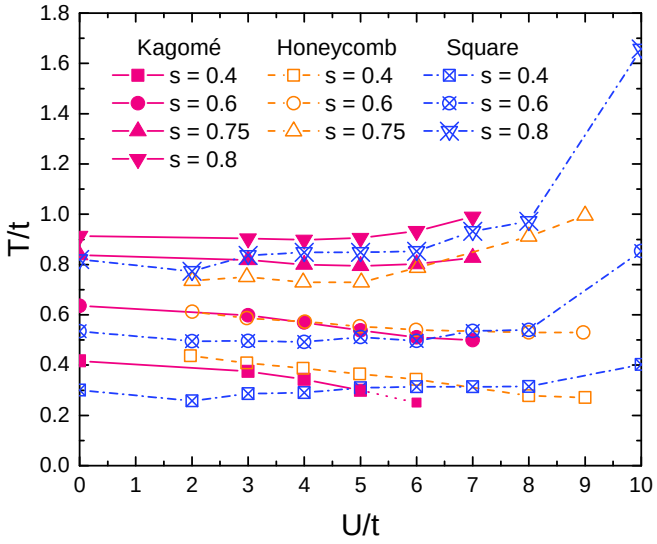

Figure 3.5: Isentropic curves as a function of U/t for the kagome (closed symbols), honeycomb (open symbols), and square (crossed symbols) lattices.

Figures 3.6 (a) and (b) display the behavior of the specific heat,

$$c(T) = \frac{1}{N}\frac{d\langle \mathcal{H} \rangle}{dT}, \tag{3.3}$$

for $U/t = 3$ and 6, respectively. The data points correspond to the differentiation of the raw QMC results in Fig. 3.4 (a), while the solid lines are obtained by differentiating a nonlinear fit of the energy; we use an exponential fit of the energy by the function $e_{fit}(T) = a_0 + \sum_{n=1}^{M} a_n \exp(-\beta n \Delta)$, with a cut-off in $M = 6$. Figure 3.6 (c) presents the specific heat from the exponential fit, for all values of U/t examined. For the noninteracting case, one notices the occurrence of a single peak around $T/t \approx 1$, which is pushed up to higher temperatures as U/t increases. Such a high-temperature broad peak is due to single-particle excitations and is closely related to the formation of local moments [102]. When the temperature is reduced a soft shoulder appears for all $U > 0$, but without a large second peak, as displayed in Fig. 3.6 (c). The occurrence of such low-temperature peak is usually due to low-lying collective spin-wave excitations, with the double-peak structure indicating strong spin-spin correlations [102]. Interestingly, by employing a cellular DMFT

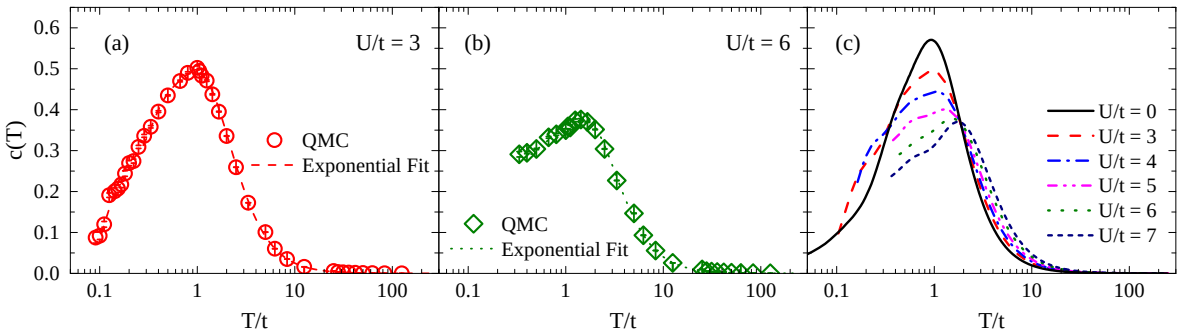

Figure 3.6: The specific heat as function of temperature for different values of U/t. The curves in panels (a) and (b) display a comparison between the numerical differentiation of the raw DQMC energy values and the differentiation of the exponential fit performed for $U/t = 3$ and $U/t = 6$, respectively. (c) The specific heat obtained from the exponential fit. When not shown, error bars are smaller than symbol size.

approach, Udagawa and Motome [108] obtained a small second peak for the specific heat at low temperatures, which they suggested is related to spin chirality degrees of freedom. In view of these issues, we further investigate the magnetic properties of the Hubbard model in the kagome lattice in the next subsection.

3.3.2 Magnetic properties

Now, we turn our attention to the magnetic properties of the system, starting our analysis with the double occupancy,

$$D = \frac{1}{3L^2}\left\langle \sum_{i,\alpha} n_{i\uparrow} n_{i\downarrow} \right\rangle. \tag{3.4}$$

The double occupation and the local moment are connected by $D = \frac{1}{2}\left[\langle n\rangle - \langle m^2\rangle\right]$, therefore for fixed n, increasing the local moment reduces the double occupancy. Figure 3.7 (a) displays D as a function of temperature, for different values of U/t, where one can notice that D has a sharp decrease for $1 < T/t < 10$ with a minimum (for all values of U) around $T/t \lesssim 1$. This minimum suggests a competition between localization and delocalization of the fermions. As depicted in Fig. 3.7 (b), when $T \to 0$ we find $\frac{\partial D}{\partial T} < 0$ for all U/t; a feature consistent with a metallic behavior. For $U/t = 7$, this minimum is shallow, while having a large local moment, which suggests an insulating or a bad metallic behavior. At

this point it is worth mentioning that metallic or insulating behavior is closely connected with of adiabatic cooling features. Indeed, since $\left(\frac{\partial D}{\partial T}\right)_{N,U} = -\left(\frac{\partial S}{\partial U}\right)_{N,T}$, when $\left(\frac{\partial S}{\partial U}\right)_{N,T} > 0$ – in the adiabatic cooling region –, then $\left(\frac{\partial D}{\partial T}\right)_{N,U} < 0$, which is consistent with a Fermi liquid at lower temperatures.

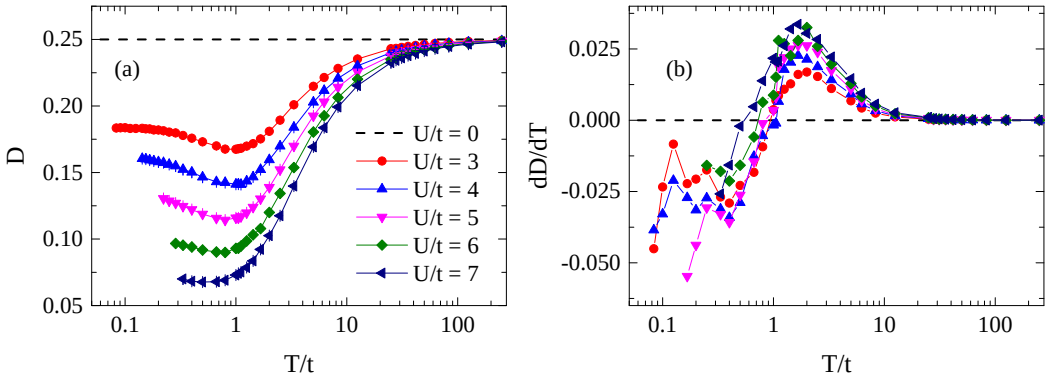

Figure 3.7: (a) Double occupancy and (b) its derivative as functions of the temperature for different U/t. The derivatives were smoothed through the usual methods. When not shown, error bars are smaller than the symbol size.

We proceed probing nonlocal spin-spin correlation functions

$$c^{\alpha\gamma}(\mathbf{i}-\mathbf{j}) = \frac{1}{3}\langle \vec{S}_{\mathbf{i},\alpha} \cdot \vec{S}_{\mathbf{j},\gamma} \rangle, \tag{3.5}$$

with $\vec{S}_{\mathbf{i},\alpha} = (S^x_{\mathbf{i},\alpha}, S^y_{\mathbf{i},\alpha}, S^z_{\mathbf{i},\alpha})$ being the spin operator of a fermion in given unit cell $\mathbf{i}$, and site index $\alpha = A$, B, and C. We first explore the nearest neighbors case $c(1)$, when $|\mathbf{i}-\mathbf{j}| = a$ (lattice parameter), i.e., the spin-spin correlations between the pairs of sites that form a triangle (see Fig. 3.1). Figure 3.8 (a), shows $c(1)$ averaged over all the combinations of near-neighbor pairs in the lattice. $c(1)$ is negative and increases in magnitude as U/t increases, i.e. there are strong spin-spin correlations along the sides of the triangle.

On the other hand, spin correlations for longer distances are suppressed, as displayed in Fig. 3.8 (b) for next-nearest neighbors [$c(2)$, when $|\mathbf{i}-\mathbf{j}| = 2a$], presenting values one order of magnitude smaller than those of $c(1)$. For $U/t \leq 4$, and at low temperatures, i.e. below the energy scale for local moment formation ($T/t \lesssim 2$), $c(2)$ is reduced to values very close to those of the non-interacting case, in line with a non-magnetic state. Interestingly,

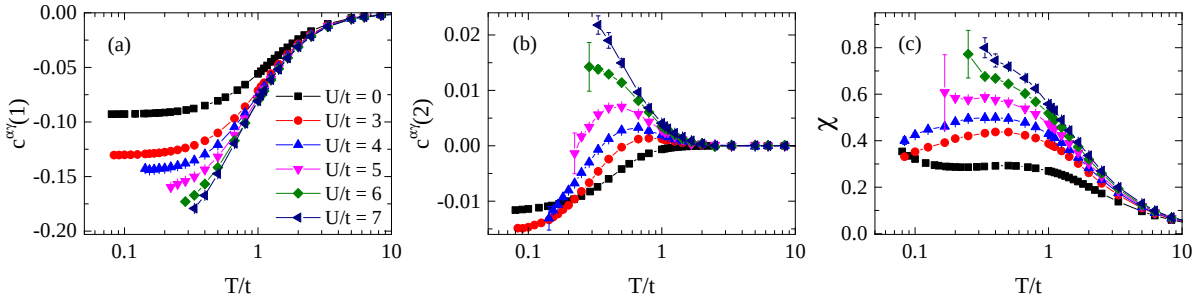

Figure 3.8: The spin-spin correlation between (a) nearest neighbors, (b) next-nearest neighbors and (c) the homogeneous magnetic susceptibility as functions of temperature for different values of U/t. When not shown, error bars are smaller than the symbol size.

for larger values of U, as for $U/t \geq 5$, $c(2)$ exhibits ferromagnetic correlations at high temperatures, and the effects of frustration (antiferromagnetic correlations) only set in for lower T/t. Finally, Fig. 3.8 (c) displays the homogeneous susceptibility as a function of temperature. For $U/t \lesssim 5$, $\chi(T)$ has a response similar to the non-interacting case, therefore being consistent with a metallic Pauli paramagnetic state, while for $U/t \gtrsim 6$ it has a monotonically increasing behavior as T decreases (within the temperature range we have analyzed). However, this increase in $\chi(T)$ with decreasing T for large interaction strengths is not enough to define the nature of the spin excitations. The minus-sign problem prevents us from reaching the very low temperatures required to determine if excitations are gapped or gapless.

3.3.3 Transport properties

Lastly, we now investigate the transport properties of the system, starting with the kinetic energy. Figure 3.9 displays the kinetic energy per site, $\langle \hat{K} \rangle = -\frac{t}{N} \left\langle \sum_{\langle \mathbf{i},\mathbf{j} \rangle,\sigma} \left(c^{\dagger}_{\mathbf{i}\sigma} c_{\mathbf{j}\sigma} + \text{H.c.} \right) \right\rangle$, as a function of temperature for different values of interaction. Since fermionic localization is favored in an insulating state, $\langle \hat{K} \rangle$ has to be reduced as a function of temperature as U increases, a feature noticed in Fig. 3.9. However, within the temperature scale we investigated, we did not find $\frac{\partial}{\partial T} \langle \hat{K} \rangle < 0$, therefore, different from the analysis of the potential energy, the behavior of the kinetic energy cannot provide clues on the emergence

of an insulating phase.

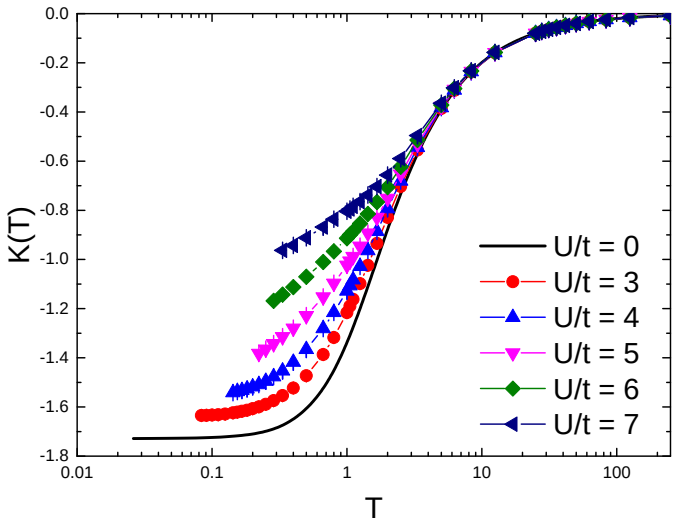

Figure 3.9: The average of the kinetic energy term as a function of the temperature for different values of U/t. When not shown, error bars are smaller than the symbol size.

In view of this, other quantities should be investigated to identify the metal-to-insulator transition. Among them, we proceed to examine the fermionic compressibility,

$$\kappa = \frac{1}{n^2}\frac{\partial n}{\partial \mu}, \tag{3.6}$$

with $n = \frac{1}{N}\left\langle \sum_{i,\sigma} n_{i\sigma} \right\rangle$, displayed in Fig. 3.10 (a). Notice that, due to the rotation symmetry, the three orbitals are equivalent, as well as their individual compressibilities. When dealing with any degree of anisotropy (of hopping or interaction), it is possible that some orbitals could be insulating while others exhibit metallic features, as an orbital-selective Mott phase. However, this is beyond the scope of this study.

For a metallic phase, κ assumes finite values, as presented in Fig. 3.10 (a) for the non-interacting case ($U = 0$). For the interacting case, in particular for $U/t \lesssim 5$, the system becomes less compressible, but the trend of κ is still consistent with a metallic phase. Otherwise, for an insulator state, a single-particle gap at the Fermi level of the density-of-states (DOS) is formed, leading to a plateau in $n(\mu)$ as the temperature is reduced, i.e. to $\kappa \to 0$. This behavior can be seen for $U/t \gtrsim 6$, where κ has a maximum in a

high-temperature scale, followed by an exponential suppression at lower temperatures, as depicted in Fig. 3.10 (a). In other words, there is a clear evidence to a metal-to-insulator transition from the behavior of the compressibility.

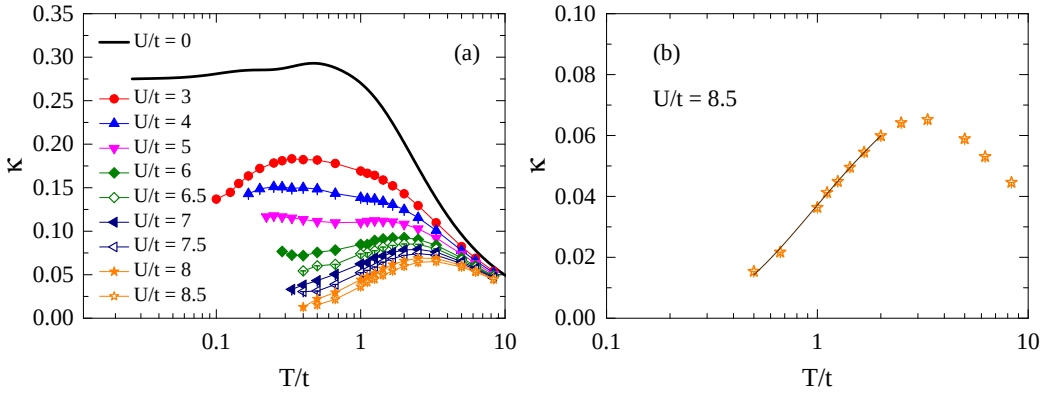

Figure 3.10: (a) The electronic compressibility as a function of the temperature, for different values of U/t. (b) The electronic compressibility for $U/t = 8.5$. Within the insulating state, $\rho(\mu)$ shows a plateau, which translates as an exponential decay in $\kappa(T)$. In order to find the charge gap Δ_c we fit the low-temperature data using $\kappa \propto \exp\left(\frac{-\Delta_c}{k_B T}\right)$ (dark line).

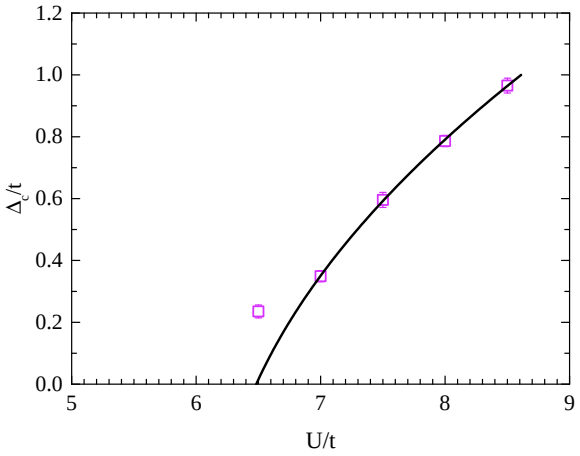

Figure 3.11: The charge gap, obtained through the compressibility data, as a function of U/t. When not shown, error bars are smaller than the symbol size.

We further investigate this change in the compressibility for $U/t \gtrsim 6$ by recalling that, within an insulating state, $\kappa \propto \exp\left(\frac{-\Delta_c}{k_B T}\right)$, with Δ_c being the charge/single-particle gap ($k_B \equiv 1$). Then, we obtain Δ_c by an exponential fit of the low-temperature data of κ for $U/t \geq 6.5$, as displayed in Fig. 3.10 (b). Assuming a second-order phase transition, and

performing an extrapolation by a polynomial or a power law function for $U/t \geq 7.0$, we obtain the critical point at $U_c/t = 6.5 \pm 0.1$, as shown by the black solid line in Fig. 3.11. Notice that the exponential fitting is not adequate when $\Delta_c \ll T$, which may lead to misleading results. Therefore, it is safe to disregard the point $U/t = 6.5$ when analysing the extrapolation.

At this point, some remarks are required. First, as the charge gap is formed at high temperature for $U/t \geq 7$, then we expect that our analysis for Δ_c in Fig. 3.10 (b) has little finite-size effects. Second, we have to recall that, in some circumstances, κ may exhibit unconventional behavior in multi-orbital systems, with the charge gap opening only for a few orbitals, while others remain metallic. However, such an orbital selective Mott transition does not occur in the Hubbard model on the kagome lattice; we have verified that the all orbitals are metallic or insulators.

The previous analysis of κ indirectly points out to a suppression of the spectral weight around the Fermi level. Given this, it is important to *directly* probe the density-of-states (DOS) as a complementary study. In order to avoid complex methodologies for numerical analytical continuations, here we examine the DOS only at the Fermi level, which is obtained through [109]

$$N(\omega = 0) \approx \frac{\beta}{\pi} G(|\mathbf{i} - \mathbf{j}| = 0,\ \tau = \beta/2). \tag{3.7}$$

Figure 3.12 (a) displays $N(\omega = 0)$ as a function of temperature for different values of U/t. Notice that $N(\omega = 0)$ exhibits a finite value for $U/t \lesssim 5$ at low-temperatures, consistent with a metallic state. By contrast, for $U/t \gtrsim 6$, the trend of the DOS has a significant change, being reduced exponentially, as expected for an insulator. In particular, within the range of temperatures examined, the behavior change occurs at $U/t \approx 6.5$, in very good agreement with the results for the compressibility.

Finally, as further evidence of a metal-to-insulator transition, we examine the dc con-

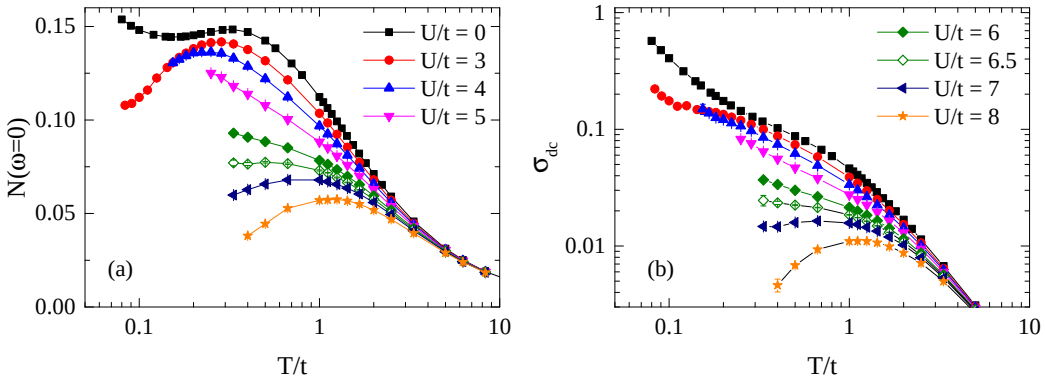

Figure 3.12: (a) The density-of-states at Fermi level, and (b) the dc conductivity as functions of the temperature, for different values of U/t. When not shown, error bars are smaller than the symbol size.

ductivity,

$$\sigma_{dc} = \frac{\beta^2}{\pi}\Lambda_{xx}(\mathbf{q}=\mathbf{0}, \tau=\beta/2), \tag{3.8}$$

in which

$$\Lambda_{xx}(\mathbf{q},\tau) = \langle j_x(\mathbf{q},\tau) j_x(-\mathbf{q},0)\rangle, \tag{3.9}$$

with $j_x(\mathbf{q},\tau)$ being the Fourier transform of the unequal-time current-current correlation functions

$$j_x(\mathbf{i},\tau) = \mathrm{e}^{\tau\mathcal{H}}\left[it\sum_{\sigma}\left(c^{\dagger}_{\mathbf{i}+\mathbf{x}\sigma}c_{\mathbf{i}\sigma} - c^{\dagger}_{\mathbf{i}\sigma}c_{\mathbf{i}+\mathbf{x}\sigma}\right)\right]\mathrm{e}^{-\tau\mathcal{H}}; \tag{3.10}$$

see, e.g., Refs.[110, 111, 112]. Figure 3.12 (b) exhibits the results for σ_{dc} as a function of temperature for different values of U/t. Similarly to the previous analyses, a metallic behavior, i.e. $\partial\sigma_{\mathrm{dc}}/\partial T < 0$, occurs only for $U/t \lesssim 6.5$. For interaction strength larger than that, the behavior is consistent with an insulator.

In summary, the analyses of the compressibility, the DOS at the Fermi level, and the dc conductivity provide strong evidence for a metal-to-insulator transition at $U_c/t = 6.5\pm0.5$.

3.3.4 Finite-size effects

In this subsection, we investigate finite-size effects. To this end, we perform simulations for a $N = 10\times10$ lattice (i.e., with 300 sites), fixing $U/t = 6$, while varying temperature.

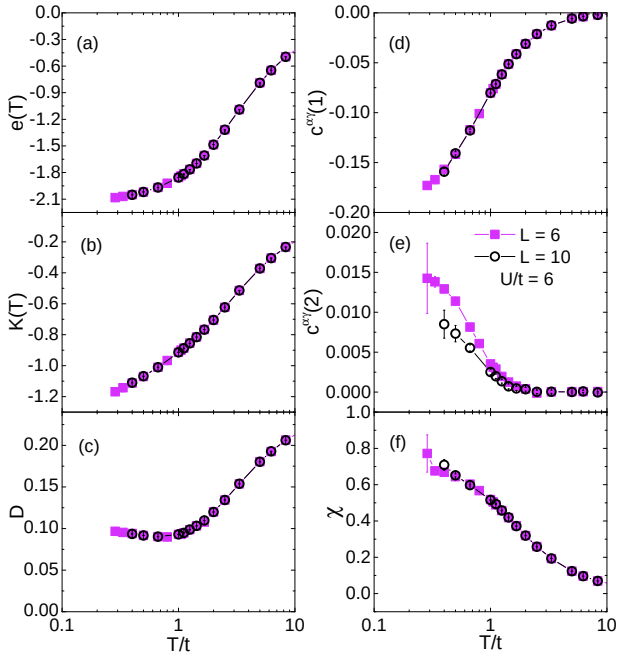

Figure 3.13: Comparison between results obtained for 6×6 (filled squares) and 10×10 (open circles) lattices for (a) the total energy, (b) the kinetic energy, (c) the double occupancy, (d) nearest and (e) next-nearest-neighbors spin-spin correlation functions, and (f) homogeneous susceptibility as functions of the temperature, at $U/t = 6$. When not shown, error bars are smaller than symbol size.

Figure 3.13 displays (a) the total energy, (b) the kinetic energy, (c) the double occupancy, and (d) nearest neighbors spin-spin correlation functions for this system size, comparing it with our previous results for $N = 6 \times 6$. Notice that, for these quantities, finite-size effects may be disregarded within the range of temperature examined. Indeed, short-ranged quantities must suffer much less from finite-size effects than long-ranged quantities, as structure factors or susceptibilities. Concerning the latter, NNN spin correlation functions and the homogeneous magnetic susceptibility exhibit a small dependence on the lattice size at low temperatures, as shown in Figs. 3.13 (e) and (f), respectively. However, these minor dependencies do not affect the main results discussed in the previous subsections.

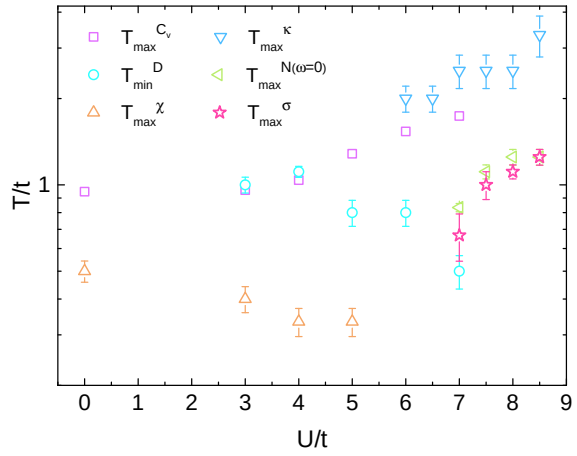

Figure 3.14: Different energy scales for the Hubbard model on the kagome lattice, for several values of U/t.

3.4 Temperaure scales

Our work presents a detailed finite-temperature analyses for the Hubbard model in the kagome lattice, allowing us to provide different energy scales of the system. To this end, Fig. 3.14 presents [i] the minima of the double occupancy $T^D_{\rm min}$, as well as the high-temperature maxima for [ii] the specific heat peak $T^c_{\rm max}$, [iii] the magnetic susceptibility $T^\chi_{\rm max}$, [iv] the compressibility $T^\kappa_{\rm max}$, [v] the DOS at Fermi level $T^N_{\rm max}$, and [vi] the dc conductivity $T^\sigma_{\rm max}$. Together, Figs. 3.5 and 3.14 provide a broad description of the model, that can be relevant to future cold atom experiments.

The contents presented up until this section appear in Ref. [76].

3.5 Lieb-Kagome

We have examined the Hubbard model on a kagome lattice with hopping anisotropy, allowing us to continuously interpolate between the unfrustrated Lieb lattice and the fully frustrated kagome lattice. This interpolation is achieved by varying the hopping amplitude, $0 \leqslant t' \leqslant 1$, along one of the diagonals of the kagome lattice, as shown in Fig. 3.15

In order to understand the magnetism we investigated the spin-spin correlation func-

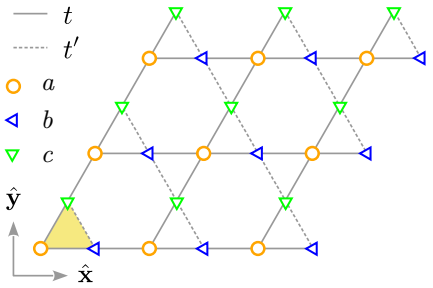

Figure 3.15: The kagome lattice, with basis sites a, b and c. By adjusting the hopping between sites b and c so that $t' = 0$, one reaches the Lieb lattice. From Ref. [2]

tions. In the Lieb limit ($t'/t = 0$), the local moment differed between sites, being more intense in sites b and c than on sites a, reflecting that hoppings are more likely to involve sites a than the other two. This difference vanishes in the kagome limit ($t'/t = 1$), as expected. The NN spin-spin correlation functions change sign as t'/t increase, going from positive when $t'/t = 0$ to negative as $t'/t \to 1$, as can be seen in Fig. 3.16. This is an indication of the transition from the ferrimagnetic behavior seen in the Lieb lattice to the antiferromagnetic one expected in the kagome limit. We use this change in sign to mark the boundary for the ferrimagnetic state in the phase diagram shown in Fig. 3.18, whose points are denoted by U_c^F/t. The error in this estimate is provided by the grid of t'/t values we used ($\Delta t' = 0.2$). These analyses were corroborated by an analysis of the uniform susceptibility.

The electronic compressibility was investigated through an analysis similar to the one described in Subsection 3.3.3. In Fig. 3.17 (a)-(d) is the electronic compressibility for all t' investigated. Here it can be seen that κ decays exponentially in the low-temperature regime, similarly to what was observed in Subsection 3.3.3. This allows us to obtain the charge gap Δ_c, shown in Fig. 3.17 (e), which we then use to mark the boundary of the metallic region in the phase diagram in Fig. 3.18, whose points are denoted by U_c^M/t.

The contents of this section appear in Ref. [2], which is not a part of this thesis.

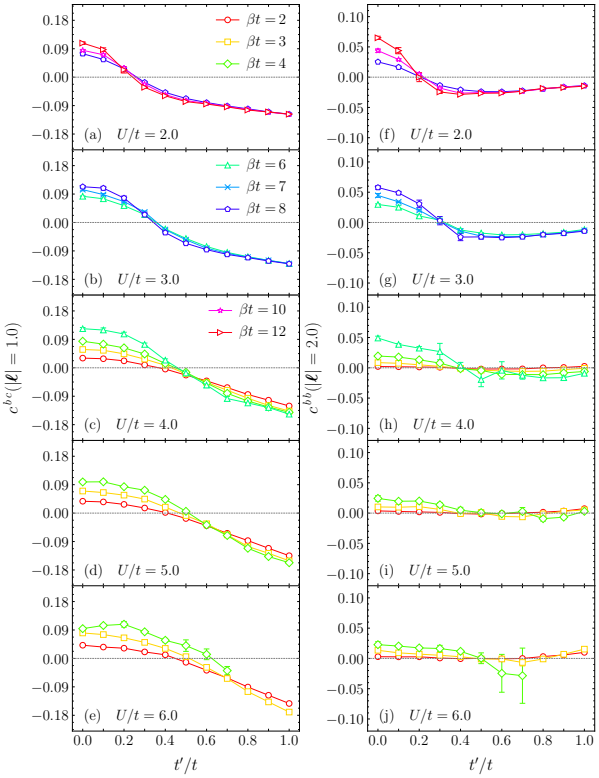

Figure 3.16: Correlations between spins on nearest neighbor b-c sites (left panels), and spins on next-nearest b-b sites along dashed t'-lines (right panels), as functions of t'/t. Panels (a)-(e) [(f)-(j)] show data for increasing values of U/t, and the curves in each panel correspond to different inverse temperatures, βt. From Ref. [2]

3.6 Conclusions

We have investigated the repulsive Hubbard model's thermodynamic, magnetic, and transport properties on the isotropic and anisotropic kagome lattice through unbiased DQMC simulations.

Starting from the investigation of the thermodynamic properties of the isotropic case, we examined the entropy for different interaction strengths and the behavior of the isentropic curves as a function of U/t. We have found that adiabatical cooling is possible for entropies smaller than $s \approx \ln 2$. In addition, we examined the specific heat: in contrast to what is seen in the Hubbard model at the square or honeycomb lattices, the low-temperature peak seems to be suppressed in the kagome lattice for all U/t. This suggests the absence of collective spin-wave excitations as temperature is reduced, i.e. the absence

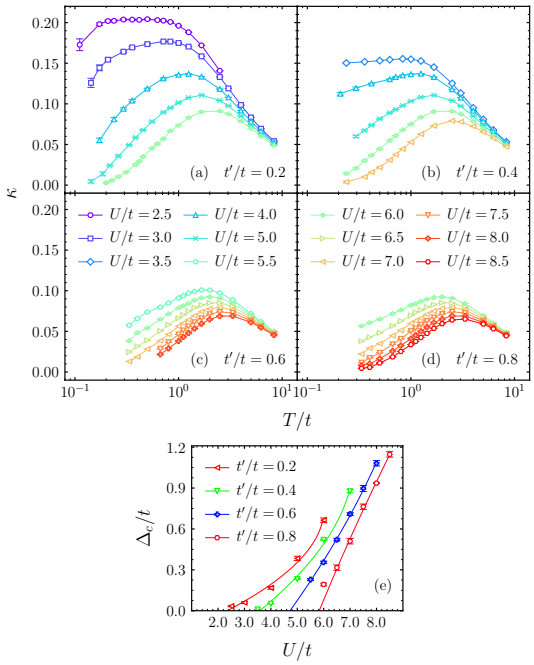

Figure 3.17: Panels (a)-(d): Compressibility as a function of temperature (we set the Boltzmann constant $k_B = 1$), for fixed values of t'/t, and different values of U/t. (e) gap estimates from fittings to $\kappa \propto \exp\{(-\beta\Delta_c)\}$, using the low temperature data of panels (a)-(d); see text. The lines are parabolic fits to the curves. From Ref. [2].

of magnetic long-range order in the ground state.

In view of this, we investigated the spin-spin correlation functions, in particular the local moment, nearest (NN), and next-nearest neighbors (NNN). We obtained well-formed local moments, with strong short-range NN correlations functions, while the NNN (and farther) ones are strongly suppressed, further evidencing the absence of magnetic long-range order. Despite this, the homogeneous magnetic susceptibility $\chi(T)$ still increases as temperature is reduced, being enhanced for larger values of U/t. However, we are not able to conclude whether the nature of the spin excitations is gapped or gapless since the sign problem prevents us from reaching lower temperatures. Furthermore, it is worth mentioning that identifying whether a spin liquid state emerges or not is challenging, and beyond the scope of this work.

Finally, we probed the metal-to-insulator transition. In particular, the behavior of the compressibility provides a clear distinction between metallic and insulating states. There-

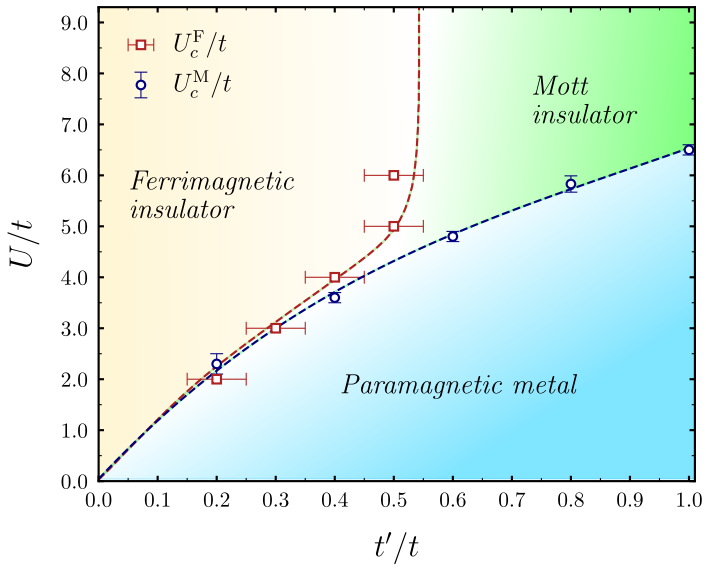

Figure 3.18: Phase diagram of the Hubbard model on the anisotropic kagome lattice at half-filling. From Ref. [2].

fore, we investigated the behavior $\kappa(T)$ for different values of U/t, being able to identify the critical point around $U_c/t \approx 6.5$. As complementary analyses, we also examined the DOS at the Fermi level, as well as the current-current correlation functions, leading to results in line with those from the compressibility. Together, these analyses provide clear evidence for a Mott transition at $U_c/t = 6.5 \pm 0.5$.

In the anisotropic case, we found that a metal-insulator transition takes place at a certain $U_c^{\mathrm{M}}/t(t'/t)$, which increases monotonically with t'/t, from $U_c^{\mathrm{M}}/t(0) = 0.0$. We also found that by increasing the frustration, mediated by t'/t, the system transitions between a ferrimagnetic phase and a Mott phase.

Chapter 4

Single-site von Neumann entropy as a marker for quantum phase transitions at non-zero temperatures

4.1 Introduction

Entanglement, a key property of quantum mechanics, is considered a fundamental asset for quantum information processes such as computation and communication, thus crucial for the development of quantum technologies [113, 114, 115, 116]. Condensed matter systems are particularly promising for quantum technology devices due to their inherent quantum fluctuations [117, 118, 119, 120].

Aside from its application in characterizing quantum phases, another important feature of entanglement is that it has been associated with the magnetic susceptibility [121, 122, 123, 37], a thermodynamic observable that could thus be used for estimating entanglement experimentally, as in spin chains systems formed by the compounds $Na_2CU_5Si_4O_{14}$ [121] and $Cu(NO_3)_2 \times 2.5H_2O$ [122]. In the context of quantum phase transitions, studies in homogeneous one-dimensional Hubbard chains at zero temperature have shown that the entanglement entropy is directly connected to the susceptibility [123] and that there are regimes at which this relation is linear and universal [37], suggesting that entanglement could be estimated experimentally via magnetic susceptibility measurements.

Here, we investigate whether the von Neumann entropy at $T \neq 0$ can still define bi-

partite entanglement and/or be used to identify and characterize Mott metal-insulator transitions (MITs) in two-dimensional lattices. That is, if signatures of the $T = 0$ quantum phase transition can be recognized at finite temperatures, while also analyzing the connection between entanglement and magnetic susceptibility at $T \neq 0$. We consider the Hubbard model on the honeycomb and kagome lattices, and the ionic Hubbard model on the square lattice, using DQMC to calculate the single-site entanglement at half-filling in all cases. Our results reveal that obtaining the transition points previously encountered in the literature for all the lattices is possible. Our findings thus demonstrate that the entanglement entropy signals quantum phase transitions to a Mott state, even at finite temperatures ($T \neq 0$). Additionally, for all the geometries studied, we find regimes at which entanglement and susceptibility are linearly related: this could then be used to estimate entanglement in experiments via susceptibility measurements.

4.2 Model and Methodology

4.2.1 Ionic Hubbard model

In this Chapter we study the Hubbard model, presented in Chapter 2, on the honeycomb and kagome lattices shown in Fig. 4.1 (a) and (b), respectively.

We also investigate the ionic Hubbard model on a square lattice; its Hamiltonian reads:

$$\hat{\mathcal{H}}_{\text{ionic}} = \hat{\mathcal{H}} + \Delta \sum_{\mathbf{i}} (-1)^{\mathbf{i}} \hat{n}_{\mathbf{i}} \ , \tag{4.1}$$

which differs from Eq. (2.10) by adding a term that differentiates the two sublattices of the square lattice [shown in green and blue in Fig. 4.1 (c)], by adding (subtracting) an onsite energy Δ to even (odd) sites.

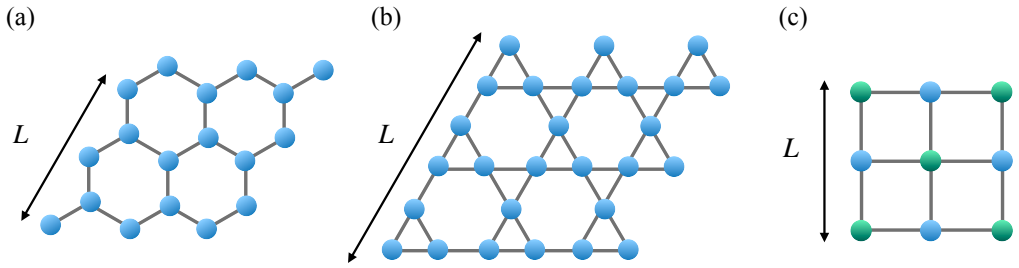

Figure 4.1: Schematic representation of the honeycomb (a), kagome (b), and square (c) lattices used, with $N = 2L^2, 3L^2$ and L^2 sites, respectively ($L = 3$ here). The latter exhibits a breaking of sublattice symmetry associated with the ionic Hubbard model, identified by the different colors.

4.2.2 Single-site entanglement

Among the various entanglement measures [124], the von Neumann entropy [125], part of the general class of Renyi entropies [126, 127], stands out as an efficient tool to quantify the entanglement of bipartite pure states. One particular approach to the von Neumann entropy is the *single-site* entanglement, which has been extensively explored in the one-dimensional Hubbard model [123, 21, 22, 128, 33, 129, 130, 36, 131, 132]. In this case, the calculated entanglement is between a single site and the rest of the system. This measure is particularly relevant when it is possible to control and detect single particles in quantum systems, such as in cold atoms [133, 134]. For a single site i, the entanglement with the remaining $N-1$ sites is then [34, 37]

$$S_i = -\frac{1}{\log_2 d} Tr[\rho_i \log_2 \rho_i] \tag{4.2}$$

where $\rho_i = \mathrm{Tr}_{\{N-i\}}\rho$ is the reduced density matrix, ρ is the ground state's total density matrix [21], d is the Hilbert space dimension and $1/\log_2 d$ is the normalization factor. As we are considering a single site, the local Hilbert space has $d = 4$, considering the four possibilities $|\uparrow\rangle$, $|\downarrow\rangle$, $|\uparrow\downarrow\rangle$, and $|0\rangle$. In particular, S_i can be rewritten in terms of the

occupation probabilities [22, 123, 135, 36] as

$$S_i = -\frac{1}{\log_2 d}[\omega_{i,\uparrow}\log_2\omega_{i,\uparrow} + \omega_{i,\downarrow}\log_2\omega_{i,\downarrow} + \omega_{i,\uparrow\downarrow}\log_2\omega_{i,\uparrow\downarrow} + \omega_{i,0}\log_2\omega_{i,0}], \tag{4.3}$$

where the single occupation probability, owing to the SU(2) symmetry of the studied models, is the same for spin up and spin down and is given by $\omega_{i,\uparrow} = \omega_{i,\downarrow} = \langle\hat{n}_i\rangle/2 - \omega_{i,\uparrow\downarrow}$, where $\omega_{i,\uparrow\downarrow} = \langle\hat{n}_{i,\uparrow}\hat{n}_{i,\downarrow}\rangle$ is the double occupancy probability at site i, and $\omega_{i,0} = 1 - \langle\hat{n}_i\rangle + \omega_{i,\uparrow\downarrow}$ is the empty occupation probability. It is interesting to note that $\langle\hat{n}_{i,\uparrow}\hat{n}_{i,\downarrow}\rangle$ and $\langle\hat{n}_i\rangle$ can be easily obtained from DQMC simulations.

Notice that S_i is zero whenever one of the probabilities is one (with the remaining being zero), i.e., when the reduced system is in a pure state. For the Hubbard model, this occurs in the vacuum state $n \equiv \sum_i\langle\hat{n}_i\rangle = 0$ (thus $\omega_{i,0} = 1$) or at full-filling $n = 2$ ($\omega_{i,\uparrow\downarrow} = 1$). The maximum entanglement, $S_i = 1$, occurs for the maximally mixed reduced system. This is the case when all four probabilities are equivalent, $\omega_i = 1/4$, which occurs at $n = 1$ and $U = 0$ [136]. At half-filling, in the presence of repulsive interactions ($U > 0$), the single occupation probabilities reach $\omega_\uparrow = \omega_\downarrow = 0.5$ as $U \to \infty$, and the double and empty probabilities tend to zero, leading to $S_i = 0.5$. This remaining entanglement is then attributed to spin degrees of freedom.

To improve statistics in our calculations, we consider the average over all sites $S \equiv \frac{1}{N}\sum_i^N S_i$, [37, 124] for the honeycomb and kagome lattices, thus obtaining a global measure representing the whole system. For the ionic Hubbard model on a square lattice, separate averages are performed in the two sublattices. The presence of a quantum critical point at $T = 0$ produces a cone of fluctuations that can still be perceived at low enough temperatures, suggesting that obtaining a signature of a quantum phase transition as a proxy at finite temperatures of S might be possible.

4.2.3 Systems

We calculate the average single-site entanglement S for the Hubbard model in honeycomb and kagome lattices and for the ionic Hubbard model in the square lattice. These systems

have been previously studied and present correlation-driven quantum phase transitions.

The repulsive Hubbard model in the honeycomb lattice [Fig. 4.1(a)] is known to display a quantum phase transition from a paramagnetic semimetal to an antiferromagnetic Mott insulator at half-filling [106, 5, 137] at $U_c/t \approx 3.8$. This bipartite geometry allows the possibility of particle-hole symmetry (PHS), which ensures that the behavior of quantities that depend on the electronic density is mirrored around the half-filling. Thus, it is sufficient to restrict the analysis to either above or below this point. We perform DQMC simulations on a honeycomb lattice of linear size $L = 9$ ($\mathrm{N} = 2 \times 9 \times 9$ sites) unless otherwise specified.

The absence of bipartite symmetry in the kagome lattice [Fig. 4.1(b)] leads to a decoupling between the onset of insulating behavior and magnetic ordering with increasing interactions. The existence of an MIT in the kagome Hubbard model has been extensively investigated. Besides the discussion presented in Chapter 3, it is important to report that on small-radius cylinder geometries, where the density-matrix renormalization group (DMRG) method is especially suitable, characterization of the onset of insulating behavior was established at $U_c/t \simeq 5.4$ [98]. Owing to the absence of PHS for any filling in the kagome lattice, which, as mentioned in Chapters 2 and 3, leads to the minus-sign problem and limits the temperatures that can be accessed within DQMC, here, we focus the DQMC simulations on a kagome lattice of size $L = 6$ ($N = 3 \times 6 \times 6$ sites).

The Hubbard model on a square lattice has a quantum phase transition at half-filling from a metallic paramagnet to an antiferromagnetic insulator as soon as the interactions are turned on. The transition is driven by the instability caused by the van Hove singularity and also by the presence of nesting [42, 138]. As finite-size effects are stronger for smaller U, and the gap is exponentially small in this regime, observing the transition through entanglement for the Hubbard model on a square lattice, where $U_c = 0$, is challenging.

Therefore, to study the phase transition in the square lattice we turn our attention to

the ionic Hubbard model, where two phase transitions, driven by the on-site interaction U at a finite Δ [139, 140, 141, 142] take place. The presence of Δ at weak interactions ($U/t \leq \Delta$) drives the system into a band insulating phase (BI). As U increases, a metallic phase is found on a 2D square lattice [140, 143], whereas at large U values, the system becomes a Mott insulator (MI) [144]. Although the exact value of U where the Mott transition takes place is not well established, it is known that for $\Delta/t = 0.5$ at half-filling, the system undergoes a band-insulator-to-metal transition at $U/t = 2.0$ [140, 141, 89]. Thus we perform DQMC simulations for a half-filled ionic square lattice with $\Delta = 0.5$ [Fig. 4.1(c)] of linear size $L = 10$ ($N = 10 \times 10$ sites).

In what follows, we calculate the single-site entanglement, in particular investigating how it varies with the electronic density n, in Sec. 4.3.1, and with the Hubbard interaction U/t, in Sec. 4.3.2. The goal is to find regimes of parameters where indications of phase transitions emerge and compare the critical points obtained in previous studies. Thus, we aim to identify the reliability of the entanglement entropy calculated at $T > 0$ as a probe for quantum phase transitions in two dimensions.

4.3 Results

4.3.1 Single-site entanglement as a function of the electronic density

We start by investigating the dependence of the entanglement entropy S with the electronic density n at $T/t = 0.5$, in Fig. 4.2. The non-interacting limit shows a maximum of $S = 1$ at $n = 1$, consistent with the expectation that, at this regime, the system is metallic and each state has equal probability, i.e., $\omega_i = 1/4$, leading to maximum entanglement. As U/t increases, the entanglement starts to decrease, and the curve eventually changes into two maxima with a dip at $n = 1$. The appearance of a dip at half-filling signals a transition from the physics of itinerant electrons to that of localized moments, and it is interpreted as a marker of a Mott phase with increasing U/t [135, 37]. In the opposite limit,

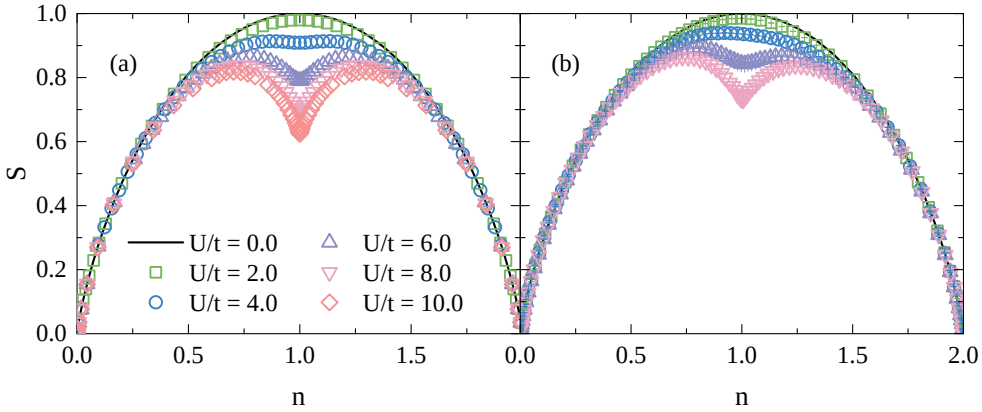

Figure 4.2: Single-site entanglement S as a function of the electronic density n for different values of U/t at $T/t = 0.5$, for the (a) honeycomb and (b) kagome lattices.

$U \to \infty$, the average single-site entanglement reaches the minimum $S = 0.5$ at $n = 1$, as charge degrees of freedom are frozen and only spin degrees of freedom remain [31]. It is worth pointing out that the two resulting domes in the curves for high U/t are symmetric around $n = 1$ for the honeycomb lattice, but not for the kagome lattice, due to the presence or absence of PHS in these systems.

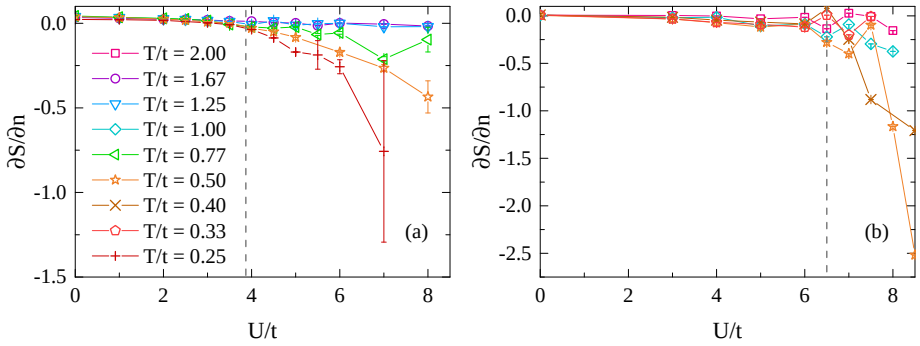

Figure 4.3: The derivative of the single-site entanglement with respect to n as a function of U/t for the (a) honeycomb and (b) kagome lattices and different temperatures. Here, the derivative is performed by varying the density near half-filling. The grey dashed lines indicate the U_c for these lattices.

To monitor the temperature effects in our results, we investigate the derivative $\partial S/\partial n$ around half-filling for different T's as shown in Fig. 4.3. We perform the derivative by varying the density around $n = 1$, for both geometries. For lower values of T/t, $\partial S/\partial n = 0$ for $U < U_c$ whereas $\partial S/\partial n \neq 0$ for $U > U_c$. This is consistent with the fact that

in a metallic phase, there are no significant changes in the non-local correlations when adding/subtracting a particle to/from the system, while in the insulating phase, quantum correlations become more susceptible to the addition/subtraction of particles [22]. This change in regimes happens when U/t is increased beyond the critical values U_c indicating that $\partial S/\partial n$ can signal the MIT. However, when T/t increases, the entanglement entropy response becomes less evident, suggesting that for $T/t \gtrsim 1$ the thermal fluctuations are intense enough to wash away the effects of the quantum phase transition.

4.3.2 Single-site entanglement as a function of interaction strength

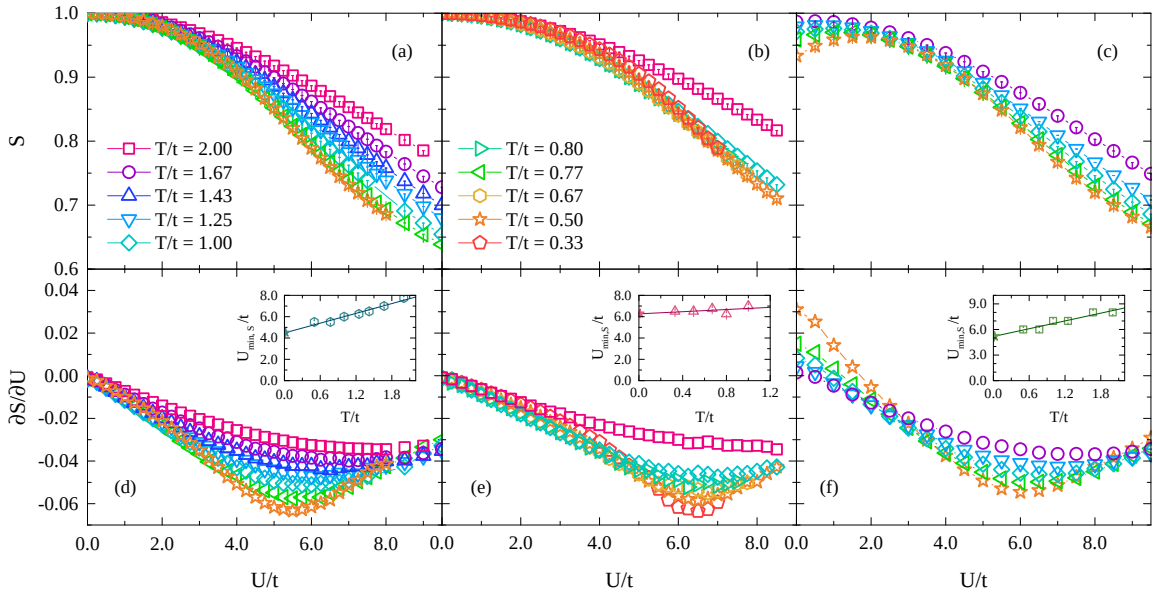

Figure 4.4: Average single-site entanglement S as a function of on-site interaction U/t for (a) honeycomb, (b) kagome, and (c) ionic square lattices, contrasting different temperatures at half-filling ($n = 1$). The decrease of S at large U reflects the localizing tendency of the electrons in this regime. Panels (d), (e), and (f) show the corresponding derivatives with respect to the interaction strength. The minima signal a finite-T proxy of the onset of insulating behavior – its temperature dependence is shown in the insets. The lines correspond to linear fits from which the critical values at $T = 0$ (U_c/t) are extracted, resulting in $U_c/t = 4.5(2)$ for the honeycomb lattice, $U_c/t = 6.3(4)$ for the kagome lattice, and $U_c/t = 5.2(3)$ for the ionic square lattice, depicted by the star markers in the corresponding insets.

Focusing on half-filling where the Mott transition occurs, we now investigate the Hub-

bard interaction U effects on S. Figure 4.4 shows that the honeycomb [Fig. 4.4(a)] and kagome lattices [Fig. 4.4(b)] display similar behavior, where the entanglement is maximum in the non-interacting regime while decaying monotonically with increasing U/t. This happens as a consequence of the zero and double occupancies, $\omega_{i,0}$ and $\omega_{i,\uparrow\downarrow}$, decreasing while the single occupancies, $\omega_{i,\sigma}$, increase and indicate a localizing tendency of the electrons. In contrast, S displays a non-monotonic behavior for the ionic Hubbard model, increasing with U until $U/t \simeq 2$ and then decreasing as the Hubbard correlation further increases – it directly derives from a competition between Δ and U. In particular, this model presents a phase transition from a band insulator to a metal for $\Delta/t = 0.5$ at $U/t \simeq 2$ [143, 89], in agreement with the maxima observed at low temperatures in Fig. 4.4(c).

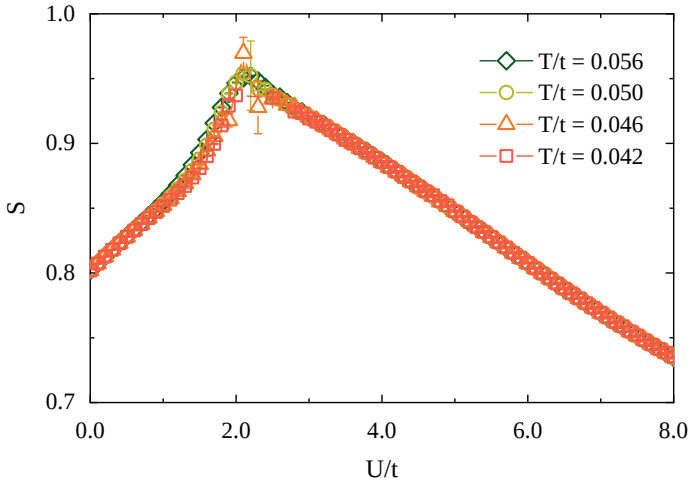

Figure 4.5: Single-site entanglement as a function of U/t for the ionic square lattice for a 4×4 lattice and a temperature range $0.04 < T/t < 0.06$ – the peak at $U/t \simeq 2$, sharper at lower Ts, gives the location of the band-insulator-to-correlated-metal transition.

As this peak is not present for the other cases examined, we further explore its behavior at $T \simeq t/20$, shown in Fig. 4.5 for a 4×4 lattice. The peak turns sharper at this low-temperature limit, indicating that the band insulator-to-metal transition is signaled by the single-site von Neumann entropy rather than its derivative. Notably, in such a small lattice size, it has been noted that this is a first-order phase transition, i.e., associated with

energy level crossing [88]. The metallic state survives the increased interactions until the screened Coulomb repulsion leads to the gap reopening, when a second phase transition is observed, from a correlated metal to a Mott insulator.

Focusing on a quantitative description of the onset of the Mott regime, we investigate the behavior of $\partial S/\partial U$ in Fig. 4.4 for the different lattices. For the honeycomb [Fig. 4.4 (d)] and ionic square lattices [Fig. 4.4 (f)], we verify that $\partial S/\partial U$ present minima at $U_{\mathrm{min,S}}(T)$ that slowly move towards smaller values of U/t as the temperature decreases. On the other hand, for the kagome lattice [Fig. 4.4 (e)], all minima are located at similar values of U/t for all T/t. To obtain an estimate for the critical value of the interaction strength U_c at which the Mott transition takes place, we extrapolate the minima positions to $T \to 0$, assuming a linear dependence – see insets in Fig. 4.4. Notice that the minima in $\partial S/\partial U$ are better defined for the lower temperatures examined and flatten as the temperature increases, disappearing for $T/t \gtrsim 2$. Remarkably, the critical values obtained from the $T \to 0$ extrapolation are in agreement to those previously found for the Mott transition for all three lattices [106, 5, 137, 76, 143, 89] as, confirming that the average single-site entanglement is a good indicator of quantum phase transitions even at finite temperature for $T/t \lesssim 1$.

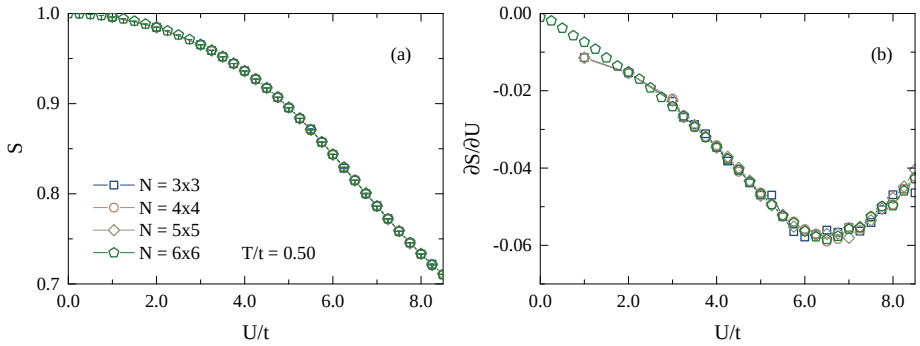

Figure 4.6: (a) Average single-site entanglement and (b) its derivative with respect to U/t as functions of U/t for different system sizes for the kagome lattice at $T/t = 0.5$.

Since these results are extracted at fixed system sizes, we now probe the potential influence of finite-size effects. Indeed, focusing on the kagome lattice, Fig. 4.6 shows that

the single-site entanglement and its derivative at $T/t = 0.5$ exhibit quantitatively minor finite-size effects for the analyzed range of number of sites, thus showing the robustness of the computed values of U_c to trigger the MI regime.

4.3.3 Susceptibility and entanglement

In this section, we analyze the relation between the single-site entanglement S and the ferromagnetic spin susceptibility $\chi(q = 0)$, obtained through the relation [42]

$$\chi(q=0) = -\beta \, \frac{1}{N} \sum_{\mathbf{i,j}} \langle (\hat{n}_{\mathbf{i}\uparrow} - \hat{n}_{\mathbf{i}\downarrow})(\hat{n}_{\mathbf{j}\uparrow} - \hat{n}_{\mathbf{j}\downarrow}) \rangle \ . \tag{4.4}$$

Focusing on half-filling, we report the χ vs. S relation in Fig. 4.7 for the honeycomb, kagome and ionic square lattices, at $T/t = 0.50$ and $T/t = 1.00$. The on-site interaction parametrizes the plot, and increases from right to left (see colorbars). While the single-site entanglement decreases as U/t increases (which was expected due to the behavior observed in Figs. 4.2 and 4.4), the susceptibility increases with U/t. These might be connected with the enhancement of local moment formation and short-range spin-spin correlation functions which are a consequence of the decrease of empty and double occupancies ($\omega_{i,0}$ and $\omega_{i,\uparrow\downarrow}$, respectively) [42, 145].

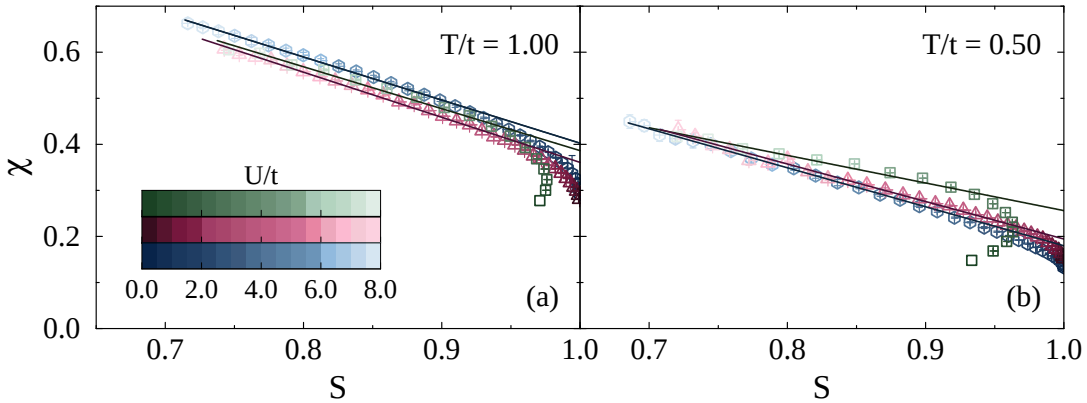

Figure 4.7: Ferromagnetic susceptibility as a function of single-site entanglement for different temperatures. The blue hexagons represent the honeycomb lattice, the pink triangles represent the kagome lattice and the green squares represent the square lattice. The lines are linear fits within a range of large U values, see text.

An interesting feature in Fig. 4.7 is the linear dependence between the susceptibility and S, similar to that observed in one-dimensional superfluid Hubbard chains [37]. The linear behavior is well established for higher values of χ, with the maximal value of $\chi_{\max}$ being equivalent to $U_{\max}/t = 8.0$ (lightest points in Fig. 4.7), and starts from a certain $\chi_{\min}$, with corresponding $U_{\min}/t$. To understand the relation of this linear behavior with U/t, we performed linear fits where we set the maximal value to be $\chi_{\max}$ and varied $\chi_{\min}$ from lowest to highest, thus obtaining linear fits for the interval $[U_{\min}/t, U_{\max}/t]$, with varying $U_{\min}/t$. From these fits, we obtained the reduced χ^2, $\chi^2_{\text{red}} = \chi^2/\text{degrees of freedom}$, which we plotted against $U_{\min}/t$ in Fig. 4.8. For the $T/t = 0.50$ of the honeycomb lattice the reduced χ^2 decreases with U/t for $U/t < 4$, developing a plateau for $U/t \geq 4$. This change of behavior happens near the critical value for the honeycomb lattice, which may suggest a connection between the linear behavior of χ when parametrized by U/t and the transition to the Mott phase. For $T/t = 1.00$, however, the plateau only develops for $U \geq 6$.

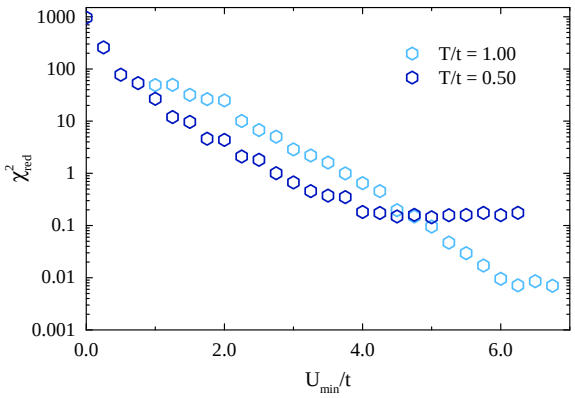

Figure 4.8: Reduced χ^2 for the linear fits of the susceptibility featured in Fig. 4.7. Each point is obtained by performing the linear fit within the (U, U_{max}) range.

4.4 Conclusions

In this Chapter, we study the behavior of the single-site entanglement entropy in two-dimensional systems at finite temperatures. Our goal was to explore the relation between

the single-site entanglement entropy and the critical interaction strengths for the onset of a Mott Insulator in the Hubbard model on the honeycomb and kagome lattices. For the ionic Hubbard model on the square lattice, we found that S signals both the Mott and the band insulator to metal transition.

When analyzing the dependency of the single-site entanglement with the electronic density, we see a change in the behavior of S, going from a one- to a two-peaked structure with increasing U/t at half-filling. This change of behavior can be observed at temperatures $T/t = 1.00$, and is caused by fluctuations produced by the quantum phase points at $T = 0$.

The dependency of the single-site entanglement with the onsite interaction signals a metal-to-band-insulator transition for the ionic Hubbard model on the square lattice, providing a critical value U_c in accordance with previous results [143, 89]. The derivative $\partial S/\partial U$ presents minima for all systems analyzed at temperatures $T/t \lesssim 1.00$, which, when extrapolated to the $T \to 0$ limit, allow us to find values of U_c/t that agree with previous works. Combined with the previous findings, these results show that the single-site entanglement can be employed to estimate quantum phase transitions at finite temperatures.

We also examined the connection between entanglement and magnetic susceptibility. We found that the parametrized magnetic susceptibility has a linear dependence with the single-site entanglement for all systems, similar to one-dimensional Hubbard chains. While a linear relation between the magnetic susceptibility and the entanglement is not sufficient to quantitatively determine the latter, from an experimental point of view, it is still possible to estimate how entangled is a certain system based on the linearity between these quantities.

The contents of this Chapter appear in Ref. [77], and have been submitted for publication.

Chapter 5

Interacting fermions in a symmetry-protected nodal-line semimetal

5.1 Introduction

In recent papers authored by M. Malard and collaborators [146, 147, 3], the following idea was advanced: Vacancy engineering can produce a 2D monoatomic, and yet symmetry-enforced, nodal line semimetals (NLSMs) by turning a symmorphic crystal into a non-symmorphic one. In Fig. 5.1 (a) we have the lattice structure of borophene with 10 atoms in its unit cell. Due to vacancy engineering, this material displays symmetry-enforced and accidental nodal lines, shown in Fig. 5.1 (c) and (d), respectively. In symmorphic crystals the accidental nodal lines should disappear when subject to spin-orbit coupling (SOC), however, the opposite happens for this nonsymmorphic one. When Rashba SOC with strength $\lambda = 0.1eV$ is applied to B_{10}, the accidental nodal lines become even stronger than when not subject to any perturbations, as can be seen in Fig. 5.1 (d).

In Refs. [146, 147, 3], one of the structures investigated therein is obtained by depleting 1/5 of the sites of a honeycomb lattice, as depicted in Fig. 5.2 (a), wielding a nonsymmorphic glide-plane symmetry, see Fig. 5.2 (b). Glide-plane, inversion, and time-reversal symmetries enforce nodal lines in the BZ of the depleted structure [3]. For short, let us call the so-obtained 2D vacancy-engineered symmetry-enforced NLSM a *nonsym-*

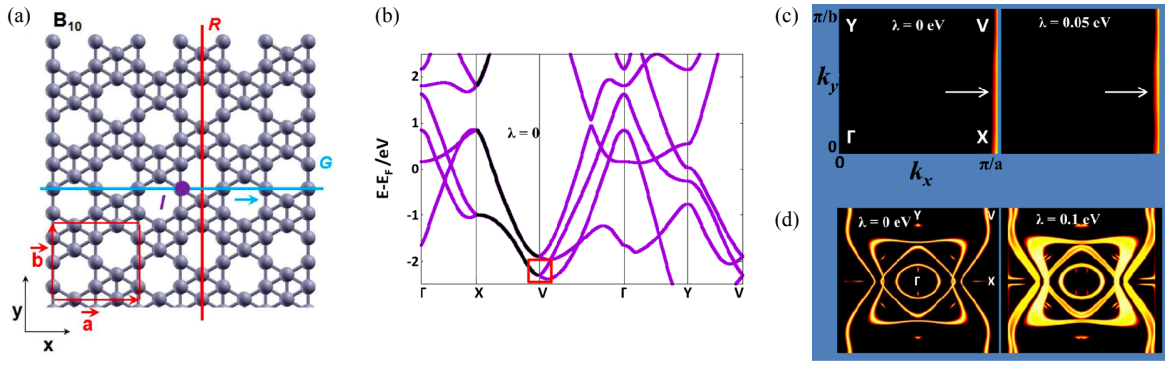

Figure 5.1: (a) Lattice structure of borophene B_{10}. Its unit cell is defined by primitive vectors $\vec{a}$ and $\vec{b}$, and the red and blue lines show the reflection and glide planes, respectively. This geometry is obtained by periodically removing sites from the pristine borophene. (b) Band structure of B_{10} without Rashba spin-coupling. The symmetry-enforced nodal lines along the X-V direction are highlighted in black. (c) On the left (right) is the contour plot of the symmetry-enforced nodal lines shown in (b) without (with) Rashba spin-orbit coupling. (d) On the left (right) is the contour plot of the accidental nodal lines within a 2.0 eV energy window about the Fermi energy without (with) Rashba spin-orbit coupling. Adapted from Ref. [3].

morphic holey graphene. We note that the proposed mechanism does not rely on chemical composition. Hence, Fig. 5.2 (a) could, in principle, represent any material that realizes a honeycomb lattice in its vacancy-free form, such as silicene, germanene, and borophene, besides graphene. For graphene, similar lattice-engineering methods have been reported using defects [148] and by manipulating single atoms on a substrate [149].

In this Chapter, we employ a mean-field approach and an unbiased determinant quantum Monte Carlo (DQMC) simulation to investigate *e*-*e* interactions in the nonsymmorphic holey graphene of Fig. 5.2 (a). We are particularly interested in the possibility that interactions drive symmetry-breaking instabilities, gapping out the nodal lines. The codimension of the nodal line plays a crucial role in this analysis. In three dimensions, nodal lines (codimension $p = 2$) lead to a vanishing density of states [150], which implies that short-range interactions are perturbatively irrelevant in the renormalization-group sense. On the other hand, a nodal line in two dimensions (codimension $p = 1$) generates a finite density of states. In the particular case of the model for nonsymmorphic holey graphene

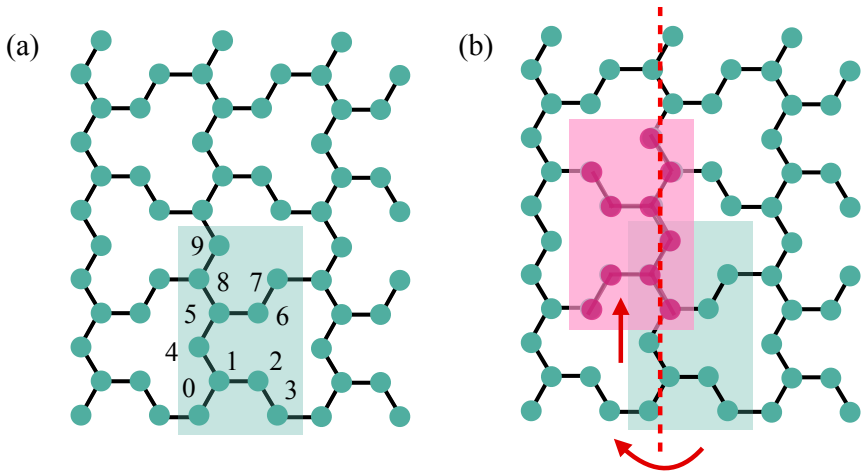

Figure 5.2: (a) The honeycomb lattice with depletions. The highlighted rectangle is the unit cell and the basis sites are numbered. (b) The glide plane is depicted by the red dashed line.

with uniform hopping parameters, we find that the spectrum exhibits a crossing between a symmetry-enforced and an accidental nodal line, which gives rise to a van Hove singularity at the Fermi level. We will show that this effect leads to an instability towards an antiferromagnetically ordered state for arbitrarily weak e-e interactions. By contrast, for the Dirac semimetal in the half-filled pristine honeycomb lattice, the transition to an antiferromagnetic (AFM) Mott insulator requires a finite interaction strength $U_c = 3.8$ (in units of the hopping amplitude) [106, 151, 5].

5.2 The repulsive Hubbard model

We investigate the properties of interacting fermions on a nodal-line semimetal system created by engineering the lattice presented in Fig. 5.2 (a). In order to facilitate the following discussions, we assume single s-orbitals with a Hubbard on-site interaction, while keeping the hopping integrals only between nearest neighbor (NN) sites, as discussed in Chapter 2. Our Hamiltonian in the Hubbard Hamiltonian given by (2.10). Here, we define the notation $\mathbf{i} = \boldsymbol{\alpha} + \mathbf{r}$, with $\boldsymbol{\alpha}$ denoting the position of the α-th orbital ($\alpha = 0, \ldots, 9$),

and $\mathbf{r}$ the position of the unit cell. To preserve the glide symmetry and, consequently, the nodal lines, one must impose that the following pairs of orbitals are equivalent (see Fig. 5.2): ($s0$,$s5$), ($s1$,$s8$), ($s2$,$s7$), ($s3$,$s6$), and ($s4$,$s9$). Similarly, the equivalent hopping integrals $t_{\alpha\alpha'}$ are: $t_{01} = t_{58}$, $t_{12} = t_{78}$, $t_{23} = t_{67}$, $t_{14} = t_{89}$, $t_{45} = t_{90}$, and $t_{56} = t_{03}$. If we impose spatial inversion in addition to glide symmetry, we are left with three sets of equivalent orbitals: ($s0$,$s1$,$s5$,$s8$), ($s2$,$s3$,$s6$,$s7$), and ($s4$,$s9$).

We investigate the properties of this Hamiltonian using a mean-field approach and unbiased determinant quantum Monte Carlo (DQMC) simulations [41, 42, 81]. We also use linear spin-wave theory (LSWT) to probe the ground state magnetic properties of the strong-coupling limit, $U \to \infty$, as the system can be mapped onto the Heisenberg model at half-filling.

On the other hand, the mean-field approach performs an approximation in the interaction term by breaking the symmetry of the Hamiltonian. For the Hubbard model, the *SU(2)* symmetry can be broken along the z-component of the spin, so the interacting term may be approximated as

$$U n_{\mathbf{i},\uparrow} n_{\mathbf{i},\downarrow} \approx U \sum_{\sigma} \left[\frac{\langle n_{\mathbf{i}} \rangle}{2} - \sigma \langle m_{\mathbf{i}} \rangle \right] c^{\dagger}_{\mathbf{i}\sigma} c_{\mathbf{i}\sigma} - U \left[\frac{\langle n_{\mathbf{i}} \rangle^2}{4} - \langle m_{\mathbf{i}} \rangle^2 \right] \tag{5.1}$$

with $\langle n_{\mathbf{i}} \rangle = \langle c^{\dagger}_{\mathbf{i}\uparrow} c_{\mathbf{i}\uparrow} + c^{\dagger}_{\mathbf{i}\downarrow} c_{\mathbf{i}\downarrow} \rangle$ being the average number of electrons on site $\mathbf{i}$, while $\langle m_{\mathbf{i}} \rangle = \langle S^z_{\mathbf{i}} \rangle = \frac{1}{2} \langle c^{\dagger}_{\mathbf{i}\uparrow} c_{\mathbf{i}\uparrow} - c^{\dagger}_{\mathbf{i}\downarrow} c_{\mathbf{i}\downarrow} \rangle$ its magnetization. Since the lattice is bipartite, we assume an AFM state in which the sign of $\langle m_{\mathbf{i}} \rangle$ alternates between even and odd sublattices (i.e., between even and odd values of α), in a way that the spatial dependence of $\langle n_{\mathbf{i}} \rangle$ and $\langle m_{\mathbf{i}} \rangle$ preserves translational symmetry. Further details of our mean-field approach are discussed later.

5.3 Results

5.3.1 Vacancy-engineered nodal-line semimetal: the non-interacting limit

As discussed earlier, a NLSM may be created by engineering a lattice with periodic depletions that give rise to glide, point inversion, and time reversal symmetries [3]. For example, it is achieved by engineering a honeycomb lattice depleted with 1/5, as shown in Fig. 5.2 (a), with the shaded area defining the unit cell, while the numbers are the site labels. As shown in Fig. 5.2 (b), this structure has a glide symmetry, with the vertical dashed (red) line representing the glide plane. In this subsection, we discuss the non-interacting properties of this NLSM, i.e., we set $U = 0$, leaving the interaction effects to the next subsections.

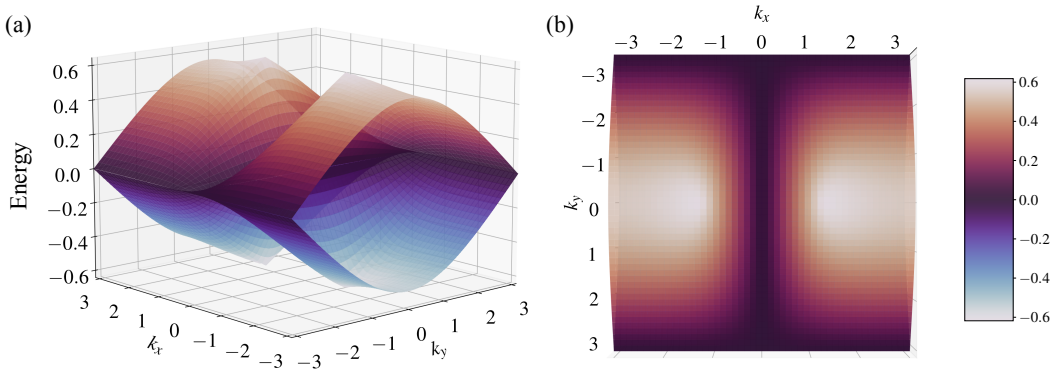

Figure 5.3: (a) Side and (b) top view of the dispersion relation focusing on the two bands closer to the Fermi level ($E = 0$) at half filling. The bands cross at the Fermi level (darker color), forming the nodal lines along $k_x = 0$ and $k_y = \pi$. The energy scale is expressed in units of $t = 1$.

The Fourier transform of the non-interacting Hamiltonian leads to a block-diagonal 10×10 matrix that can be diagonalized numerically. Due to the particle-hole symmetry, the nodal lines appear at zero energy, coinciding with the Fermi level at half filling. Figure 5.3 (a) displays the two bands that cross the Fermi level and touch along the nodal lines presented in Fig. 5.3 (b). Interestingly, there are two nodal lines: one at $k_y = \pi$ and

another at $k_x = 0$. As discussed in Refs. [146, 147, 3], the former is symmetry-enforced, while the latter is accidental.

Although the results presented in Fig. 5.3 were obtained by fixing $t_{\mathbf{i},\mathbf{j}} = t$, we can test the stability of the nodal lines by considering inhomogeneous hopping while preserving the glide symmetry. For example, when we set $t_{23} = t_{67} \neq t$ [See Fig. 5.4 (a)-(b)], the (horizontal) nodal line at $k_y = \pi$ is maintained, while the (vertical) nodal line at $k_x = 0$ is destroyed. We illustrate this feature by fixing $k_y = 0$ and varying k_x, or by fixing $k_x = \pi$ and varying k_y, as shown in Figs. 5.4 (a) and (b), respectively. In fact, any difference among the pairs of hopping integrals (t_{01},t_{58}), (t_{12},t_{78}), (t_{23},t_{67}) and (t_{56},t_{03}) is enough to gap out the accidental nodal line at $k_x = 0$ while the symmetry-enforced one at $k_y = \pi$ is unremovable.

Interestingly, unlike the previous case, changing the values of (t_{14},t_{89}) and (t_{45},t_{90}) does not destroy the accidental nodal line at $k_x = 0$. This behavior is shown in Fig. 5.4 (c)-(d) for the case of changing (t_{14},t_{89}), where one may notice the presence of both nodal lines for different values of (t_{14},t_{89}), with the crossing bands collapsing into a twofold degenerate flat band when $t_{14} = t_{89} \to 0$. To understand the formation of these flat bands, we note that for $t_{14} = t_{89} = 0$ the system reduces to a set of decoupled chains, as illustrated in Fig. 5.4 (e). The fact that the chains are bipartite and have an odd number of sites per unit cell implies compact localized states, thus flat bands [152, 153]. Therefore, we expect that in the half-filled ground state, the limiting case $t_{14} = t_{89} \to 0$ would favor magnetism for any $U/t > 0$, as provided by Lieb's theorem [153].

Examining the local density of states (LDOS) in the noninteracting case is also important. Taking the time Fourier transform and performing an analytical continuation of the single-particle Green's function (see, e.g. Refs. [154, 155] for details), we obtain the spectral functions

$$A^{\alpha}_{\sigma}(\mathbf{k}, \omega) = -\frac{1}{\pi} \operatorname{Im} G^{\alpha}_{\sigma}(\mathbf{k}, \omega + i0^{+}), \tag{5.2}$$

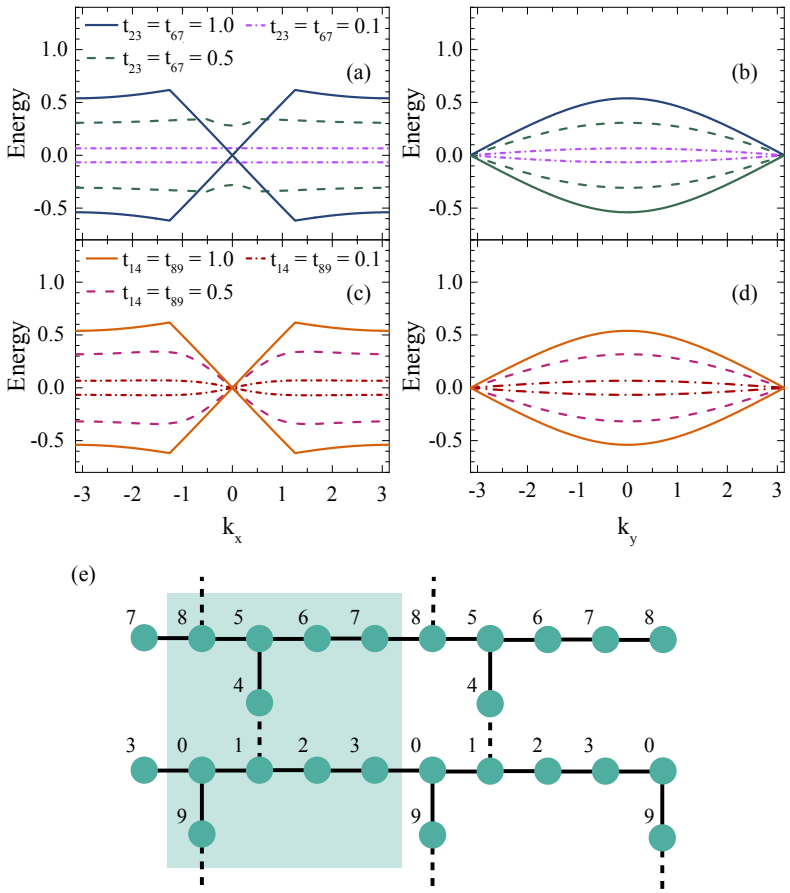

Figure 5.4: Energy dispersion for fixed $k_y = 0$ [panels (a) and (c)] and $k_x = \pi$ [panels (b) and (d)]. The nodal-line at $k_x = 0$ is gapped out whenever $t_{23} = t_{67} \neq 1.0$, but remains unaffected when $t_{14} = t_{89} \neq 1.0$, where $t = 1.0$ is the value of the hopping parameter for the other glide-related pairs. Expectedly, the nodal-line at $k_y = \pi$ is not destroyed for when changing the value of any of the glide-related pairs. (e) Different arrangement of the depleted honeycomb lattice, which shows the decoupling into two separate lattices when $t_{14} = t_{89} \to 0$ (dashed lines).

with $\alpha = 0, \ldots, 9$ denoting the different orbitals. Given this, the LDOS is defined as

$$N^{\alpha}(\omega) = \sum_{\mathbf{k},\sigma} A^{\alpha}_{\sigma}(\mathbf{k}, \omega). \tag{5.3}$$

Figure 5.5 displays the LDOS for all orbitals, divided into three categories: [i] panels (a)-(b), for $(s0, s5)$ and $(s1, s8)$; [ii] panels (c)-(d), for $(s2, s7)$ and $(s3, s6)$; [iii] panels (e)-(f), for $(s4, s9)$. Notice that this division is directly related to the coordination number z of the orbitals. The panels on the left [i.e., (a), (c), and (e)] display data for homogeneous hopping, $t_{\mathbf{i},\mathbf{j}} = 1$, while those in the right [i.e., (b), (d), and (f)] have $t_{14} = t_{89} = 0.5$.

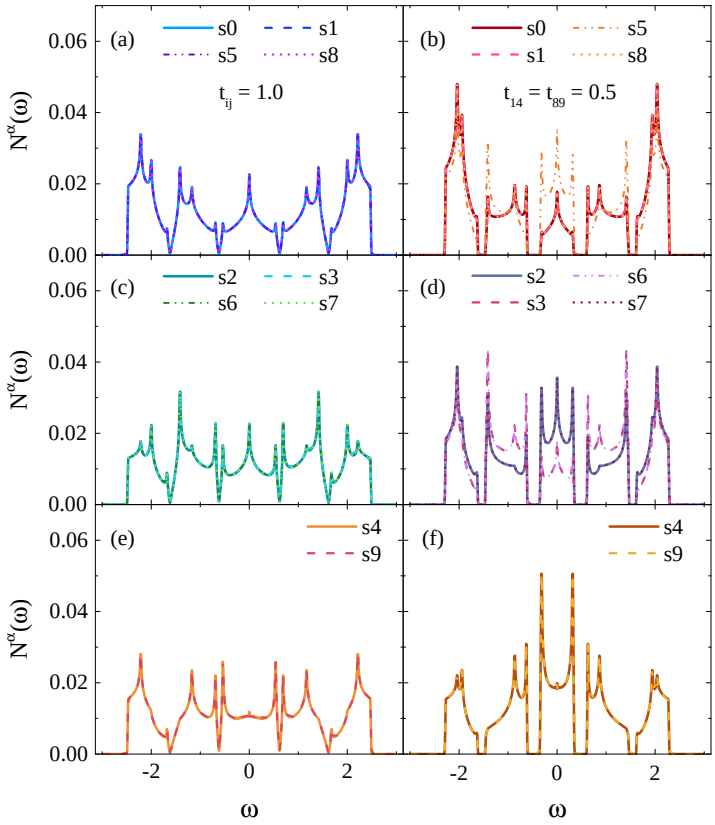

Figure 5.5: Local density of states for orbitals sites $s0$, $s5$, $s1$ and $s8$ (a)-(b), $s2$, $s7$, $s3$ and $s6$ (c)-(d), and $s4$ and $s9$ (e)-(f). The panels on the left display the LDOS for homogeneous hoppings ($t_{ij} = 1.0$) and the panels on the right display data for $t_{14} = t_{89} = 0.5$. The van Hove singularities present in the homogeneous case [panels (a) and (c)] persist when hopping anisotropy in $t_{14} = t_{89}$ is introduced [panels (b) and (d)]. For $s4$ and $s9$, the van Hove singularity at $\omega = 0$ is weak in both the isotropic and anisotropic scenarios [panels (e) and (f).]

Figure 5.5 clearly shows a well-formed van Hove singularity at $\omega = 0$ in the LDOS of orbitals ($s0$,$s5$), ($s1$,$s8$), ($s2$,$s7$) and ($s3$,$s6$), even in the presence of anisotropy introduced in $t_{14} = t_{89}$. Meanwhile, the peak at $\omega = 0$ for $(s4, s9)$ is rather weak already for the isotropic case.

We can show that the van Hove singularity at the Fermi level is due to the crossing of the accidental and symmetry-enforced nodal lines at the momentum $\mathbf{k} = (0, \pi)$. Expanding the dispersion of the two low-energy bands in the vicinity of the crossing point, we obtain the form $\varepsilon_{\pm}(\mathbf{p}) \approx \pm c|p_x p_y|$, where $\mathbf{p} = (k_x, k_y - \pi)$ with $|\mathbf{p}| \ll 1$ and c is a

constant of the order of the bandwidth. We then have

$$\sum_{\alpha} N^{\alpha}(\omega) \sim \int d^2p\, \delta(\omega \mp c|p_x p_y|) \sim \ln\left(\frac{c\Lambda^2}{|\omega|}\right), \tag{5.4}$$

where Λ is an ultraviolet momentum cutoff of order unity. Thus, the LDOS diverges logarithmically for $\omega \to 0$. As a consequence, the Stoner criterion strongly suggests that the system is unstable against interactions in this case. On the other hand, if glide-symmetry-preserving perturbations gap out the accidental nodal line, we expect the low-energy density of states to be finite and inversely proportional to the velocity of the linear dispersion around the remaining symmetry-enforced nodal line. To verify this statement, we consider a glide-symmetry-preserving anisotropy that acts on any pair of glide-related hopping parameters other than $t_{14} = t_{89}$ (by that excluding the special anisotropic case for which, as seen before, the accidental nodal line and the van Hove singularity at the Fermi level remain). In Fig. 5.6, we show the LDOS for two cases in which we vary a pair of hopping integrals, either (t_{23},t_{67}) or (t_{01},t_{58}). In both cases, we can see a finite LDOS at the Fermi level, thus confirming that a glide-symmetry-preserving anisotropy that destroys the accidental nodal line also removes the van Hove singularity at the Fermi level.

5.3.2 Mean-field approach

We now discuss the mean-field solution of the interacting ($U/t \neq 0$) Hamiltonian in Eq. (2.10). Since the unit cell has multiple orbitals, we need to define average values for the local density and local magnetization, i.e. $\langle n_{\mathbf{r}\alpha}\rangle = \langle c^{\dagger}_{\mathbf{r}\alpha\uparrow} c_{\mathbf{r}\alpha\uparrow} + c^{\dagger}_{\mathbf{r}\alpha\downarrow} c_{\mathbf{r}\alpha\downarrow}\rangle$ and $\langle m_{\mathbf{r}\alpha}\rangle = \frac{1}{2}\langle c^{\dagger}_{\mathbf{r}\alpha\uparrow} c_{\mathbf{r}\alpha\uparrow} - c^{\dagger}_{\mathbf{r}\alpha\downarrow} c_{\mathbf{r}\alpha\downarrow}\rangle$, respectively. In addition, as the lattice is bipartite, at half-filling we expect the emergence of staggered magnetism with no charge order. Thus, in our mean-field approach we set $\langle n_{\mathbf{r}\alpha}\rangle = n = 1$, while $\langle m_{\mathbf{r}\alpha}\rangle = m_{\alpha} > 0$ for α even, and

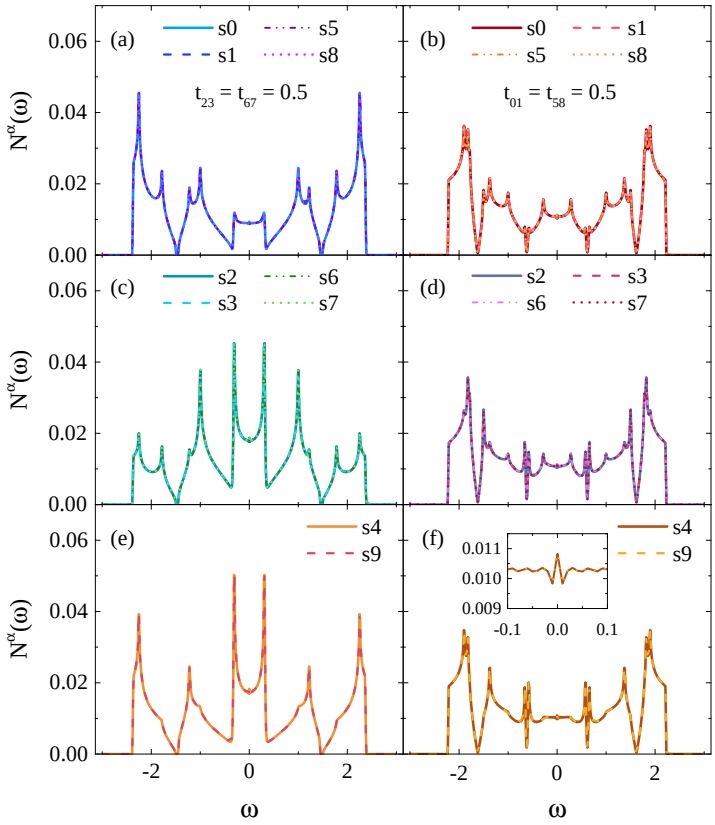

Figure 5.6: Local density of states for orbitals $s0$, $s5$, $s1$ and $s8$ (a)-(b), $s2$, $s7$, $s3$ and $s6$ (c)-(d), and $s4$ and $s9$ (e)-(f). The panels on the left display the LDOS with $t_{23} = t_{67} = 0.5$ and the panels on the right $t_{01} = t_{58} = 0.5$. The LDOS becomes finite in panels (a)-(d) when hopping anisotropies $t_{23} = t_{67}$ and $t_{01} = t_{58}$ are introduced, resembling the behavior in Fig. 5.5 (e) and (f). The inset in panel (f) shows the LDOS for sites $s4$ and $s9$ near $\omega = 0$.

$\langle m_{\mathbf{r}\alpha} \rangle = m_\alpha < 0$ for α odd. As a result, the mean-field Hamiltonian reads

$$\begin{aligned} \mathcal{H}_{\mathrm{MF}} = & -t \sum_{\langle \mathbf{r}\alpha, \mathbf{r}'\alpha' \rangle, \sigma} \left(c^\dagger_{\mathbf{r}\alpha\sigma} c_{\mathbf{r}'\alpha'\sigma} + \mathrm{H.c.} \right) - \mu \sum_{\mathbf{r}\alpha,\sigma} n_{\mathbf{r}\alpha\sigma} \\ & - U \sum_{\mathbf{r}\alpha,\sigma} \sigma \, m_\alpha \, c^\dagger_{\mathbf{r}\alpha\,\sigma} c_{\mathbf{r}\alpha\,\sigma} + N\,U \sum_\alpha \left(m_\alpha^2 + \frac{1}{4} \right), \end{aligned} \tag{5.5}$$

with $\langle \mathbf{r}\alpha, \mathbf{r}'\alpha' \rangle$ denoting NN sites, and N being the number of unit cells.

The mean-field Hamiltonian can be diagonalized in Fourier space using a ten-component spinor, leading to the bands $E^n_{\mathbf{k},\sigma}$, with $n = 0, \ldots, 9$. The corresponding Helmholtz free

energy is

$$F = -\frac{1}{\beta}\sum_{n,\mathbf{k},\sigma} \ln\left(1 + e^{-\beta E^{n}_{\mathbf{k},\sigma}}\right) + \text{const.}, \tag{5.6}$$

where $\beta = 1/k_B T$. We are then able to determine the effective fields by self-consistently minimizing the Helmholtz free energy, $\left\langle \frac{\partial F}{\partial m_\alpha} \right\rangle = 0$. The resulting nonlinear coupled equations are solved numerically with standard library routine packages, using the Hellmann-Feynman theorem. Note that the term proportional to m_α in Eq. (5.5) breaks the glide symmetry in the mean-field Hamiltonian by attributing an opposite magnetization to glide-related sites. However, we assume that the magnetic phase preserves the product of glide symmetry and spin flip, which implies that pairs of sites connected by the glide symmetry must have opposite magnetization; for instance, $m_0 = -m_5$, $m_1 = -m_8$, and so on. This condition guarantees that the ground state has zero net magnetization and reduces the number of effective fields by half.

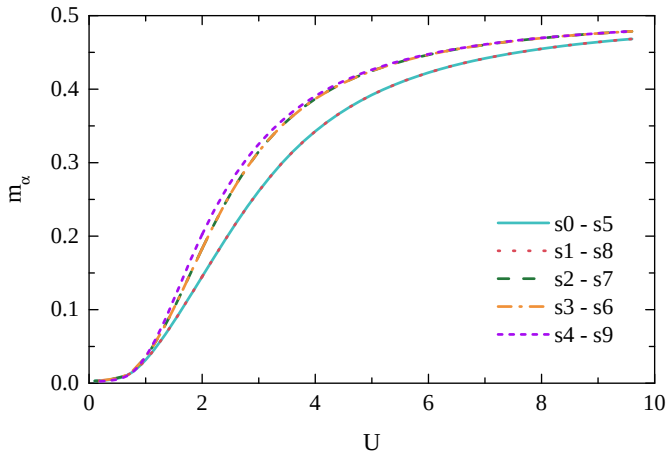

Figure 5.7: Magnetic order parameter as a function of the Hubbard interaction U/t at half-filling.

Figure 5.7 displays the ground state results for the mean-field magnetic order parameters m_α as a function of the interaction strength U/t, for homogeneous hopping integrals. Three remarks are in order. First, as expected, there are three distinct responses for the magnetic order parameters, due to the three kinds of LDOS discussed in the previous subsection. Note that the spontaneous magnetization is weaker on sites with coordina-

tion number $z = 3$, corresponding to orbitals $(s0, s1, s5, s8)$, than on sites with only two nearest neighbors. Second, our mean-field approach shows magnetism for any $U/t > 0$, putting the nonsymmorphic holey graphene in stark contrast to its pristine counterpart whose critical e-e interaction is known to be $U_c/t = 3.8$ [151, 106, 5]. The found magnetic order of nonsymmorphic holey graphene at arbitrarily weak e-e interaction is similar to the behavior of the Hubbard model on a square lattice, where the van Hove singularity is due to the nesting of the Fermi surface at half-filling, rather than the crossing of nodal lines as in our case.

As a third remark, we verified that the mean-field results are independent of the choice of spin direction used to break the *SU(2)* symmetry. In particular, we obtained identical results when $\langle S^x_{\mathbf{i}} \rangle \neq 0$. Furthermore, we observed that any net staggered magnetization breaks the glide symmetry and is sufficient to open a gap at half-filling, while a ferromagnetic solution preserves the glide symmetry and, hence, the symmetry-enforced nodal line. However, it is important to emphasize that the ferromagnetic state is not the ground state of the system at this filling. We conclude that, although the lattice with staggered magnetization has a kind of "modified glide symmetry", defined by the crystalline glide plane times a spin flip, this new symmetry does not ensure the survival of the nodal line enforced by the glide symmetry in the non-interacting model.

5.3.3 Linear spin wave theory

Since the mean-field solution discussed in the previous subsection is expected to be valid in the limit $U \to 0$, it is worthwhile to consider the strong-coupling limit, $U \to \infty$. At half-filling, the system can be mapped onto the Heisenberg model, whose ground-state magnetic properties can be analyzed using linear spin-wave theory (LSWT).

The Heisenberg model on the depleted honeycomb lattice is given by

$$\mathcal{H}_s = \sum_{\langle \mathbf{i},\mathbf{j} \rangle} J_{\mathbf{i},\mathbf{j}} \mathbf{S}_{\mathbf{i}} \cdot \mathbf{S}_{\mathbf{j}}, \tag{5.7}$$

where $J_{\mathbf{i},\mathbf{j}} = 4t^2_{\mathbf{i},\mathbf{j}}/U$ is the exchange coupling and $\mathbf{S_i}$ is the spin-S operator at site $\mathbf{i}$. We shall keep S as a free parameter and set $S = 1/2$ at the end. Assuming uniform hopping integrals, we set $J_{\mathbf{i},\mathbf{j}} = J = 4t^2/U$ for all nearest-neighbor bonds.

The classical spin configuration corresponds to a Néel state on this bipartite lattice. To describe the spin excitations, we use the Holstein-Primakoff transformation with $S^z_{\mathbf{i}} = (-1)^\alpha(S - a^\dagger_{\mathbf{i}} a_{\mathbf{i}})$, where $\alpha = 0, 1, \ldots, 9$ is the orbital index of site $\mathbf{i}$ and $a_{\mathbf{i}}$ is a boson annihilation operator. Within LSWT, the quadratic boson Hamiltonian to order S has the form

$$\mathcal{H}_s \approx E_{\rm cl} + \frac{JS}{2}\sum_{\mathbf{i}} z_{\mathbf{i}} a^\dagger_{\mathbf{i}} a_{\mathbf{i}} + JS\sum_{\langle \mathbf{i},\mathbf{j}\rangle}(a_{\mathbf{i}} a_{\mathbf{j}} + a^\dagger_{\mathbf{i}} a^\dagger_{\mathbf{j}}), \tag{5.8}$$

where $z_{\mathbf{i}} = z_\alpha$ is the coordination number of site $\mathbf{i}$ with orbital index α and $E_{\rm cl} = -12NJS^2$ is the energy of the classical Néel state for N unit cells.

Taking a Fourier transform, we define the vector $\mathbf{X}(\mathbf{k}) = (a_0(\mathbf{k}), \ldots, a_9(\mathbf{k}), a^\dagger_0(-\mathbf{k}), \ldots, a^\dagger_9(-\mathbf{k}))$ and rewrite the Hamiltonian in the form

$$\mathcal{H}_s \approx E_{\rm cl} - NJS{\rm Tr}(A) + \frac{JS}{2}\sum_{\mathbf{k}} \mathbf{X}^\dagger(\mathbf{k})\mathbf{H}(\mathbf{k})\mathbf{X}(\mathbf{k}), \tag{5.9}$$

where

$$\mathbf{H}(\mathbf{k}) = \begin{pmatrix} A & B(\mathbf{k}) \\ B^*(-\mathbf{k}) & A \end{pmatrix}. \tag{5.10}$$

Here A is a 10×10 diagonal matrix with nonzero elements given by $A_{\alpha\alpha} = z_\alpha$ and $B(\mathbf{k})$ stems from the Fourier transform of the nearest-neighbor-coupling terms in Eq. (5.8). We diagonalize the Hamiltonian in the standard way [156] using a Bogoliubov transformation $\mathbf{X}(\mathbf{k}) = \mathbf{Q}(\mathbf{k})\mathbf{Y}(\mathbf{k})$, where $\mathbf{Y}(\mathbf{k})$ is the new vector of bosonic operators and the matrix $\mathbf{Q}(\mathbf{k})$ obeys

$$\mathbf{Q}^\dagger(\mathbf{k})\mathbf{g}\mathbf{Q}(\mathbf{k}) = \mathbf{g}, \tag{5.11}$$

$$\mathbf{Q}^\dagger(\mathbf{k})\mathbf{H}(\mathbf{k})\mathbf{Q}(\mathbf{k}) = \mathbf{\Lambda}(\mathbf{k}), \tag{5.12}$$

where $\mathbf{g} = {\rm diag}(1, \ldots, 1, -1, \ldots, -1)$ and $\mathbf{\Lambda}(\mathbf{k}) = {\rm diag}(\omega_0(\mathbf{k}), \ldots, \omega_9(\mathbf{k}), \omega_0(-\mathbf{k}), \ldots, \omega_9(-\mathbf{k}))$. The functions $\omega_\lambda(\mathbf{k})$, with $\lambda = 0, \ldots, 9$, correspond to the dispersion relations of the

magnon bands. The quantum correction to the magnetization in each sublattice can be calculated from the matrix $\mathbf{Q}(\mathbf{k})$ as

$$\Delta S_\alpha = \frac{1}{2N}\sum_{\mathbf{k}}\sum_{\lambda=10}^{19}\left[|\mathbf{Q}_{\alpha,\lambda}(\mathbf{k})|^2 + |\mathbf{Q}_{\alpha+10,\lambda}(\mathbf{k})|^2\right] - \frac{1}{2}. \tag{5.13}$$

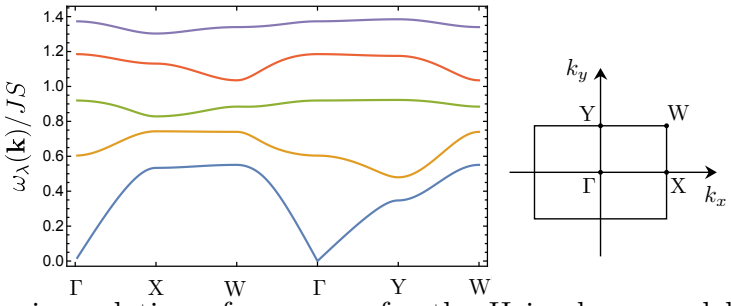

Figure 5.8: Dispersion relation of magnons for the Heisenberg model on the depleted honeycomb lattice.

In Fig. 5.8 we show the magnon dispersion along high-symmetry directions in the Brillouin zone. We obtain five twofold degenerate bands. The lowest band is gapless with linear dispersion around the Γ point, as expected from Goldstone modes associated with the spontaneous breaking of *SU(2)* symmetry. The absence of zero-energy flat bands in the magnon spectrum indicates that the antiferromagnetic state is stable. Indeed, by calculating the quantum corrections to the magnetization, we find that the order parameter remains finite and respects the symmetry that combines spatial inversion and a spin flip, as well as the composition of glide plane and spin flip. The order parameters $m_\alpha = S - \Delta S_\alpha$ for each sublattice are (setting $S = 1/2$)

$$\begin{aligned} m_0 &= m_1 = m_5 = m_8 = 0.124, \\ m_2 &= m_3 = m_6 = m_7 = 0.140, \\ m_4 &= m_9 = 0.199. \end{aligned} \tag{5.14}$$

The average antiferromagnetic order parameter is $m = \frac{1}{10}\sum_\alpha m_\alpha = 0.146$. Note that the order parameter is smaller on the sites with coordination number $z = 3$, in agreement with the mean-field result. Comparing with the result $m = 0.242$ from LSWT for the

pristine honeycomb lattice [157], we conclude that the creation of vacancies leads to weaker antiferromagnetic order in the strong-coupling limit.

The calculations presented in this subsection were performed by Rodrigo G. Pereira, who collaborated on Ref. [78].

5.3.4 Quantum Monte Carlo

After discussing the weak- and strong-coupling limits in the previous subsections, we now turn our attention to the Hubbard model at intermediate interaction strengths. This analysis is performed using unbiased DQMC simulations, with up to 10^4 Monte Carlo sweeps for thermalization and 10^5 for measurements. To this end, we start with the mean double occupancy,

$$D = \frac{1}{10N}\sum_{\mathbf{r},\alpha}\left\langle n_{\mathbf{r},\alpha\uparrow}n_{\mathbf{r},\alpha\downarrow}\right\rangle = \frac{1}{10}\sum_{\alpha} D_{\alpha}\ , \tag{5.15}$$

which is the average over all orbitals, with N being the number of unit cells. Figure 5.9 displays the behavior of D as a function of temperature for different values of U/t. The mean double occupancy is suppressed as U/t increases, with the appearance of a minimum for sufficiently large interaction strength values. As suppression of D is expected for interacting systems (since electrons avoid sitting in the same orbital), its minimum is directly related to the emergence of unusual (bad) metallic properties [158]. In addition, there are many suggestions that the sign change of $\partial D/\partial T$ is a key feature of the occurrence of anomalies in the Seebeck coefficient, which, in turn, leads to a reconstruction of the Fermi surface [159, 160]. Finally, for $\frac{\partial D}{\partial T} < 0$, the system can be adiabatically cooled by increasing the Hubbard interaction [161, 162, 107, 163, 164, 76], a condition relevant to the establishment of this geometry in cold-atom experiments. In summary, although beyond the scope of this thesis, all of these features (bad metallicity, anomalous Seebeck effect, and adiabatic cooling) are likely to occur in our interacting NLSM.

The double occupancy is directly related to the local-moment formation, since $D_{\alpha} = \frac{1}{2}\left[\langle n_{\alpha}\rangle - \langle m_{\alpha}^2\rangle\right]$, with $\langle m_{\alpha}^2\rangle = \langle (n_{\alpha\uparrow} - n_{\alpha\downarrow})^2\rangle$. Therefore, a decrease in D_{α} implies an

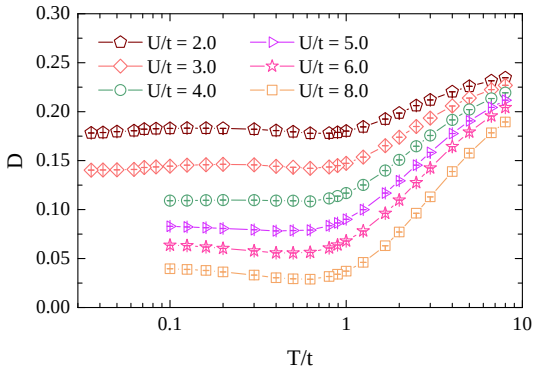

Figure 5.9: Double occupancy as function of T/t for different U/t considering a $N = 4 \times 4$ lattice (i.e. 160 sites).

increase in $\langle m_\alpha^2 \rangle$, once $\langle n_\alpha \rangle = 1$ at half filling. Given this, the behavior of the orbital local moments $\langle m_\alpha^2 \rangle$ as a function of temperature is similar to that presented in Fig. 5.9, for the mean double occupancy, but showing maxima instead of minima.

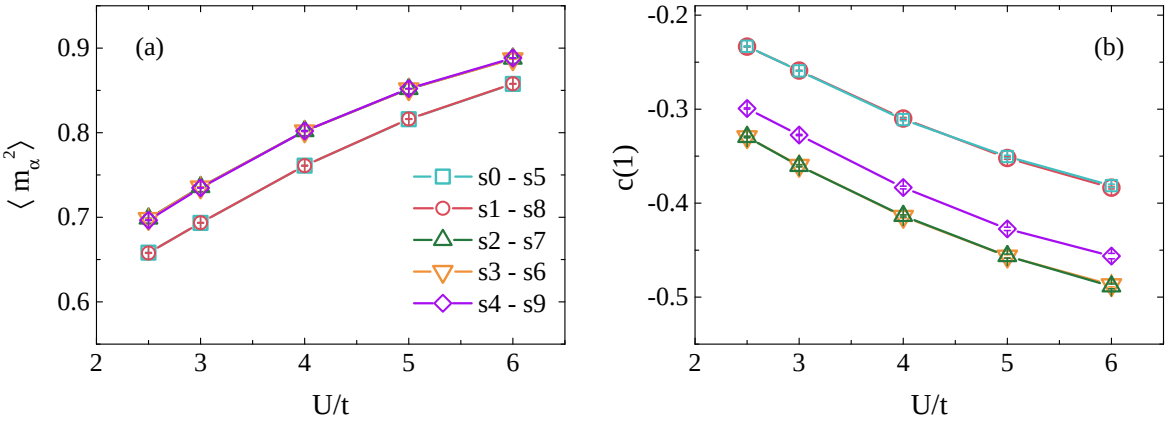

Figure 5.10: (a) Local moment, (b) spin-spin correlation function for nearest neighbors at $\beta = 24$ as a function of U/t for a depleted honeycomb lattice of size $N = 4 \times 4$ (160 sites).

To further investigate the magnetic properties, we examine the local moments as a function of U/t, at a low temperature ($\beta = 24$ is low enough to provide results close to the ground state ones), as displayed in Fig. 5.10 (a). We notice that $\langle m_\alpha^2 \rangle$ are well-formed and exhibit a non-uniform spatial response, with the local moment at orbitals $(s0, s5)$ and $(s1, s8)$ being smaller than at other ones. Longer distances spin-spin correlation functions,

given by

$$c(\mathbf{i}-\mathbf{j}) = \langle (n_{\mathbf{i}\uparrow} - n_{\mathbf{i}\downarrow})(n_{\mathbf{j}\uparrow} - n_{\mathbf{j}\downarrow}) \rangle = 4\langle S^z_{\mathbf{i}} S^z_{\mathbf{j}} \rangle \ ,$$

may also be analyzed, where we keep the notation $\mathbf{i} = \boldsymbol{\alpha} + \mathbf{r}$. Figure 5.10 (b) illustrates the behavior of $c(\mathbf{i}-\mathbf{j})$ as a function of U/t for each pair of orbitals corresponding to their NN sites, where $|\mathbf{i}-\mathbf{j}| = 1$. In fact, the quantity $c(1)$ represents the average value of $c(\mathbf{i}-\mathbf{j})$ over all NN sites. Notice that the non-uniform feature for the correlation functions remains, i.e. orbitals $(s0, s5)$ and $(s1, s8)$ display weaker spin-spin correlations, in agreement with the mean-field results in Fig. 5.7.

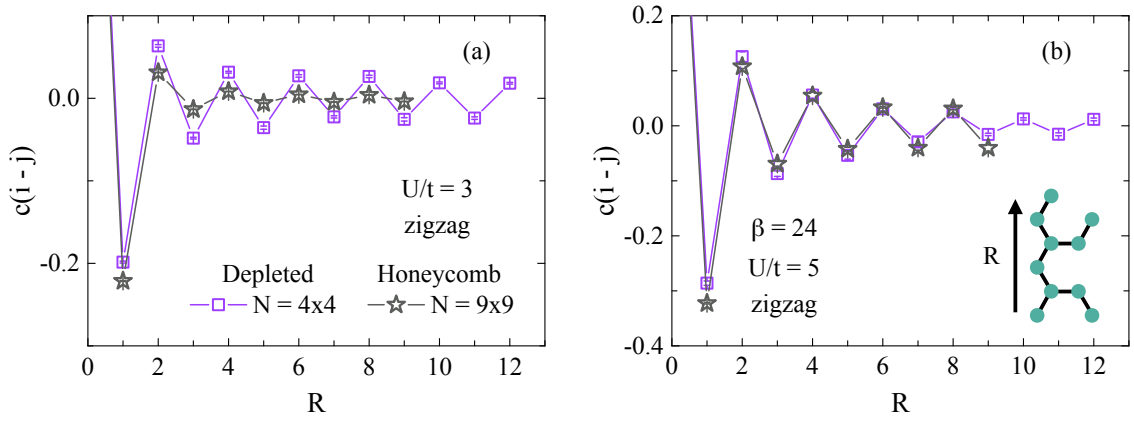

Figure 5.11: Spatial dependence of the spin-spin correlation functions for (a) $U/t = 3$ and (b) $U/t = 5$ at $\beta = 24$ for a depleted honeycomb lattice of size $N = 4 \times 4$ (squares) and a pristine lattice of size $N = 9 \times 9$ (stars). The origin is set on site $s0$ and $\mathbf{r}$ runs along the sites in the zigzag direction (see inset).

It is also worth comparing the magnetic properties of the depleted lattice with those of the pristine honeycomb one. To this end, we analyze the spin-spin correlation functions between a reference orbital $s0$ and the $\mathbf{i}$-th site/orbital along the zigzag direction. Specifically, following our definition of $\mathbf{i} \equiv (\mathbf{r}, \alpha)$, the sites we examine are $(\mathbf{r}, \alpha) = (\mathbf{0}, 0)$, $(\mathbf{0}, 1)$, $(\mathbf{0}, 4)$, $(\mathbf{0}, 5)$, $(\mathbf{0}, 8)$, $(\mathbf{0}, 9)$, $(\hat{y}, 0)$, $(\hat{y}, 1), \ldots$ (see, e.g., Fig. 5.2). Figure 5.11 shows the spin-spin correlation functions $c(R_{\mathbf{i}})$, with $R_{\mathbf{i}}$ being the Hamming distance, for (a) $U/t = 3$ and (b) $U/t = 5$, while fixed $\beta = 24$. In the latter case, both the

depleted and pristine honeycomb lattices display similar behavior. However, for $U/t = 3$, the $c^{\alpha,\gamma}(R_{\mathbf{i}})$ response of the depleted lattice is significantly stronger than that of the honeycomb lattice. We recall that the Hubbard model in the honeycomb lattice has an AFM critical point at $U_c/t = 3.8$, therefore the results of Fig. 5.11 (a) suggest that site depletion enhances magnetic correlations, at least for weak and intermediate interaction strengths. This phenomenon has indeed been observed in the honeycomb lattice with a single depletion, and, in our case, it suggests the emergence of magnetism below the critical U/t of the pristine lattice [165].

The emergence of magnetism in the Hubbard model on depleted bipartite lattices is, in many cases, related to Lieb's theorem, which ensures the occurrence of ferrimagnetism when the number of sites in one sublattice exceeds that of the other sublattice [153, 166]. However, in the case we are considering, both sublattices have an equal number of sites. As a result, Lieb's theorem only ensures that the total spin is zero, leaving the possibility of magnetic ordering as an open issue.

A thorough determination of long-range order is given by the AFM spin structure factor,

$$S_{AFM} = \frac{1}{10}\frac{1}{N}\sum_{\mathbf{i},\mathbf{j}} c(\mathbf{i}-\mathbf{j})(-1)^{|\mathbf{i}-\mathbf{j}|} = \frac{1}{10}\frac{1}{N}\sum_{\mathbf{i},\mathbf{j}} 4\langle S^z_{\mathbf{i}} S^z_{\mathbf{j}}\rangle(-1)^{|\mathbf{i}-\mathbf{j}|} \ , \tag{5.16}$$

which is proportional to the square of the order parameter in the thermodynamic limit. Figure 5.12 shows S_{AFM} as a function of the inverse of temperature, for fixed (a) $U/t = 2.5$, (b) $U/t = 3.0$ and (c) $U/t = 3.5$, and different system sizes N. In all cases, the following behavior is observed: at high temperatures (low β), S_{AFM} is independent of the lattice size, indicating that the system exhibits only short-range correlations. As the temperature decreases (higher β), the spin correlation length becomes comparable to the system size, leading S_{AFM} to develop a plateau, whose value depends on N. The lattice size dependence of such a plateau is an important hint of long-range order.

Once the structure factor no longer changes as the temperature is lowered, one can

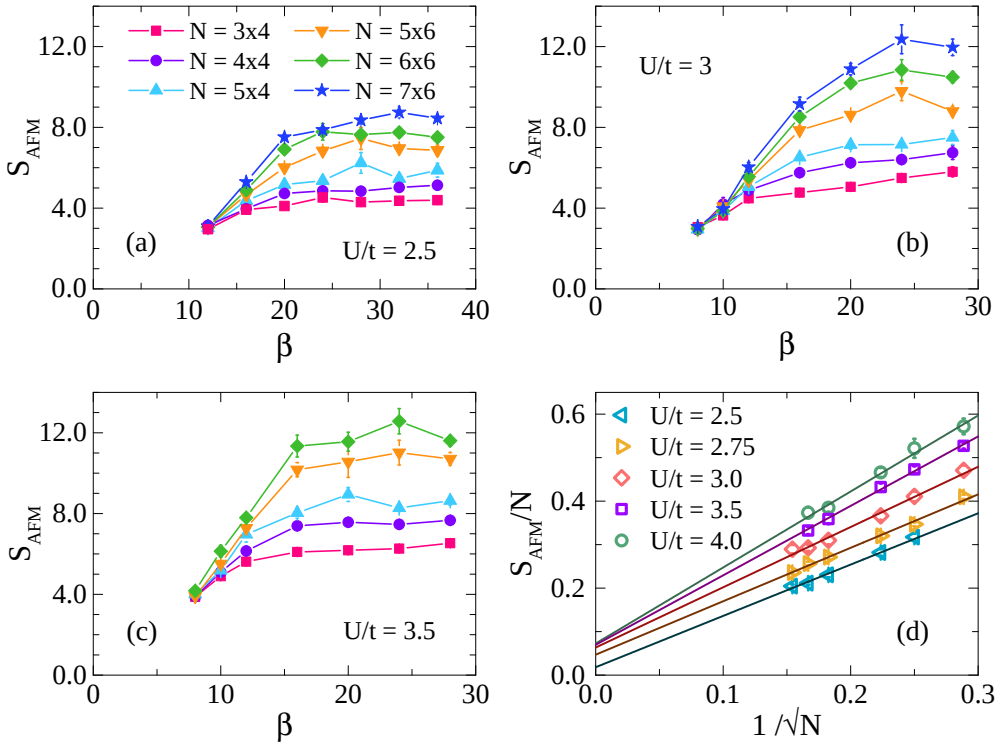

Figure 5.12: Antiferromagnetic structure factor as a function of β for (a) $U/t = 2.5$, (b) $U/t = 3$ and (c) $U/t = 3.5$. At lower temperatures, the structure factor stabilizes, allowing for extrapolations to the thermodynamic limit [4], as illustrated in panel (d). When not shown, error bars are smaller than symbol size.

normalize the low-temperature results by the lattice size using the linear spin-wave scaling by Huse [4], in which

$$S_{AFM}/N = A + B/\sqrt{N} + \mathcal{O}(1/N)$$

where $A = 4m_{AFM}^2$, and with m_{AFM} being the ground-state AFM order parameter in the thermodynamic limit. The constant 4 in $A = 4m_{AFM}^2$ arises from our definition of the structure factor S_{AFM} in Eq. (5.16), which has the same multiplicative factor applied to $\langle S_{\mathbf{i}}^z S_{\mathbf{j}}^z \rangle$. This allows us to understand the behavior of the system at the thermodynamic limit ($1/N \to 0$ and $T = 0$ limit). The extrapolations, shown in Fig. 5.12 (d), are finite in the $1/N \to 0$ limit, indicating that the system remains magnetic even for $U/t = 2.5$, in stark contrast to the pristine honeycomb lattice, which becomes magnetic only for $U/t \geq 3.8$ [151, 106, 5].

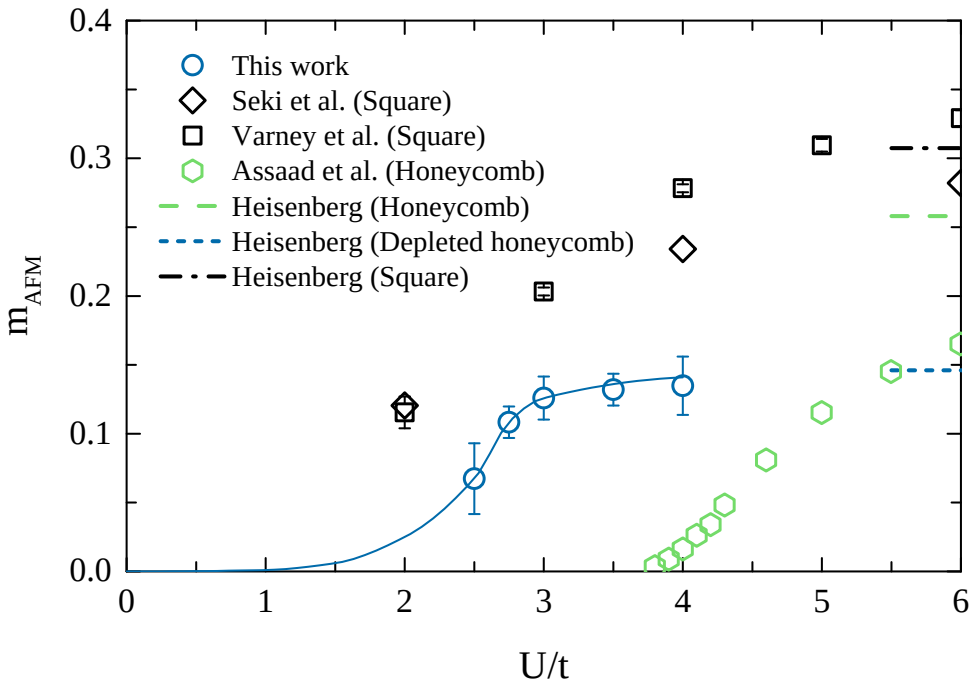

Figure 5.13: Antiferromagnetic order parameter as a function of U/t (blue circle symbols). The points were obtained at the thermodynamic limit from the data displayed in Fig. 5.12 (d), as detailed on the text. The solid line is a guide to the eye. The green hexagon symbols represent DQMC values for the honeycomb lattice (Ref. [5]), while the black square and diamond symbols are QMC results for the square lattice (Refs. [6] and [7] respectively). The horizontal lines denote the Heisenberg limit for the square (black dashed-dotted line; Ref. [8]), pristine honeycomb (green dashed line; Ref. [9]), and depleted honeycomb lattices (blue short dashed line; the value used here was the average AFM order parameter found in Sec. 5.3.3 of this Chapter).

The AFM order parameter m_{AFM}, obtained in Fig. 5.12 (d), is displayed in Fig. 5.13 (blue open circle symbols), along with the values of m_{AFM} for the pristine honeycomb lattice presented in Ref. [5] (green open hexagon symbols). Notice that the strong-coupling limit for the depleted lattice (horizontal blue short-dashed line) is nearly achieved at $U/t = 4$. In contrast, larger values of U/t are required to approach the strong coupling limit for the pristine honeycomb lattice (horizontal green dashed line). This difference in behavior can be attributed to instabilities associated with the van Hove singularity, which enhances the local moment formation as a function of U/t, effectively freezing the charge degrees of freedom. A similar feature is observed for the square lattice [6, 7], as illustrated

in Fig. 5.13. However, the magnetization for the Heisenberg model on the depleted lattice is smaller than that of the square and pristine honeycomb lattices due to the reduced coordination number. In light of these results, along with the MFT and LSWT results, we conclude that AFM order is likely present for any interaction strength in the depleted lattice.

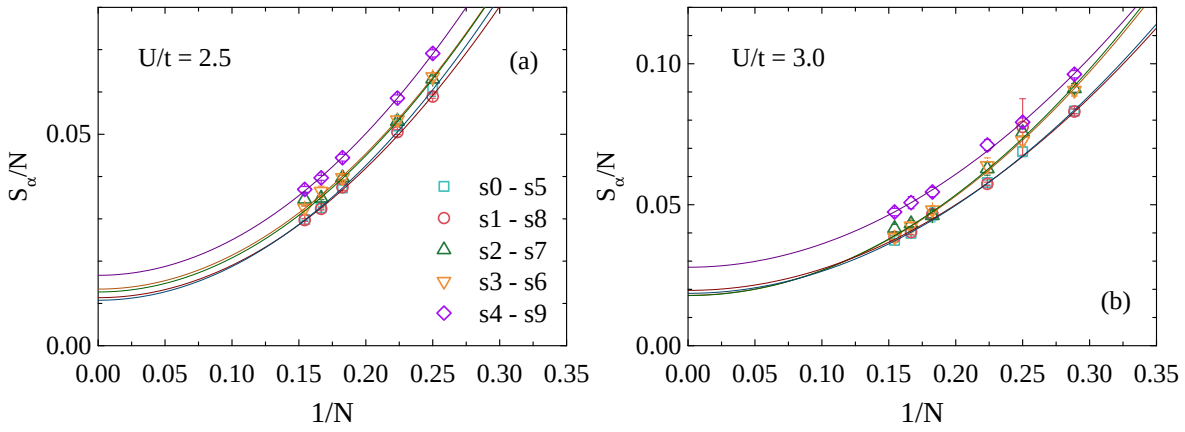

Figure 5.14: Extrapolation of the structure factor for individual orbitals as a function of inverse system size for (a) $U/t = 2.5$ and (b) $U/t = 3$.

We finish the analysis of the magnetic properties by examining the main orbital contributions to the AFM order. To this end, notice that Eq. (5.16) may be written as

$$S_{AFM} = 4\frac{1}{10}\frac{1}{N}\sum_{\mathbf{r},\mathbf{r}'}\sum_{\alpha,\gamma}(-1)^{\alpha+\gamma}\langle S^z_{\mathbf{r},\alpha}S^z_{\mathbf{r}',\gamma}\rangle \ . \tag{5.17}$$

Among the 55 possible orbital combinations, we focus on those where $\alpha = \gamma$, which represents the contribution of individual orbitals to the global order parameter. We then define

$$S_\alpha = \frac{1}{N}\sum_{\mathbf{r},\mathbf{r}'}\langle S^z_{\mathbf{r},\alpha}S^z_{\mathbf{r}',\alpha}\rangle. \tag{5.18}$$

Notice that the spin-spin correlations for orbitals on the same sublattice are ferromagnetic; thus, $S_\alpha > 0$. Figure 5.14 presents the behavior of S_α, averaged over equivalent orbitals, for (a) $U/t = 2.5$ and (b) $U/t = 3$, as a function of the system size at low temperature (i.e. for large values of β, where the structure factor has stabilized as in Fig. 5.12).

An important remark must be made here: There is a noticeable difference between the contributions from the orbitals $(s4, s9)$ and the others. Interestingly, these orbitals have the highest responses at the mean-field solution and in the LSWT approach.

Now, we turn our attention to the electronic compressibility $\kappa = \frac{1}{n^2}\frac{\partial n}{\partial \mu}$, with $n = \frac{1}{N}\left\langle \sum_{\mathbf{i},\sigma} n_{i\sigma} \right\rangle$. In order to perform the derivative $\frac{\partial n}{\partial \mu}$, we vary the chemical potential μ by $\Delta\mu = 0.05$, thus changing the density n. The result is displayed in Fig. 5.15 (a) as a function of temperature. In a metallic phase, κ has finite values, but for an insulator we have $\kappa \to 0$ because $n(\mu)$ exhibits a plateau as $T \to 0$.

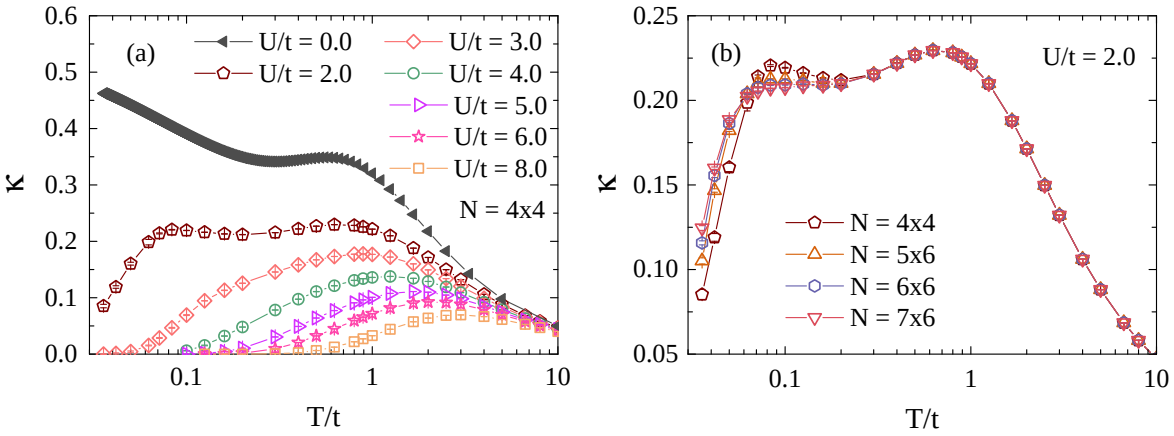

Figure 5.15: (a) Electronic compressibility as a function of T/t for different values of U/t and a depleted honeycomb lattice of size $N = 4 \times 4$. (b) Comparison of κ for different lattice sizes and $U/t = 2.0$. For $U/t = 2$, the compressibility displays a double-peaked structure due to finite size effects, as can be seen in the $N = 4 \times 4$ curve. A careful analysis with system size shows that the peak at $T/t \approx 0.083$ disappears as the system size increases. Therefore, the peak at $T/t = 0.625$ is the actual low-temperature peak for $U/t = 2.0$.

These features are present in our interacting NLSM, as displayed in Fig. 5.15 (a), with $\kappa \to 0$ for any $U/t > 0$ at low temperatures. That is, as the temperature is lowered, the system enters an insulating phase with strong short-range spin correlations, which eventually give rise to long-range AFM order in the ground state. It is important to note that the curve for $U/t = 2.0$ in Fig. 5.15 (a) has two peaks, the first at $T/t = 0.625$ and the second at $T/t = 0.083$. However, in Fig. 5.15 (b) it is possible to see that κ depends

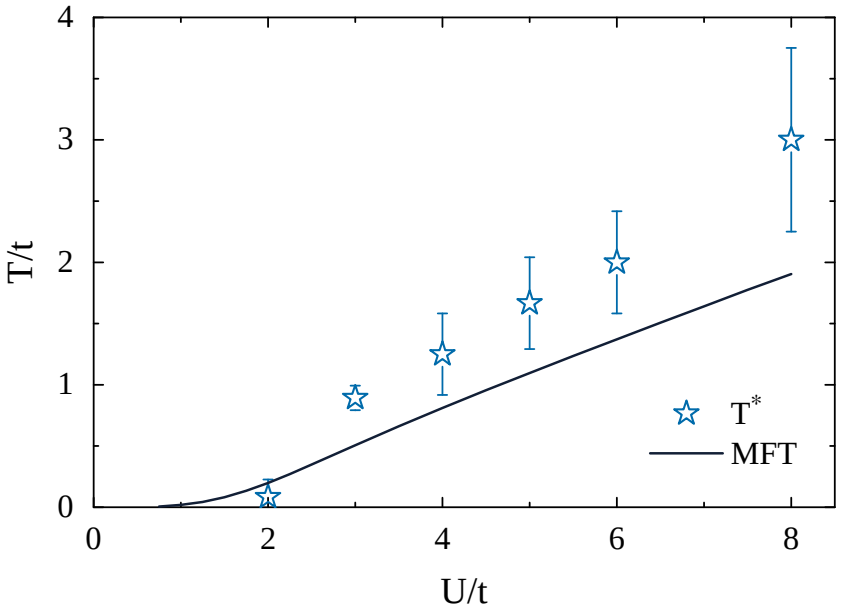

Figure 5.16: Temperature scale T^* defined by the low-temperature maxima for the compressibility (open stars) and mean-field Néel temperature (solid line).

on the system size for temperatures lower than $T/t < 0.2$, implying that the peak at $T/t = 0.083$ is actually a finite size effect and should disappear as $N \to \infty$. Therefore, in Fig. 5.16 we have considered the peak at $T/t = 0.625$.

The temperature scale for the onset of the insulating phase, denoted as T^*, is presented in Fig. 5.16. It corresponds to the temperature of the lowest peak in the compressibility. Within a mean-field approach, long-range order occurs at the same temperature as the metal-insulator transition. Therefore, it is important to compare the mean-field Néel temperature with the T^* from QMC, as presented in Fig. 5.16. Interestingly, these energy scales are similar, indicating that the mean-field approach successfully captures short-range effects.

5.4 Conclusions

In this Chapter, we investigate the interacting properties of the repulsive Hubbard model on a nonsymmorphic depleted honeycomb lattice which, in the noninteracting regime,

exhibits symmetry-enforced and accidental nodal lines for the isotropic lattice and for a special anisotropic one. The crossing of the nodal lines leads to a van Hove singularity at zero energy in the local density of states, making the system unstable to interactions at half-filling. Generic anisotropy gaps the accidental nodal line, thus removing the associated van Hove singularity.

In the interacting case ($U/t > 0$), we analyze the model using three different approaches: mean-field theory (MFT), linear spin wave theory (LSWT), and determinant quantum Monte Carlo (DQMC) simulations. This allows us to examine the weak, strong, and intermediate coupling limits, respectively.

Within the mean-field approach, we observe that the system becomes magnetic and opens a gap in the spectrum for any $U/t > 0$, which can be attributed to the presence of the van Hove singularity in the noninteracting regime. Moreover, the magnetism is inhomogeneous within the unit cell, with orbitals $s4$ and $s9$ exhibiting the largest responses. The onset of an inhomogeneous magnetic order for arbitrarily weak e-e interaction in nonsymmorphic holey graphene is to be contrasted with the magnetization of the pristine honeycomb lattice, which is homogeneous and requires $U/t > 3.8$.

In the opposite limit, as $U/t \to \infty$, our LSWT analysis for the Heisenberg model yields a global antiferromagnetic order parameter $m_{AFM} \approx 0.146$, which is significantly smaller than the value for the pristine honeycomb lattice, $m_{AFM} \approx 0.258$ [9]. This reduction is attributed to the smaller effective coordination number in the former case. Nevertheless, in agreement with the previous MFT solution, the magnetic responses exhibit inhomogeneities, with the largest contributions again arising from orbitals $s4$ and $s9$.

For the intermediary regime of e-e interactions, we employed QMC simulations to investigate the isotropic lattice. We started by analyzing double occupancy, which exhibits a change in the sign of $\partial D/\partial T$ as a function of temperature. This behavior is crucial for identifying bad metalicity, anomalies in the Seebeck coefficient, and adiabatic cooling. Additionally, our analysis of the spin-spin correlation functions reveals an inhomogeneous

magnetic response, consistent with both the MFT and LSWT limits, and stronger correlations than that of the pristine honeycomb lattice in the weakly interacting regime. Consistent with the MFT result, we obtain a staggered antiferromagnetic order for any $U/t > 0$ also in the intermediary e-e interaction regime, a stark contrast to the Hubbard model on the honeycomb lattice. It is important to notice that the MFT results are valid in the $U \to 0$ limit, where the antiferromagnetic order parameter becomes exponentially small. Outside this limit, MFT overestimates the order parameter, which renders a quantitative comparison of our DQMC and MFT results impossible. For large values of U/t, the QMC order parameter agrees with the LSWT results, valid in the strongly interacting regime.

Finally, our analysis of the electronic compressibility shows insulating behavior at low temperatures with long-range antiferromagnetic order and metal-insulator transition occurring simultaneously. This collection of results demonstrates that vacancy engineering can qualitatively change the magnetic phase transition of a crystal and substantially alter the magnetization and spin correlations in the magnetic phase, thus providing a practical mechanism for designing quantum materials with tailored magnetic characteristics.

The contents of this chapter appear in Ref. [78].

Chapter 6

Photoinduced enhancement of superconductivity in the bilayer Hubbard and t-J models

6.1 Introduction

Cuprates are compounds with high appeal due to exhibiting high temperature superconductivity. However, the critical temperature T_c from which superconductivity is suppressed is still lower than ambient temperature, limiting applications. This has motivated investigations on ways to raise T_c [167]. Among these, experiments involving photoirradiation have been attracting attention [168].

These experiments utilize laser pulses to excite the vibrational modes of the oxygen atoms of the cuprates, facilitating tunneling between the layers of the material [169].These experiments can be modeled and studied from a theoretical approach, allowing to better understand the mechanisms that enhance tunneling [170, 171].

With this in mind, in this Chapter we investigate how to use photoirradiation to induce superconductivity in a cuprate. To model the tunneling seen in experiments with $YBa_2Cu_3O_{6+\delta}$ we consider the bilayer Hubbard and t-J models (Fig. 6.1).

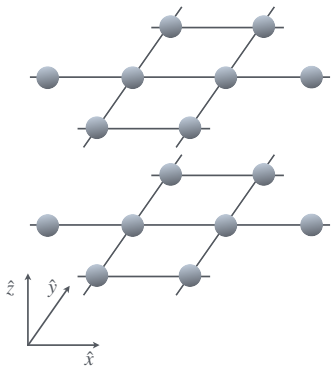

Figure 6.1: Bilayer square lattice with $N = 16$ sites (8 sites per layer).

6.2 The repulsive Hubbard model and the t-J model

In this chapter we will analyze the bilayer Hubbard and t-J models through exact diagonalization calculations. The Hubbard Hamiltonian is shown in Eq. (2.10). To introduce hopping between bilayers, we define $t_{\mathbf{i},\mathbf{j}} = t$ ($t_\perp$) as the hopping amplitude in (between) layers, and set the interlayer hopping to $t_\perp = 0.1t$. The time is measured in terms of t^{-1} and $\hbar = 1$. As the interaction strength increases, the energetic cost for two electrons to occupy the same orbital is extremely high. In the strongly correlated limit ($U \gg t$) we have the t-J model

$$\mathcal{H}_{\mathrm{tJ}} = -\sum_{\langle \mathbf{i},\mathbf{j}\rangle,\sigma} \left(t_{\mathbf{i},\mathbf{j}} c^\dagger_{\mathbf{i}\sigma} c_{\mathbf{j}\sigma} + \mathrm{H.c.}\right) + \sum_{\mathbf{i}} J_{\mathbf{i},\mathbf{j}} \left(\hat{S}_{\mathbf{i}} \cdot \hat{S}_{\mathbf{j}} - \frac{1}{4} n_{\mathbf{i}} n_{\mathbf{j}}\right), \tag{6.1}$$

where $J_{\mathbf{i},\mathbf{j}} = J$ ($J_\perp$) is the exchange between electrons that belong to the same (different) layer and $-\frac{1}{4} n_{\mathbf{i}} n_{\mathbf{j}}$ is included to account for the absence of double occupancy in this model. We focus on the $U \gg t$ limit, where $J_{\mathbf{i},\mathbf{j}} \approx 4{t_{\mathbf{i},\mathbf{j}}}^2/U$. In our simulations, we define the interlayer exchange as $J_\perp = 0.01J$ [172]. We focus on the doped case, with $n = 0.875$ for the system with $N = 16$ sites and $n = 0.9$ for the system with $N = 20$ sites.

To mimic the photoirradiation performed experimentally with the use of a laser beam, we perform a Peierls substitution on the hopping amplitude t in Eqs. (**??**) and (6.1)

$$t_{\mathbf{i},\mathbf{j}} \hat{c}^\dagger_{\mathbf{i},\sigma} \hat{c}_{\mathbf{j},\sigma} + \mathrm{H.c.} \rightarrow t_{\mathbf{i},\mathbf{j}} e^{i\mathbf{A}(t)\cdot(\mathbf{r_i}-\mathbf{r_j})} \hat{c}^\dagger_{\mathbf{i},\sigma} \hat{c}_{\mathbf{j},\sigma} + \mathrm{H.c.}, \tag{6.2}$$

where $\mathbf{A}(t)$ is the spatially uniform vector potential. To mimic an ultrafast photoirradiation, we chose $\mathbf{A}(t)$ as

$$\mathbf{A}(t) = A_0 e^{-(t-t_0)/2t_d^2} \cos\left[\omega_0(t-t_0)+\varphi\right]\mathbf{e}_z, \tag{6.3}$$

that is, an oscillatory Gaussian centered at t_0, with width t_d, frequency ω_0, amplitude A_0 and polarized in the z-direction.

The simulations are performed with the time-dependent Lanczos method [173, 174], with the time evolution being obtained through $|\Psi(t+dt)\rangle = e^{-i\hat{\mathcal{H}}(\hat{t})dt}|\Psi(t)\rangle$ with dt being a sufficiently small time step. The initial states $\Psi(t\to-\infty)\rangle$ are the ground state of Eqs. (2.10) and (6.1) and the wave function $|\Psi(t)\rangle$ and the quantities of interest are evaluated at each instant dt, allowing to monitor how the properties of the system evolve in time.

Since the t-J model does not allow double occupancy, its Hilbert space is smaller than that of the Hubbard model leading to faster simulations. Therefore, here we study the bilayer Hubbard and t-J models on a lattice with $N = 16$ sites and periodic boundary conditions. We set our parameters in such a way that we can compare the results of both models.

6.3 Equilibrium results

To understand how the photoirradiation affects our systems we divide our analysis in two parts: firstly we observe the properties of the system without perturbations. In particular, we investigate the d-wave pairing structure factor

$$P_d = \frac{1}{N}\sum_{\mathbf{i},\mathbf{dr}} \langle \hat{\Delta}_{\mathbf{i}}^{(d)} \hat{\Delta}_{\mathbf{i}+\mathbf{dr}}^{(d)\,\dagger} \rangle, \tag{6.4}$$

where $\hat{\Delta}_{\mathbf{i}}^{(d)} = \left(\hat{c}_{\mathbf{i}+\hat{\mathbf{x}},\sigma} + f(d)\hat{c}_{\mathbf{i}+\hat{\mathbf{y}},\sigma}\right)\hat{c}_{\mathbf{i},\sigma}$, with $f(d) = +1$. We analyze P_d across the low-lying spectrum, to understand where superconductivity is more likely to be enhanced by the photoirradiation. In Fig. 6.2 we have the eigenstates expectation values of the

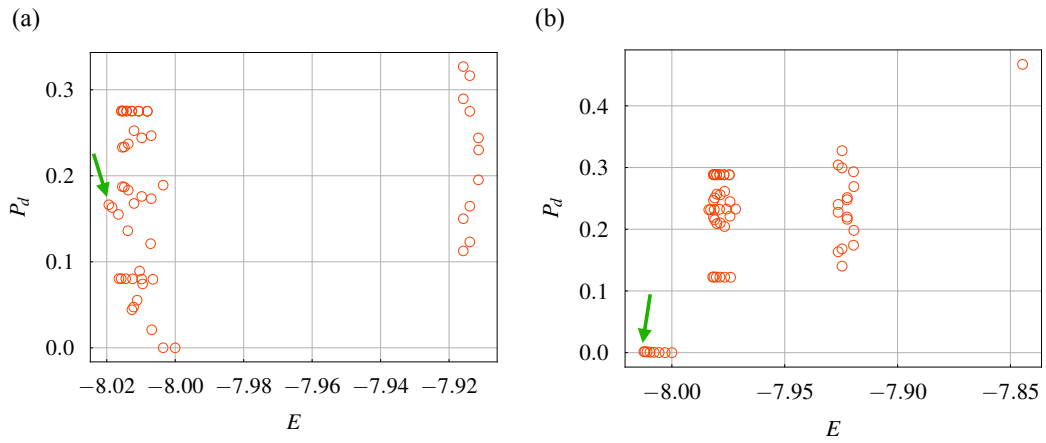

Figure 6.2: d-wave structure factor in the ground state and the first few excited states for the (a) Hubbard and (b) t-J models. The green arrows indicate the ground state.

d-wave structure factor. To compare the results for the Hubbard and the t-J models we set $U/t = 20.0$ and $J/t = 0.2$. For both models the energy scale is similar, showing that for the parameters chosen, however, the configuration of the low-lying spectrum is not identical. For the Hubbard case, there is a group of excited states with energy gap of $E_\alpha - E_0 \simeq 0.05t$ with d-wave pairing $P_d \simeq 0.27$, while for the ground state $P_d \simeq 0.16$. For the t-J case, there are three groups of states with higher P_d. The ones closest to the ground state have $P_d \simeq 0.24$ and energy gap $E_\alpha - E_0 \simeq 0.025t$. To understand how likely these states are to contribute to the dynamics at a certain time t, it is relevant to see how they couple to the current operator

$$\hat{\mathcal{J}} = \sum_{\langle \mathbf{i},\mathbf{j}\rangle,\sigma} (-it_{\mathbf{i},\mathbf{j}} \hat{c}^\dagger_{\mathbf{i},\sigma} \hat{c}_{\mathbf{j},\sigma} + \text{H.c.}). \tag{6.5}$$

In the systems we are trying to simulate, the pump is applied on the $\hat{z}$ direction, in order to enhance tunneling between layers. With this in mind, we focus on the z component of $\hat{\mathcal{J}}$, in particular, on the overlaps $|\langle\alpha|\mathcal{J}_z|0\rangle|^2$, displayed in Fig. 6.3. The overlaps $|\langle\alpha|\mathcal{J}_z|0\rangle|^2$, with α being an excited state, suggest that for the bilayer Hubbard and t-J models the ground state is the most influent in the dynamics. While this result does not exclude the possibility for different α states to participate in the dynamics, being accessed after the

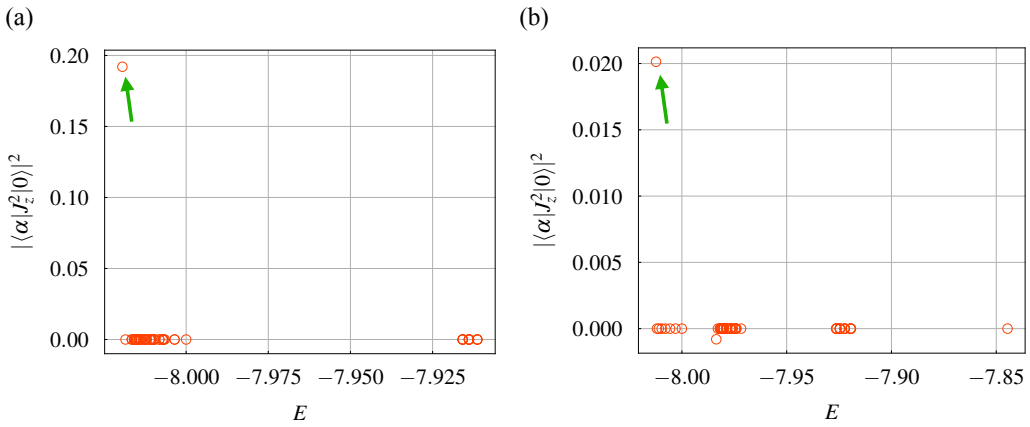

Figure 6.3: Overlaps of the current operator $\mathcal{J}_z$ between the ground and the α excited states for the (a) Hubbard and (b) t-J models. The green arrows indicate the ground state.

introduction of the pump, it indicates that the transition from the ground state to a given α state may require a fine-tuned perturbation to happen.

6.4 Out of equilibrium results

Now we add a time-dependent external field that can be adjusted to allow transitions between the ground and excited states. The pump used must be time constrained to prevent the system to continuously absorb energy. To find the optimal pump parameters that enhance superconductivity, we can adjust the amplitude, width and frequency of the pump. To do so, we associate t_d and ω_0 through $t_d = 3\frac{2\pi}{\omega_0}$ and then vary (A_0, ω_0). If we consider $t = 0.36$ eV [175], we have that a pump of $A_0 = 1.0$ corresponds to a pump fluence of ~ 10 mJ and a frequency of $\omega_0 = 0.05$ corresponds to ~ 0.02 eV or ~ 20 THz, in agreement with the parameters employed in photoirradiation experiments [168, 176, 177].

We begin our analysis by the bilayer t-J model. Firstly, we explore (A_0, ω_0) and observe how the d-wave pairing changes in time by taking $\Delta P_d = P_d(t_{max}) - P_d(t_{min})$, seen in Fig. 6.4. Here we see small islands of (A_0, ω_0) that enhance P_d. If we analyze the region

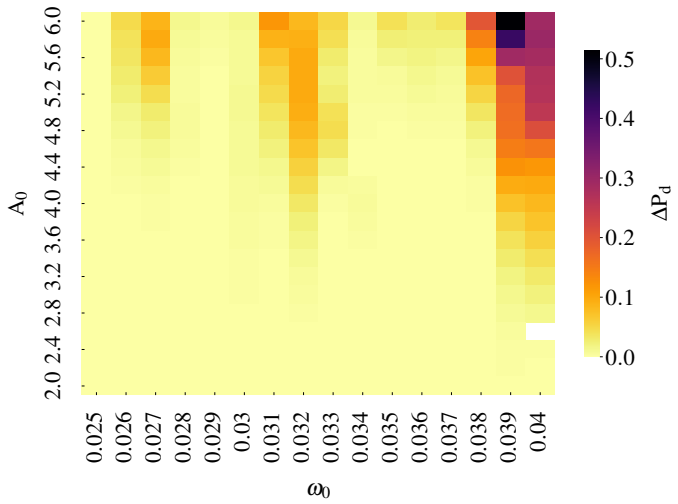

Figure 6.4: Contour plot of the enhancement of d-wave structure factor as a function of the amplitude and frequency of the pump for the t-J model with $J = 0.2$, $J_\perp = 0.002$, $t = 1.0$ and $t_\perp = 0.1$.

.

where the enhancement of P_d is more pronounced, we see that the energy given to the system is much higher than that of the states considered in the time evolution, meaning that the pulse is not targeting the desired states as intended. In Fig. 6.5 (a) we have the variation of P_d in time, given by $\Delta P_d = P_d(t_{max}) - P_d(t_{min})$, for a set of parameters (A_0, ω_0). In Fig. 6.5 (c) we see an increase in P_d that coincides with the decrease of the overlap of the wave function $|\psi\rangle$ with the ground state ($|\langle 0|\psi(t)\rangle|^2$) and the increase of its overlap with state $|\alpha = 21\rangle$. This implies that the pulse with parameters $A_0 = 9.0$ and $\omega_0 = 0.4$ was able to target state $|\alpha = 21\rangle$.

Due to constraints on the simulations times, it is not feasible to increase the size of the Hubbard bilayer. However, the t-J model allows to achieve larger lattices sizes. Fig. 6.6 displays d-wave structure factor. When comparing the d-wave structure factor for the bilayers with $N = 16$ [Fig. 6.6 (a)] and $N = 20$ sites [Fig. 6.6 (b)], we see that the low lying spectrum is completely different between. It is noteworthy that for the smaller system, the ground state has $P_d = 0$, while, for the larger one, $P_d \simeq 0.85$.

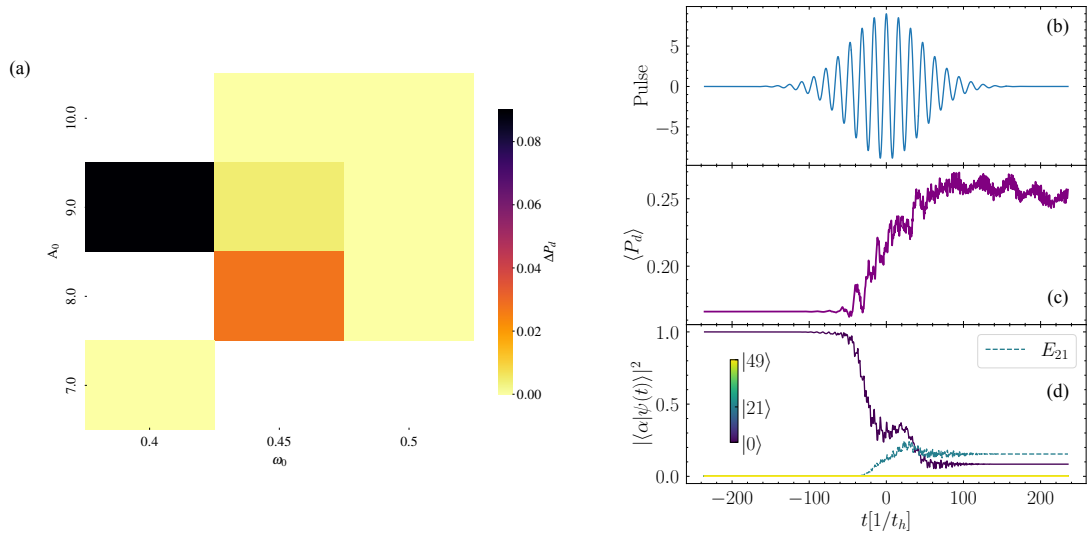

Figure 6.5: (a) Contour plot of ΔP_d, for different A_0 and ω_0. (b) Schematics of the pulse amplitude, (c) d-wave structure factor and (d) dynamics of the overlaps $|\langle\alpha|\psi(t)\rangle|^2$ as a function of t for $A_0 = 9.0$ and $\omega_0 = 0.4$.

6.5 Conclusions

In this Chapter we have presented the current results for the bilayer Hubbard and t-J models under photoirradiation. Our goal was to enhance d-wave superconductivity dynamically. We studied the underdoped regime, with $n = 0.875$ with small hopping between layers, where we noticed an increase in the pairing after allowing the system to evolve after applying a perturbation. While the presence of excited states with higher d-wave pairing than the ground state is promising, targeting these excited states has proven to be a difficult task. This might be connected with the fact that for the groups of parameters observed the low-lying spectrum of the system in equilibrium have very similar energies. Analysis of the overlaps of the target and ground states with the current operator show that, in first order, the target states are not likely influenced by the dynamics.

Indeed, while the pump disturbs the system enough to slightly enhance superconductivity, the energy injected is not applied in an orderly fashion to successfully access the desired states while maintaining the increase in P_d after the system is allowed to relax.

Simulation costs limit increasing the size of the system for the bilayer Hubbard model,

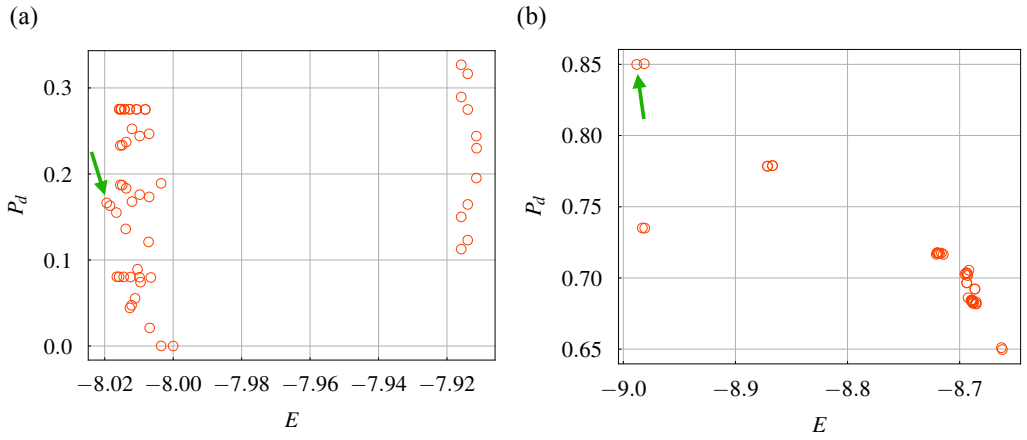

Figure 6.6: d-wave structure factor for bilayers with (a) $N = 16$ and (b) $N = 20$ sites. Results for the t-J model with $J = 0.2$, $J_\perp = 0.002$, $t = 1.0$ and $t_\perp = 0.1$.

but it is feasible for the bilayer t-J model. Preliminary analysis show that the low-lying spectrum of this model is greatly impacted by the difference in size. This work is in progress and will be prepared for publication when finished.

Chapter 7

Concluding remarks

In this thesis we investigated properties of the Hubbard model on different geometries through tight-binding and mean-field calculations, exact diagonalization and quantum Monte Carlo simulations. We were able to contribute towards a better understanding of the Hubbard model on the kagome lattice, we also proposed an approximation to the single-site entaglement at finite temperatures as a proxy to identify quantum phase transitions. We then investigated how vacancy-engineering a nonsymmorphic geometry affects magnetis and finally studied the possibility of targeting states with a time-dependent perturbation to enhance superconductivity.

Firstly, we analyzed the properties of the repulsive Hubbard model on a kagome lattice. Through DQMC simulations it was established that it is possible to adiabatically cool this system by increasing U/t. There are evidences for the absence of collective spin-wave excitations in the ground state, supported by the suppression of the low-temperature peak, that is consistent for all U/t observed. This is further evidenced by the spin-spin correlation functions that although are very intense between nearest neighbors, decrease rapidly for greater distances. We also observe that the homogeneous magnetic susceptibility displays a behavior consistent with a metallic state for lower U/t. However, we are unable to confirm whether this changes for higher U/t since the sign problem prevents us from exploring the low-temperature limit in this case. We have contributed towards the discussion about the metal-to-insulator transition for this system. By analyzing three

different quantities, namely the electronic compressibility, density of states at the Fermi level and current-current correlation functions, we gathered solid evidence for a Mott transition at $U_c/t = 6.5 \pm 0.5$.

Still on the subject of Mott transitions and motivated by the cone of fluctuations produced by quantum critical points at $T = 0$ we have investigated the possibility of computing single-site entanglement at finite temperatures. We employed DQMC to obtain the single-site entanglement for the Hubbard model on the honeycomb and kagome lattices and for the ionic Hubbard model on the square lattice aiming to identify its reliability in identifying quantum phase transitions for these two-dimensional systems. Our findings suggest that the single-site entanglement is efficient to signal the critical Hubbard U at which Mott and band-insulator-to-metal transitions happen, and the filling at which Mott transition happens. This analysis provide satisfactory results for temperatures $T \leq 1.0$.

We also investigated the properties of a nonsymmorphic depleted honeycomb lattice vacancy-engineered from a pristine honeycomb lattice. We observed the presence of symmetry-enforced and accidental nodal lines for the depleted lattice and established that their crossing leads to a van Hove singularity in the local density of states, making the system unstable to interactions at half-filling. This is corroborated by mean-field theory calculations showing that the system becomes magnetic for any $U/t > 0$, in direct contrast with the pristine honeycomb lattice. The removal of sites of the lattice resulted in inhomogeneous magnetism within the unit cell, with stronger responses for orbitals with smaller coordination number, which is also at odds with the pristine honeycomb lattice, that has homogeneous magnetization and undergoes a Mott transition for $U/t > 3.8$. The inhomogeneity is consistent in the weak, strong and intermediate coupling limits, as can be seen through mean-field theory, linear spin wave theory and DQMC simulations, respectively. By employing these different techniques we are able to have a good understanding of the antiferromagnetic order parameter in all interacting limits. The depleted lattice also shows insulating behavior at low-temperatures with long-range antiferromagnetic order

and metal-insulator transition occurring simultaneously.

And finally, we investigated the introduction of time-dependant perturbations in the bilayer Hubbard and t-J models. Our preliminary findings suggest the possibility to increase d-wave pairing and enhance superconductivity by applying a fine-tuned perturbation that allows us to target certain states of our system.

Bibliography

[1] M. R. Norman, "Colloquium: Herbertsmithite and the search for the quantum spin liquid", *Rev. Mod. Phys.* **88**, 041002 (2016). xii, 1, 2

[2] L. O. Lima, A. R. Medeiros-Silva, R. R. dos Santos, T. Paiva, N. C. Costa, "Magnetism and metal-insulator transitions in the anisotropic kagome lattice", *Phys. Rev. B* **108**, 235163 (2023). xiv, 5, 27, 28, 29, 30

[3] F. Liu, F. Qu, I. Žutić, M. Malard, "Vacancy-engineered nodal-line semimetals", *Sci. Rep.* **12**, 14981 (2022). xvi, 44, 45, 48, 49

[4] D. A. Huse, "Ground-state staggered magnetization of two-dimensional quantum Heisenberg antiferromagnets", *Phys. Rev. B* **37**, 2380 (1988). xviii, 62

[5] F. F. Assaad, I. F. Herbut, "Pinning the Order: The Nature of Quantum Criticality in the Hubbard Model on Honeycomb Lattice", *Phys. Rev. X* **3**, 031010 (2013). xix, 35, 40, 46, 55, 62, 63

[6] C. N. Varney, *et al.*, "Quantum Monte Carlo study of the two-dimensional fermion Hubbard model", *Phys. Rev. B* **80**, 075116 (2009). xix, 63

[7] K. Seki, S. Sorella, "Benchmark study of an auxiliary-field quantum Monte Carlo technique for the Hubbard model with shifted-discrete Hubbard-Stratonovich transformations", *Phys. Rev. B* **99**, 144407 (2019). xix, 63

[8] A. W. Sandvik, H. G. Evertz, "Loop updates for variational and projector quantum Monte Carlo simulations in the valence-bond basis", *Phys. Rev. B* **82**, 024407 (2010). xix, 63

[9] E. V. Castro, N. M. R. Peres, K. S. D. Beach, A. W. Sandvik, "Site dilution of quantum spins in the honeycomb lattice", *Phys. Rev. B* **73**, 054422 (2006). xix, 63, 67

[10] J. S. Helton, *et al.*, "Spin Dynamics of the Spin-1/2 Kagome Lattice Antiferromagnet $ZnCu_3(OH)_6Cl_2$", *Phys. Rev. Lett.* **98**, 107204 (2007). 1

[11] J. S. Helton, *et al.*, "Dynamic Scaling in the Susceptibility of the Spin-$\frac{1}{2}$ Kagome Lattice Antiferromagnet Herbertsmithite", *Phys. Rev. Lett.* **104**, 147201 (2010). 1

[12] T.-H. Han, *et al.*, "Fractionalized excitations in the spin-liquid state of a kagome-lattice antiferromagnet", *Nature* **492**, 406 (2012). 1

[13] M. Fu, T. Imai, T.-H. Han, Y. S. Lee, "Evidence for a gapped spin-liquid ground state in a kagome Heisenberg antiferromagnet", *Science* **350**, 655 (2015). 1

[14] S. Kempkes, *et al.*, "Robust zero-energy modes in an electronic higher-order topological insulator", *Nature Materials* **18**, 1292 (2019). 1

[15] S. Sun, *et al.*, "Designing Kagome Lattice from Potassium Atoms on Phosphorus–Gold Surface Alloy", *Nano Letters* **20**, 5583 (2020). PMID: 32568547. 1

[16] G.-B. Jo, *et al.*, "Ultracold Atoms in a Tunable Optical Kagome Lattice", *Phys. Rev. Lett.* **108**, 045305 (2012). 1

[17] T. H. Barter, *et al.*, "Spatial coherence of a strongly interacting Bose gas in the trimerized kagome lattice", *Phys. Rev. A* **101**, 011601(R) (2020). 1

[18] T.-H. Leung, *et al.*, "Interaction-Enhanced Group Velocity of Bosons in the Flat Band of an Optical Kagome Lattice", *Phys. Rev. Lett.* **125**, 133001 (2020). 1

[19] G. Vidal, J. I. Latorre, E. Rico, A. Kitaev, "Entanglement in Quantum Critical Phenomena", *Phys. Rev. Lett.* **90**, 227902 (2003). 2

[20] A. Osterloh, L. Amico, G. Falci, R. Fazio, "Scaling of entanglement close to a quantum phase transition", *Nature* **416**, 608–610 (2002). 2

[21] P. Zanardi, "Quantum entanglement in fermionic lattices", *Phys. Rev. A* **65**, 042101 (2002). 2, 33

[22] S.-J. Gu, S.-S. Deng, Y.-Q. Li, H.-Q. Lin, "Entanglement and Quantum Phase Transition in the Extended Hubbard Model", *Phys. Rev. Lett.* **93**, 086402 (2004). 2, 33, 34, 38

[23] i. c. v. Brukner, V. Vedral, A. Zeilinger, "Crucial role of quantum entanglement in bulk properties of solids", *Phys. Rev. A* **73**, 012110 (2006). 2

[24] V. V. França, G. A. Prataviera, "Stability and entanglement in optical-atomic amplification of trapped atoms: The role of atomic collisions", *Phys. Rev. A* **75**, 043604 (2007). 2

[25] T. Chakraborty, H. Singh, D. Das, T. K. Sen, C. Mitra, "Quantification of entanglement from magnetic susceptibility for a Heisenberg spin 1/2 system", *Physics Letters A* **376**, 2967 (2012). 2

[26] S. Ghosh, T. Rosenbaum, G. Aeppli, S. Coppersmith, "Entangled Quantum States of Magnetic Dipoles", *Nature* **425**, 48 (2003). 2

[27] D. Larsson, H. Johannesson, "Single-site entanglement of fermions at a quantum phase transition", *Phys. Rev. A* **73**, 042320 (2006). 2

[28] S.-S. Deng, S.-J. Gu, H.-Q. Lin, "Block-block entanglement and quantum phase transitions in the one-dimensional extended Hubbard model", *Phys. Rev. B* **74**, 045103 (2006). 2

[29] T. Brünner, E. Runge, A. Buchleitner, V. V. França, "Entanglement enhancement in spatially inhomogeneous many-body systems", *Phys. Rev. A* **87**, 032311 (2013). 2

[30] T. Mendes-Santos, T. Paiva, R. R. dos Santos, "Entanglement, magnetism, and metal-insulator transitions in fermionic superlattices", *Phys. Rev. B* **87**, 214407 (2013). 2

[31] G. A. Canella, V. V. França, "Mott-Anderson metal-insulator transitions from entanglement", *Phys. Rev. B* **104**, 134201 (2021). 2, 37

[32] G. A. Canella, K. Zawadzki, V. V. França, "Effects of temperature and magnetization on the Mott–Anderson physics in one-dimensional disordered systems", *Scientific Reports* **12**, 8709 (2022). 2

[33] A. Anfossi, C. D. E. Boschi, A. Montorsi, F. Ortolani, "Single-site entanglement at the superconductor-insulator transition in the Hirsch model", *Phys. Rev. B* **73**, 085113 (2006). 2, 33

[34] G. A. Canella, V. V. França, "Superfluid-Insulator Transition unambiguously detected by entanglement in one-dimensional disordered superfluids", *Scientific Reports* **9**, 15313 (2019). 2, 33

[35] K. Zawadzki, G. A. Canella, V. V. França, I. D'Amico, "Work Statistics and Entanglement Across the Fermionic Superfluid-Insulator Transition", *Advanced Quantum Technologies* **7**, 2300237 (2024). 2

[36] V. França, "Entanglement and exotic superfluidity in spin-imbalanced lattices", *Physica A: Statistical Mechanics and its Applications* **475**, 82 (2017). 2, 33, 34

[37] D. Arisa, V. V. França, "Linear mapping between magnetic susceptibility and entanglement in conventional and exotic one-dimensional superfluids", *Phys. Rev. B* **101**, 214522 (2020). 2, 31, 33, 34, 36, 42

[38] H. Ju, A. B. Kallin, P. Fendley, M. B. Hastings, R. G. Melko, "Entanglement scaling in two-dimensional gapless systems", *Phys. Rev. B* **85**, 165121 (2012). 3

[39] Y.-B. Guo, *et al.*, "Entanglement entropy of non-Hermitian free fermions", *Journal of Physics: Condensed Matter* **33**, 475502 (2021). 3

[40] T. Grover, "Entanglement of Interacting Fermions in Quantum Monte Carlo Calculations", *Phys. Rev. Lett.* **111**, 130402 (2013). 3

[41] R. Blankenbecler, D. J. Scalapino, R. L. Sugar, "Monte Carlo calculations of coupled boson-fermion systems. I", *Phys. Rev. D* **24**, 2278 (1981). 3, 6, 47

[42] J. E. Hirsch, "Two-dimensional Hubbard model: Numerical simulation study", *Phys. Rev. B* **31**, 4403 (1985). 3, 35, 41, 47

[43] P. Broecker, S. Trebst, "Rényi entropies of interacting fermions from determinantal quantum Monte Carlo simulations", *Journal of Statistical Mechanics: Theory and Experiment* **2014**, P08015 (2014). 3

[44] F. F. Assaad, "Stable quantum Monte Carlo simulations for entanglement spectra of interacting fermions", *Phys. Rev. B* **91**, 125146 (2015). 3

[45] G. Pan, *et al.*, "Stable computation of entanglement entropy for two-dimensional interacting fermion systems", *Phys. Rev. B* **108**, L081123 (2023). 3

[46] X. Zhang, G. Pan, B.-B. Chen, K. Sun, Z. Y. Meng, "Integral algorithm of exponential observables for interacting fermions in quantum Monte Carlo simulations", *Phys. Rev. B* **109**, 205147 (2024). 3

[47] J. D'Emidio, R. Orús, N. Laflorencie, F. de Juan, "Universal Features of Entanglement Entropy in the Honeycomb Hubbard Model", *Phys. Rev. Lett.* **132**, 076502 (2024). 3

[48] S. Murakami, "Phase transition between the quantum spin Hall and insulator phases in 3D: Emergence of a topological gapless phase", *New J. Phys.* **9**, 356 (2007). 3

[49] A. A. Burkov, "Topological semimetals", *Nat. Mater.* **15**, 1145 (2016). 3

[50] H. Weng, C. Fang, Z. Fang, B. A. Bernevig, X. Dai, "Weyl Semimetal Phase in Noncentrosymmetric Transition-Metal Monophosphides", *Phys. Rev. X* **5**, 011029 (2015). 3

[51] R. Wan, A. M. Turner, A. Vishwanath, S. Y. Savrasov, "Topological Semimetal and Fermi-arc Surface States in the Electronic Structure of Pyrochlore Iridates", *Phys. Rev. B* **83**, 205101 (2011). 3

[52] A. A. Burkov, Y. B. Kim, "$\mathbb{Z}_2$ and Chiral Anomalies in Topological Dirac Semimetals", *Phys. Rev. Lett* **86**, 115113 (2016). 3

[53] I. Žutić, A. Matos-Abiague, B. Scharf, H. Dery, K. Belashchenko, "Proximitized Materials", *Mater. Today* **22**, 85 (2019). 3

[54] L. Michel, J. Zak, "Connectivity of energy bands in crystals", *Phys. Rev. B* **59**, 5998 (1999). 3

[55] Y. Zhao, A. P. Schnyder, Z. Wang, "Unified theory of PT and CP invariant topological metals and nodal superconductors", *Phys. Rev. Lett.* **116**, 156402 (2016). 4

[56] A. P. Schnyder, "Lecture notes on: Accidental and symmetry-enforced band crossings in topological semimetals", *Topological Matter School, San Sebastian, Spain* (2018). 4

[57] S. M. Young, C. L. Kane, "Dirac Semimetals in Two Dimensions", *Phys. Rev. Lett.* **115**, 126803 (2015). 4

[58] J. Zhang, *et al.*, "Topological band crossings in hexagonal materials", *Phys. Rev. Mater.* **2**, 074201 (2018). 4

[59] H. Park, N. Son, B. H. Park, S. WooJoo, M. Kang, "Visible light-induced stable HER performance using duality of ultrafine Pt NPs in a *Z*-scheme *pn* junction Fe_2O_3@Pt@FeS catalyst", *Appl. Surf. Sci.* **541**, 148347 (2021). 4

[60] F. Xia, H. Wang, J. C. M. Hwang, A. H. C. Neto, L. Yang, "Black phosphorus and its isoelectronic materials", *Nat. Rev. Phys.* **1**, 306 (2019). 4

[61] J.-L. Lu, *et al.*, "Two-Dimensional Node-Line Semimetals in a Honeycomb-Kagome Lattice", *Chinese Physics Letters* **34**, 057302 (2017). 4

[62] B. Gao, *et al.*, "Density functional theory calculation on two-dimensional MoS_2/BiOX (X= Cl, Br, I) van der Waals heterostructures for photocatalytic action", *Appl. Surf. Sci.* **492**, 157 (2019). 4

[63] B. Song, *et al.*, "Observation of nodal-line semimetal with ultracold fermions in an optical lattice", *Nat. Phys.* **15**, 911 (2019). 4

[64] Y. Shao, *et al.*, "Electronic correlations in nodal-line semimetals", *Nat. Phys.* **16**, 636 (2020). 4

[65] G. Gatti, *et al.*, "Light-Induced Renormalization of the Dirac Quasiparticles in the Nodal-Line Semimetal ZrSiSe", *Phys. Rev. Lett.* **125**, 076401 (2020). 4

[66] M. Yang, *et al.*, "Magnetic and electronic properties of a topological nodal line semimetal candidate: HoSbTe", *Phys. Rev. Mater.* **4**, 094203 (2020). 4

[67] Y. Sun, *et al.*, "TM2B3 monolayers: Intrinsic anti-ferromagnetism and Dirac nodal line semimetal", *Applied Physics Letters* **121**, 183103 (2022). 4

[68] T. Shang, *et al.*, "Unconventional superconductivity in topological Kramers nodal-line semimetals", *Science Advances* **8**, eabq6589 (2022). 4

[69] M. Koshino, I. F. Hizbullah, "Magnetic susceptibility in three-dimensional nodal semimetals", *Phys. Rev. B* **93**, 045201 (2016). 4

[70] B. Roy, "Interacting nodal-line semimetal: Proximity effect and spontaneous symmetry breaking", *Phys. Rev. B* **96**, 041113 (2017). 4

[71] J. Wang, "Antiferromagnetic topological nodal line semimetals", *Phys. Rev. B* **96**, 081107 (2017). 4

[72] G. Jose, B. Uchoa, "Quantum critical scaling of gapped phases in nodal-line semimetals", *Phys. Rev. B* **101**, 115123 (2020). 4

[73] Z. Wu, Y. Wang, "Nodal topological superconductivity in nodal-line semimetals", *Phys. Rev. B* **108**, 224503 (2023). 4

[74] Y. Huh, E.-G. Moon, Y. B. Kim, "Long-range Coulomb interaction in nodal-ring semimetals", *Phys. Rev. B* **93**, 035138 (2016). 4

[75] D. Muñoz Segovia, A. Cortijo, "Many-body effects in nodal-line semimetals: Correction to the optical conductivity", *Phys. Rev. B* **101**, 205102 (2020). 4

[76] A. R. Medeiros-Silva, N. C. Costa, T. Paiva, "Thermodynamic, magnetic, and transport properties of the repulsive Hubbard model on the kagome lattice", *Phys. Rev. B* **107**, 035134 (2023). 5, 26, 40, 58

[77] W. C. de Freitas Silva, A. R. Medeiros-Silva, R. Mondaini, V. V. França, T. Paiva, Single-site entanglement as a marker for quantum phase transitions at non-zero temperatures (2025). 5, 43

[78] A. R. Medeiros-Silva, M. Malard, R. G. Pereira, T. Paiva, "Electronic interactions in a vacancy-engineered honeycomb lattice: Transition from a nodal-line semimetal to a magnetic insulator", *Phys. Rev. B* **111**, 195152 (2025). 5, 58, 68

[79] J. Hubbard, "Electron Correlations in Narrow Energy Bands", *Proc. R. Soc. London, Ser. A* **276**, 238 (1963). 6

[80] J. E. Hirsch, "Discrete Hubbard-Stratonovich transformation for fermion lattice models", *Phys. Rev. B* **28**, 4059 (1983). 6, 9

[81] S. R. White, D. J. Scalapino, R. L. Sugar, N. E. Bickers, R. T. Scalettar, "Attractive and repulsive pairing interaction vertices for the two-dimensional Hubbard model", *Phys. Rev. B* **39**, 839 (1989). 6, 47

[82] F. Assaad, *Quantum Simulations of Complex Many-Body Systems: From Theory to Algorithms*, J. Grotendorst, D. Marx, A. Muramatsu, eds. (NIC Series, 2002), vol. 10, pp. 99–156. 6

[83] R. R. dos Santos, "Introduction to quantum Monte Carlo simulations for fermionic systems", *Brazilian Journal of Physics* **33**, 36 (2003). 6

[84] J. Gubernatis, N. Kawashima, P. Werner, *Quantum Monte Carlo Methods: Algorithms for Lattice Models* (Cambridge University Press, Cambridge, England, 2016). 6

[85] F. Becca, S. Sorella, *Quantum Monte Carlo approaches for correlated systems* (Cambridge University Press, Cambridge, England, 2017). 6

[86] L. Rademaker, S. Johnston, J. Zaanen, J. van den Brink, "Determinant quantum Monte Carlo study of exciton condensation in the bilayer Hubbard model", *Phys. Rev. B* **88**, 235115 (2013). 9

[87] S. Wessel, B. Normand, F. Mila, A. Honecker, "Efficient Quantum Monte Carlo simulations of highly frustrated magnets: the frustrated spin-1/2 ladder", *SciPost Phys.* **3**, 005 (2017). 10

[88] R. Mondaini, S. Tarat, R. T. Scalettar, "Quantum critical points and the sign problem", *Science* **375**, 418 (2022). 10, 40

[89] R. Mondaini, S. Tarat, R. T. Scalettar, "Universality and critical exponents of the fermion sign problem", *Phys. Rev. B* **107**, 245144 (2023). 10, 36, 39, 40, 43

[90] S. Yan, D. A. Huse, S. R. White, "Spin-Liquid Ground State of the ¡i¿S¡/i¿ = 1/2 Kagome Heisenberg Antiferromagnet", *Science* **332**, 1173 (2011). 12

[91] Y. Iqbal, F. Becca, S. Sorella, D. Poilblanc, "Gapless spin-liquid phase in the kagome spin-$\frac{1}{2}$ Heisenberg antiferromagnet", *Phys. Rev. B* **87**, 060405 (2013). 12

[92] A. Yamada, K. Seki, R. Eder, Y. Ohta, "Mott transition and ferrimagnetism in the Hubbard model on the anisotropic kagome lattice", *Phys. Rev. B* **83**, 195127 (2011). 12

[93] R. Higa, K. Asano, "Bond formation effects on the metal-insulator transition in the half-filled kagome Hubbard model", *Phys. Rev. B* **93**, 245123 (2016). 12

[94] T. Ohashi, N. Kawakami, H. Tsunetsugu, "Mott Transition in Kagomé Lattice Hubbard Model", *Phys. Rev. Lett.* **97**, 066401 (2006). 12

[95] S. Kuratani, A. Koga, N. Kawakami, "Mott transition of correlated electrons on the Kagomé lattice", *Journal of Physics: Condensed Matter* **19**, 145252 (2007). 12

[96] N. Bulut, W. Koshibae, S. Maekawa, "Magnetic Correlations in the Hubbard Model on Triangular and Kagomé Lattices", *Phys. Rev. Lett.* **95**, 037001 (2005). 13

[97] J. Kaufmann, K. Steiner, R. T. Scalettar, K. Held, O. Janson, "How correlations change the magnetic structure factor of the kagome Hubbard model", *Phys. Rev. B* **104**, 165127 (2021). 13

[98] R.-Y. Sun, Z. Zhu, "Metal-insulator transition and intermediate phases in the kagome lattice Hubbard model", *Phys. Rev. B* **104**, L121118 (2021). 13, 35

[99] C. Wen, *et al.*, "Superconducting pairing symmetry in the kagome-lattice Hubbard model", *Phys. Rev. B* **105**, 075118 (2022). 13

[100] A. J. Kim, F. Simkovic, E. Kozik, "Spin and Charge Correlations across the Metal-to-Insulator Crossover in the Half-Filled 2D Hubbard Model", *Phys. Rev. Lett.* **124**, 117602 (2020). 13

[101] A.-M. Daré, L. Raymond, G. Albinet, A. M. S. Tremblay, "Interaction-induced adiabatic cooling for antiferromagnetism in optical lattices", *Phys. Rev. B* **76**, 064402 (2007). 15

[102] T. Paiva, R. T. Scalettar, C. Huscroft, A. K. McMahan, "Signatures of spin and charge energy scales in the local moment and specific heat of the half-filled two-dimensional Hubbard model", *Phys. Rev. B* **63**, 125116 (2001). 16, 17

[103] E. Khatami, M. Rigol, "Thermodynamics of strongly interacting fermions in two-dimensional optical lattices", *Phys. Rev. A* **84**, 053611 (2011). 16

[104] B. Tang, T. Paiva, E. Khatami, M. Rigol, "Short-Range Correlations and Cooling of Ultracold Fermions in the Honeycomb Lattice", *Phys. Rev. Lett.* **109**, 205301 (2012). 16

[105] B. Tang, T. Paiva, E. Khatami, M. Rigol, "Finite-temperature properties of strongly correlated fermions in the honeycomb lattice", *Phys. Rev. B* **88**, 125127 (2013). 16

[106] T. Paiva, R. T. Scalettar, W. Zheng, R. R. P. Singh, J. Oitmaa, "Ground-state and finite-temperature signatures of quantum phase transitions in the half-filled Hubbard model on a honeycomb lattice", *Phys. Rev. B* **72**, 085123 (2005). 16, 35, 40, 46, 55, 62

[107] T. Paiva, R. Scalettar, M. Randeria, N. Trivedi, "Fermions in 2D Optical Lattices: Temperature and Entropy Scales for Observing Antiferromagnetism and Superfluidity", *Phys. Rev. Lett.* **104**, 066406 (2010). 16, 58

[108] M. Udagawa, Y. Motome, "Chirality-Driven Mass Enhancement in the Kagome Hubbard Model", *Phys. Rev. Lett.* **104**, 106409 (2010). 18

[109] N. Trivedi, M. Randeria, "Deviations from Fermi-Liquid Behavior above T_c in 2D Short Coherence Length Superconductors", *Phys. Rev. Lett.* **75**, 312 (1995). 23

[110] N. Trivedi, R. T. Scalettar, M. Randeria, "Superconductor-insulator transition in a disordered electronic system", *Phys. Rev. B* **54**, R3756 (1996). 24

[111] P. J. H. Denteneer, R. T. Scalettar, N. Trivedi, "Conducting Phase in the Two-Dimensional Disordered Hubbard Model", *Phys. Rev. Lett.* **83**, 4610 (1999). 24

[112] R. Mondaini, K. Bouadim, T. Paiva, R. R. dos Santos, "Finite-size effects in transport data from quantum Monte Carlo simulations", *Phys. Rev. B* **85**, 125127 (2012). 24

[113] V. Vedral, "Entanglement hits the big time", *Nature* **425**, 28 (2003). 31

[114] I. Klich, G. Refael, A. Silva, "Measuring entanglement entropies in many-body systems", *Phys. Rev. A* **74**, 032306 (2006). 31

[115] A. Acín, *et al.*, "The quantum technologies roadmap: a European community view", *New Journal of Physics* **20**, 080201 (2018). 31

[116] L. Wei, "Skewness of von Neumann entanglement entropy", *Journal of Physics A: Mathematical and Theoretical* **53**, 075302 (2020). 31

[117] L. Amico, R. Fazio, A. Osterloh, V. Vedral, "Entanglement in many-body systems", *Rev. Mod. Phys.* **80**, 517 (2008). 31

[118] R. Islam, *et al.*, "Measuring entanglement entropy in a quantum many-body system", *Nature* **528**, 054422 (2015). 31

[119] N. Aslam, *et al.*, "Quantum sensors for biomedical applications", *Nature Reviews Physics* **5**, 157 (2023). 31

[120] C. Hempel, *et al.*, "Quantum Chemistry Calculations on a Trapped-Ion Quantum Simulator", *Phys. Rev. X* **8**, 031022 (2018). 31

[121] A. M. Souza, M. S. Reis, D. O. Soares-Pinto, I. S. Oliveira, R. S. Sarthour, "Experimental determination of thermal entanglement in spin clusters using magnetic susceptibility measurements", *Phys. Rev. B* **77**, 104402 (2008). 31

[122] D. Das, H. Singh, T. Chakraborty, R. K. Gopal, C. Mitra, "Experimental detection of quantum information sharing and its quantification in quantum spin systems", *New Journal of Physics* **15**, 013047 (2013). 31

[123] D. Larsson, H. Johannesson, "Entanglement Scaling in the One-Dimensional Hubbard Model at Criticality", *Phys. Rev. Lett.* **95**, 196406 (2005). 31, 33, 34

[124] T. Pauletti, M. Silva, G. Canella, V. França, "Linear entropy fails to predict entanglement behavior in low-density fermionic systems", *Physica A: Statistical Mechanics and its Applications* **644**, 129824 (2024). 33, 34

[125] J. von Neumann, *Mathematical Foundations of Quantum Mechanics*, Goldstine Printed Materials (Princeton University Press, 1955). 33

[126] A. Rényi, *Proceedings of the Fourth Berkeley Symposium on Mathematics, Statistics and Probability, 1960* (University of California Press, 1961), pp. 547–561. 33

[127] J. C. Principe, *Information Theoretic Learning: Renyi's Entropy and Kernel Perspectives*, no. XIV, 448 (Springer New York, NY, 2010), first edn. 33

[128] L.-A. Wu, M. S. Sarandy, D. A. Lidar, "Quantum Phase Transitions and Bipartite Entanglement", *Phys. Rev. Lett.* **93**, 250404 (2004). 33

[129] V. V. França, K. Capelle, "Universal and nonuniversal contributions to block-block entanglement in many-fermion systems", *Phys. Rev. A* **77**, 062324 (2008). 33

[130] K. Capelle, V. L. Campo, "Density functionals and model Hamiltonians: Pillars of many-particle physics", *Physics Reports* **528**, 91 (2013). Density functionals and model Hamiltonians: Pillars of many-particle physics. 33

[131] T. de Picoli, I. D'Amico, V. V. França, "Metric-Space Approach for Distinguishing Quantum Phase Transitions in Spin-Imbalanced Systems", *Brazilian Journal of Physics* **48**, 472 (2018). 33

[132] D. L. B. Ferreira, T. O. Maciel, R. O. Vianna, F. Iemini, "Quantum correlations, entanglement spectrum, and coherence of the two-particle reduced density matrix in the extended Hubbard model", *Phys. Rev. B* **105**, 115145 (2022). 33

[133] R. Blatt, C. F. Roos, "Quantum simulations with trapped ions", *Nature Physics* **8**, 277 (2012). 33

[134] I. Bloch, J. Dalibard, S. Nascimbène, "Quantum simulations with ultracold quantum gases", *Nature Physics* **8**, 267 (2012). 33

[135] V. V. França, K. Capelle, "Entanglement of strongly interacting low-dimensional fermions in metallic, superfluid, and antiferromagnetic insulating systems", *Phys. Rev. A* **74**, 042325 (2006). 34, 36

[136] V. V. F. HENN, Emaranhamento em Sistemas de Muitos Férmions, Doutorado em física básica, Instituto de Física de São Carlos, Universidade de São Paulo, São Carlos (2008). 34

[137] Y. Otsuka, S. Yunoki, S. Sorella, "Universal Quantum Criticality in the Metal-Insulator Transition of Two-Dimensional Interacting Dirac Electrons", *Phys. Rev. X* **6**, 011029 (2016). 35, 40

[138] H. Q. Lin, J. E. Hirsch, "Two-dimensional Hubbard model with nearest- and next-nearest-neighbor hopping", *Phys. Rev. B* **35**, 3359 (1987). 35

[139] A. Garg, H. R. Krishnamurthy, M. Randeria, "Can Correlations Drive a Band Insulator Metallic?", *Phys. Rev. Lett.* **97**, 046403 (2006). 36

[140] K. Bouadim, N. Paris, F. Hébert, G. G. Batrouni, R. T. Scalettar, "Metallic phase in the two-dimensional ionic Hubbard model", *Phys. Rev. B* **76**, 085112 (2007). 36

[141] N. Paris, K. Bouadim, F. Hebert, G. G. Batrouni, R. T. Scalettar, "Quantum Monte Carlo Study of an Interaction-Driven Band-Insulator–to–Metal Transition", *Phys. Rev. Lett.* **98**, 046403 (2007). 36

[142] K. Byczuk, M. Sekania, W. Hofstetter, A. P. Kampf, "Insulating behavior with spin and charge order in the ionic Hubbard model", *Phys. Rev. B* **79**, 121103 (2009). 36

[143] L. Craco, P. Lombardo, R. Hayn, G. I. Japaridze, E. Müller-Hartmann, "Electronic phase transitions in the half-filled ionic Hubbard model", *Phys. Rev. B* **78**, 075121 (2008). 36, 39, 40, 43

[144] S. S. Kancharla, E. Dagotto, "Correlated Insulated Phase Suggests Bond Order between Band and Mott Insulators in Two Dimensions", *Phys. Rev. Lett.* **98**, 016402 (2007). 36

[145] A. Moreo, "Magnetic susceptibility of the two-dimensional Hubbard model", *Phys. Rev. B* **48**, 3380 (1993). 41

[146] F. Liu, *et al.*, "Robust Topological Nodal-Line Semimetals from Periodic Vacancies in Two-Dimensional Materials", *The Journal of Physical Chemistry Letters* **12**, 5710 (2021). PMID: 34128659. 44, 49

[147] M. S. M. de Sousa, F. Liu, M. Malard, F. Qu, W. Chen, "Symmetry-enforced nodal lines in the band structures of vacancy-engineered graphene", *Phys. Rev. B* **105**, 155414 (2022). 44, 49

[148] V. N. Kotov, B. Uchoa, V. M. Pereira, F. Guinea, A. H. Castro Neto, "Electron-Electron Interactions in Graphene: Current Status and Perspectives", *Rev. Mod. Phys.* **84**, 1067 (2012). 45

[149] M. R. Slot, *et al.*, "Experimental realization and characterization of an electronic Lieb lattice", *Nat. Phys.* **13**, 672 (2017). 45

[150] A. A. Burkov, M. D. Hook, L. Balents, "Topological nodal semimetals", *Phys. Rev. B* **84**, 235126 (2011). 45

[151] S. Sorella, Y. Otsuka, S. Yunoki, "Absence of a Spin Liquid Phase in the Hubbard Model on the Honeycomb Lattice", *Sci Rep* **2** (2012). 46, 55, 62

[152] A. Ramachandran, A. Andreanov, S. Flach, "Chiral flat bands: Existence, engineering, and stability", *Phys. Rev. B* **96**, 161104 (2017). 49

[153] E. H. Lieb, "Two theorems on the Hubbard model", *Phys. Rev. Lett.* **62**, 1201 (1989). 49, 61

[154] Y. L. Loh, N. Trivedi, "Theoretical Studies of Superconductor-Insulator Transitions", *Conductor-Insulator Quantum Phase Transitions* (2013). 49

[155] K. Beach, "Magnetic-field-induced antiferromagnetism in the Kondo lattice", *Ph.D. thesis, Dept. of Physics, Massachusetts Institute of Technology* (1999). 49

[156] G. Chen, L. Balents, "Spin-orbit effects in $Na_4Ir_3O_8$: A hyper-kagome lattice antiferromagnet", *Phys. Rev. B* **78**, 094403 (2008). 56

[157] J. D. Reger, J. A. Riera, A. P. Young, "Monte Carlo simulations of the spin-1/2 Heisenberg antiferromagnet in two dimensions", *J. Phys.: Condens. Matter* **1**, 1855 (1989). 58

[158] A. J. Kim, F. Simkovic, E. Kozik, "Spin and Charge Correlations across the Metal-to-Insulator Crossover in the Half-Filled 2D Hubbard Model", *Phys. Rev. Lett.* **124**, 117602 (2020). 58

[159] W. C. F. Silva, *et al.*, "Effects of strong electronic interactions on the thermopower properties of the repulsive Hubbard model", *Phys. Rev. B* **108**, 075101 (2023). 58

[160] N. T. Sayantan Roy, Abhisek Samanta, "Sign changes of the thermoelectric transport coefficient across the metal-insulator crossover in the doped Fermi Hubbard model", *arXiv:2407.01680* (2024). 58

[161] F. Werner, O. Parcollet, A. Georges, S. R. Hassan, "Interaction-Induced Adiabatic Cooling and Antiferromagnetism of Cold Fermions in Optical Lattices", *Phys. Rev. Lett.* **95**, 056401 (2005). 58

[162] A.-M. Daré, L. Raymond, G. Albinet, A. M. S. Tremblay, "Interaction-induced adiabatic cooling for antiferromagnetism in optical lattices", *Phys. Rev. B* **76**, 064402 (2007). 58

[163] T. Paiva, Y. L. Loh, M. Randeria, R. T. Scalettar, N. Trivedi, "Fermions in 3D Optical Lattices: Cooling Protocol to Obtain Antiferromagnetism", *Phys. Rev. Lett.* **107**, 086401 (2011). 58

[164] T. Paiva, *et al.*, "Cooling Atomic Gases With Disorder", *Phys. Rev. Lett.* **115**, 240402 (2015). 58

[165] M. Charlebois, D. Sénéchal, A.-M. Gagnon, A.-M. S. Tremblay, "Impurity-induced magnetic moments on the graphene-lattice Hubbard model: An inhomogeneous cluster dynamical mean-field theory study", *Phys. Rev. B* **91**, 035132 (2015). 61

[166] N. C. Costa, T. Mendes-Santos, T. Paiva, R. R. d. Santos, R. T. Scalettar, "Ferromagnetism beyond Lieb's theorem", *Phys. Rev. B* **94**, 155107 (2016). 61

[167] D. Nicoletti, *et al.*, "Magnetic-Field Tuning of Light-Induced Superconductivity in Striped $La_{2-x}Ba_xCuO_4$", *Phys. Rev. Lett.* **121**, 267003 (2018). 69

[168] C. R. Hunt, *et al.*, "Dynamical decoherence of the light induced interlayer coupling in $YBa_2Cu_3O_{6+\delta}$", *Phys. Rev. B* **94**, 224303 (2016). 69, 73

[169] A. Ribak, *et al.*, "Two-fluid dynamics in driven $YBa_2Cu_3O_{6.48}$", *Phys. Rev. B* **107**, 104508 (2023). 69

[170] C. Shao, P. D. Sacramento, R. Mondaini, "Photoinduced anomalous Hall effect in the interacting Haldane model: Targeting topological states with pump pulses", *Phys. Rev. B* **104**, 125129 (2021). 69

[171] Y. Zhang, R. Mondaini, R. T. Scalettar, "Photoinduced enhancement of superconductivity in the plaquette Hubbard model", *Phys. Rev. B* **107**, 064309 (2023). 69

[172] F. Chen, F. D. M. Haldane, D. N. Sheng, "Global phase diagram of D-wave superconductivity in the square-lattice t-J model", *Proceedings of the National Academy of Sciences* **122**, e2420963122 (2025). 70

[173] S. R. Manmana, A. Muramatsu, R. M. Noack, "Time evolution of one-dimensional Quantum Many Body Systems", *AIP Conference Proceedings* **789**, 269 (2005). 71

[174] P. Prelovšek, J. Bonča, *Ground State and Finite Temperature Lanczos Methods* (Springer Berlin Heidelberg, Berlin, Heidelberg, 2013), pp. 1–30. 71

[175] A. Iwano, Y. Yamaji, "Superconductivity in Bilayer t–t' Hubbard Models", *Journal of the Physical Society of Japan* **91**, 094702 (2022). 73

[176] S. Rajasekaran, *et al.*, "Probing optically silent superfluid stripes in cuprates", *Science* **359**, 575 (2018). 73

[177] B. Liu, *et al.*, "Pump Frequency Resonances for Light-Induced Incipient Superconductivity in $YBa_2Cu_3O_{6.5}$", *Phys. Rev. X* **10**, 011053 (2020). 73